IOP Publishing Journal of Physics: Condensed Matter
J. Phys.: Condens. Matter **34** (2022) 443001 (41pp) https://doi.org/10.1088/1361-648X/ac8a7f

## Topical Review

# Carbon-based nanostructures as a versatile platform for tunable $\pi$-magnetism

**Dimas G de Oteyza**[1,2,*] **and Thomas Frederiksen**[2,3,*]

[1] Nanomaterials and Nanotechnology Research Center (CINN), CSIC-UNIOVI-PA, E-33940 El Entrego, Spain
[2] Donostia International Physics Center (DIPC)—UPV/EHU, E-20018 San Sebastián, Spain
[3] Ikerbasque, Basque Foundation for Science, E-48013 Bilbao, Spain

E-mail: d.g.oteyza@cinn.es and thomas_frederiksen@ehu.eus

Received 8 April 2022, revised 27 June 2022
Accepted for publication 17 August 2022
Published 5 September 2022

**Abstract**

Emergence of $\pi$-magnetism in open-shell nanographenes has been theoretically predicted decades ago but their experimental characterization was elusive due to the strong chemical reactivity that makes their synthesis and stabilization difficult. In recent years, on-surface synthesis under vacuum conditions has provided unprecedented opportunities for atomically precise engineering of nanographenes, which in combination with scanning probe techniques have led to a substantial progress in our capabilities to realize localized electron spin states and to control electron spin interactions at the atomic scale. Here we review the essential concepts and the remarkable advances in the last few years, and outline the versatility of carbon-based $\pi$-magnetic materials as an interesting platform for applications in spintronics and quantum technologies.

Keywords: open-shell nanographenes, $\pi$-magnetism, electron spin, magnetic interactions

(Some figures may appear in colour only in the online journal)

## 1. Introduction

Magnetic materials are key to a wide variety of technological applications. However, to date their practical use is limited to transition metals with unpaired *d*- or *f*-shell electrons. The same applies even for the so-called molecular magnetism that has been studied and developed for decades, but still relying on coordination of *d*- or *f*-block elements to organic ligands [1, 2]. Instead, the magnetism associated to *p*-shell electrons in carbon-based materials has been hardly utilized to date and only recently it is being enthusiastically explored [3, 4]. There are multiple reasons for the booming interest that it is raising. On the one hand we find the attractive magnetic properties offered by light materials like carbon nanostructures, which display weak spin-orbit and hyperfine couplings, the two main channels responsible for the relaxation and decoherence of electron spins [3, 5–7]. In addition, they are also expected to display high spin-wave stiffness, which should be mirrored in high Curie temperatures and long spin correlation lengths [3, 8]. These materials thus make for a greatly promising platform on which to exploit spin-polarized currents or the processing of spin-based quantum information [3, 7, 9–11]. On the other hand, carbon-based materials also display several advantages with regard to their processing, with the potential to allow for a cheap and scalable production of materials that,

* Authors to whom any correspondence should be addressed.

 

beyond their magnetic functionalities, may further include biocompatibility, light weight or plasticity. Lastly, molecule-based materials profit from the prospects of bottom-up production methods, which may be among the keys for success if the current miniaturization trend in information technology devices is to be maintained.

Until recently, the main drawback faced by carbon-based $\pi$-magnetism was its poor reproducibility. The magnetic properties or carbon-based nanostructures are extremely susceptible to minute changes in the bonding configuration and at the same time they are based on unpaired $\pi$-electrons that display great propensity for chemical reactions [12, 13]. Indeed, besides information or quantum technology applications, diradicals are also of key importance for the understanding and further development of organic chemistry due to their characteristic reactivity and their inevitable presence, even if often only transiently due to their limited lifetime [13]. This is one of the reasons for which diradicals have been extensively studied in the past [13, 14], but also for the scarce reproducible studies about magnetic carbon-based materials, whose chemical reactivity either hindered their synthesis by conventional wet chemistry, forcing the addition of protecting groups, or hampered their characterization due to an excessively short product's lifetime. However, the advent of surface-supported chemistry under vacuum, typically termed as on-surface synthesis (OSS) [15–18], has provided unprecedented opportunities for the synthesis and characterization of this type of materials [4, 19]. The inert vacuum environment, in combination with the often stabilizing effect of the supporting substrate, allows for the synthesis of carbon-based nanostructures and at the same time limits its possible degradation mechanisms. Furthermore, it places at the researcher's disposal a variety of surface sensitive characterization techniques with which to characterize the samples, including scanning probe microscopies (SPMs) and spectroscopies (STS) [15–17]. The latter allow for a precise determination of the covalent bonding structure as well as for a simultaneous assessment of the electronic and magnetic properties at the single molecule level.

These new prospects have caused the research on magnetic carbon-based nanostructures to be booming over the last years [4, 19]. In turn, the increasing number of researchers that are focusing their efforts into this field have facilitated an impressive progress in short time. Although the experimental proof of the magnetism associated to carbon vacancies in graphene (as observed by SPM at the single vacancy level) already dates back to 2007 [20], the synthesis of iconic molecules with intrinsic magnetic properties that were theoretically devised already in the 1950s, like triangulene [21], has only occurred in recent years [22]. Along with triangulene, many other highly coveted carbon-based nanostructures with magnetic properties have been synthesized and studied over the last few years, like for example Clar's goblet [23, 24] and zigzag-edged graphene nanoribbons (GNRs) [25]. The growing number of available systems for experimental study has also brought about an increasing understanding of the properties and of the magnetic interactions between different magnetic (radical) $\pi$-states. This increased understanding, along with the continuously improving capabilities of OSS strategies, have further allowed for the generation of one- and two-dimensional materials with engineered properties as provided by the controlled coupling of appropriately placed radical $\pi$-states in periodic arrays [26, 27]. That is, the development of the synthetic protocols and the understanding of the resulting material's properties are going hand in hand and are responsible for the fascinating advances reached in carbon-based magnetism.

At this point it needs to be remarked that there is a stringent requirement on atomic precision for the synthesis of the carbon nanostructures. Minor changes in the bonding structure may result in dramatic changes to the optoelectronic and magnetic properties, as exemplified in figure 1 with seven different molecular structures. Although they all feature a comparable number of carbon atoms and associated rings, the energy of their calculated frontier orbitals, which is displayed in the bottom part, varies enormously, with decreasing HOMO–LUMO gaps and the appearance of zero-energy states when moving from left to right. As explained later on, low HOMO–LUMO gaps (and thus even more zero-energy states) may not warrant but at least facilitate the appearance of magnetic properties in carbon nanostructures (indeed when going from left to right there is a gradual change from a purely closed-shell character, through gradually increasing open-shell character and all the way to a high-spin molecule). From the calculated orbital energies in figure 1(c) we can therefore already extract some qualitative trends for parameters that, although again being no guarantee for magnetism, generally promote its appearance. One is increasing molecular size, as can be inferred from comparison of the isomorphic structures (**1** *vs.* **2**, **3** *vs.* **4** and **5** *vs.* **6**), which show a smaller gap for the larger structures. Another one is the presence of zigzag edges, as can be inferred from comparing **1** and **2** with **3** and **4**, or also with structure **7**, which displays zigzag edges all over its perimeter and has two zero-energy states. Lastly, also the presence of non-benzenoid rings facilitates the appearance of magnetism, as may be inferred from comparing **1** and **2** with **5** and **6**, the latter of which even displays a zero-energy state. Also a comparison of **3** with **5** reveals a comparable HOMO–LUMO gap in spite of the lower number of carbon atoms in the latter. The reasons underlying the effects of each of these parameters on the material's magnetic properties will be discussed and explained in more detail in the following sections.

This review is organized as follows. We begin with an overview in section 2 of commonly used computational approaches to describe the electronic structure of graphene nanostructures and relationships between band topology, emergence of spin-polarization and many-body spin states. In section 3 we present well-established counting rules to infer the relationship between nanographene geometry and its ground-state spin properties. After a review in section 4 of the experimental techniques for nanographene synthesis and scanning probe characterization, we proceed to discuss the different mechanisms to induce magnetism. Section 6 is devoted to interactions among spin states and section 7 to the chemical reactivity associated with the open-shell character of the involved spin states. Finally, an outlook is presented in section 8.

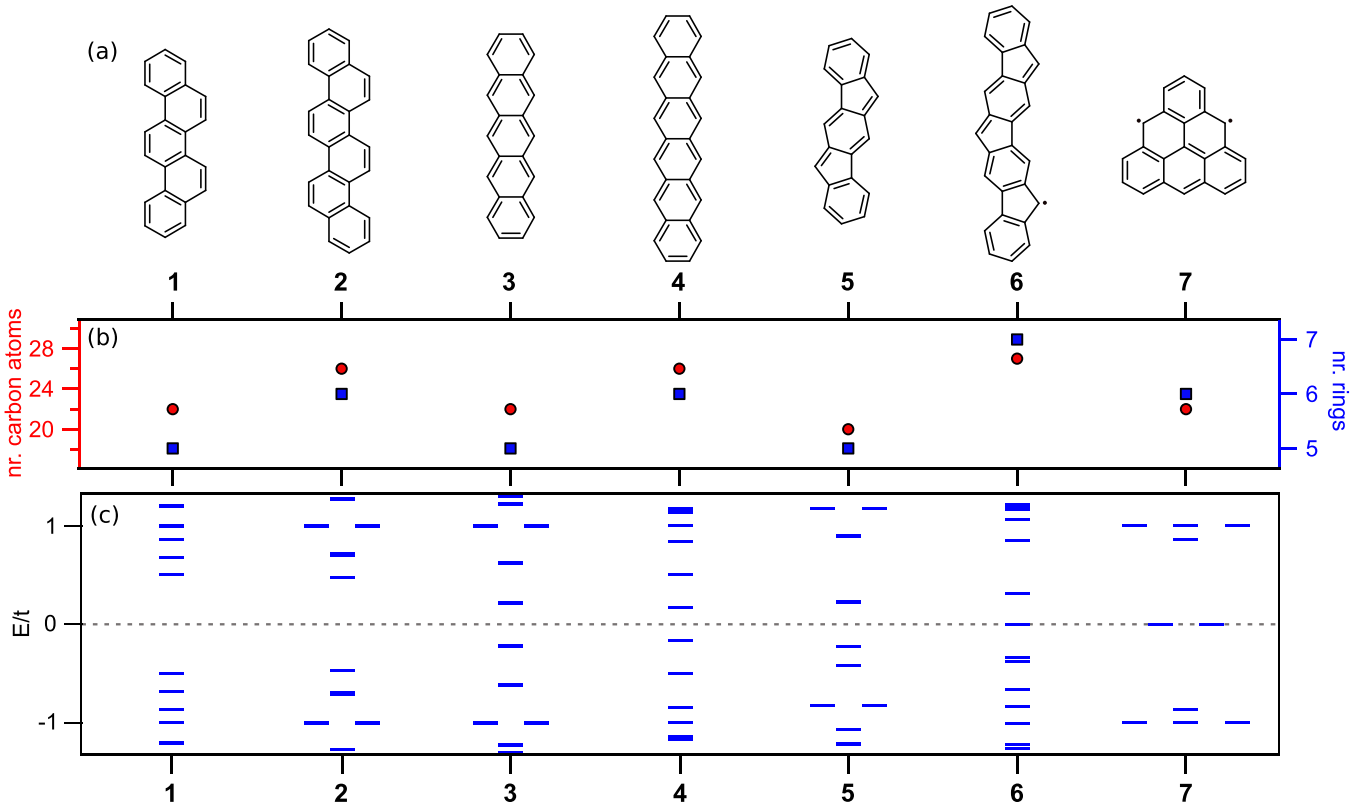


**Figure 1.** (a) Molecular structures for comparison. (b) Number of carbon atoms and comprised rings. (c) Calculated low-energy spectrum within a tight-binding (TB) model with nearest neighbor hopping $t$.

## 2. Computational approaches

Carbon has four valence electrons in the second shell which favors the formation of four single bonds. In the case of planar carbon structures like graphene, the robust trigonal structure arises from a $sp^2$ hybridization of one $2s$ and two $2p$ carbon orbitals to form doubly-occupied $\sigma$ bonds with its three neighbors. The remaining electron, associated with the out-of-plane orbital $2p_z$, forms $\pi$-bonding with its neighbors, resulting in a half-filled $\pi$ band at the origin of interesting electronic properties of graphene, such as 'relativistic' massless Dirac fermions and valley degeneracy [28, 29], emergence of $\pi$-magnetism at edges and defects [3], and exceptional transport phenomena [30]. The electronic structure of $sp^2$ carbon systems can be addressed computationally at different levels as outlined in the following sections.

### 2.1. Density functional theory

In condensed matter physics, density functional theory (DFT) is probably the most popular approach to describe the electronic structure of materials [31]. It is theoretically founded in the Hohenberg–Kohn theorems, establishing that the electron *density* that minimizes the total energy corresponds to that of the ground state of the system. In principle, this implies a drastic reduction of complexity since the ground state of a many-body problem can be described by the electron density instead of the full wave function. The Kohn–Sham (KS) equations (KS-DFT) make this theory tractable in practice by introducing an effective non-interacting Schrödinger equation for one-electron KS orbitals that lead to the same electron density as for the interacting system. The KS wave function of the $N$-electron system is then written as a Slater determinant of these single-particle orbitals. The only unknown is the so-called exchange-correlation (XC) functional, which leads to typical schemes such as the local-density approximation (LDA), the generalized-gradient approximation (GGA), etc. Having fixed the XC functional, the problem is then solved iteratively for the self-consistent solution to the KS equations.

The reason for the popularity of DFT nowadays is the tractability of systems of thousands of atoms, without any system-specific parameters, with high accuracy for ground state properties such as lattice constants and phonons for solids as well as geometry and vibrations for molecules. A recent Special Topic Issue [32] on electronic structure software provides a broad overview of many quantum chemistry codes based on DFT and beyond.

DFT is also successful in describing many aspects of carbon $\pi$-magnetism as is evident from the vast body of literature covered in this review. It allows, for instance, to compute the spin density for adsorbed atoms, molecules and extended 2D structures on metal surfaces and interfaces. Spin in KS-DFT [33] is typically described in the symmetry-broken form, where the spin density of the non-interacting electrons are targeting an accurate description of the energetics of low-spin states at the expense of matching the exact spin state of the

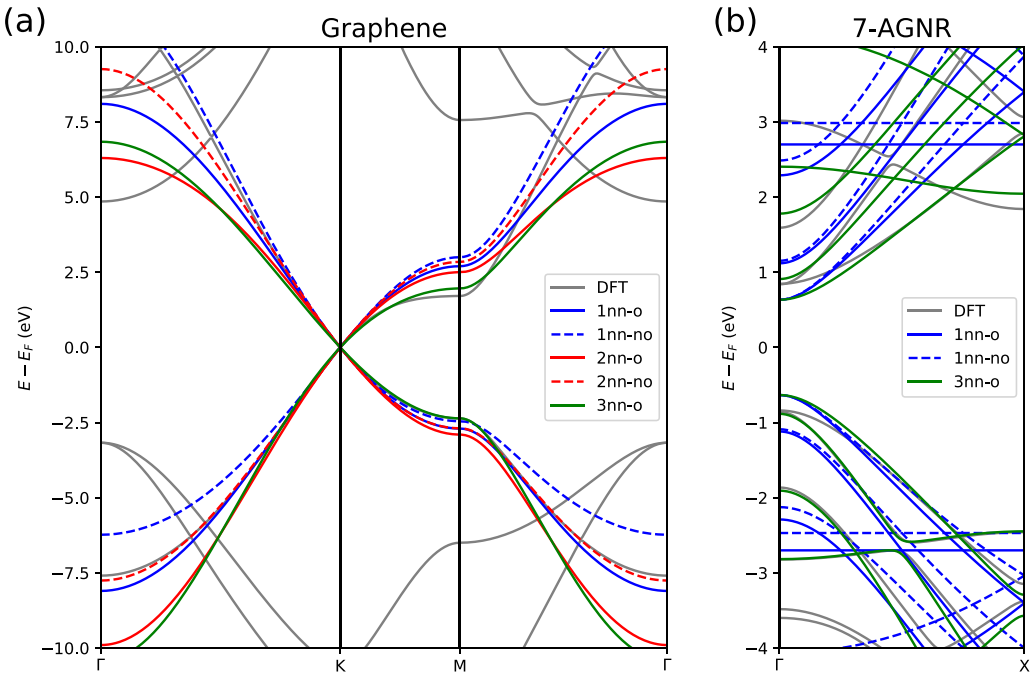


**Figure 2.** Comparison of electronic band structures from different TB models and DFT for (a) graphene and (b) a hydrogen-terminated 7-AGNR. The nearest neighbor (1nn, blue) model includes $t_1 = -2.7$ eV, the next-nearest neighbor (2nn, red) model also $t_2 = -0.2$ eV, and the third-nearest neighbor (3nn, green) model additionally $t_3 = -0.18$ eV. Both orthogonal (-o, full lines) and nonorthogonal (-no, dashed lines) basis variants are considered, the latter with a nearest-neighbor overlap set to $s_1 = 0.1$. The gray bands correspond to SIESTA [35] DFT-GGA calculations using a TZTP (DZP) basis set and lattice constant $a = 2.460$ (4.260) Å for graphene (7AGNR).

interacting problem. This occurs because the KS orbitals for the two spin components are allowed to differ in the spin-unrestricted formulation. This leads to wave functions that are not true eigenstates of the total spin operator $\hat{S}^2$ (only of the $\hat{S}_z$ projection), i.e. they are in principle spin-contaminated. This limitation, which applies more generally to all mean-field descriptions, is important to keep in mind for applications to open-shell molecules. Wave-function based methods from computational chemistry (configuration-interaction, coupled cluster, etc) are therefore more suitable for accurately describing spin states, but these are limited to small systems.

### 2.2. Tight binding

Due to the orthogonality of the $\sigma$ and $\pi$ electrons in planar structures, it is possible to study them separately. The advantages of such effective descriptions involving only the latter are simplicity and numerical efficiency, which may also help to reach a better understanding of the mechanisms at play.

In the tight-binding (TB) approximation one describes electrons in a solid in terms of the atomic orbitals of isolated atoms and the corrections that arise due to their overlaps [34]. The electrons are also treated as independent (noninteracting) particles. The (multi-band) TB Hamiltonian can be written as:

$$\hat{H}^0 = \sum_{ij\sigma} H^0_{ij} \hat{c}^\dagger_{i\sigma} \hat{c}_{j\sigma}, \tag{1}$$

where $\hat{c}^\dagger_{i\sigma}$ is the fermionic creation operator of an electron with spin $\sigma = \{\uparrow, \downarrow\}$ in basis orbital $i$. The operators satisfy the usual anticommutation relations $\{\hat{c}_\mu, \hat{c}_\nu\} = \{\hat{c}^\dagger_\mu, \hat{c}^\dagger_\nu\} = 0$ and $\{\hat{c}_\mu, \hat{c}^\dagger_\nu\} = \delta_{\mu\nu}$. The matrix elements $H^0_{ij} = \langle i|\hat{H}^0|j\rangle$ describe the onsite energies along the diagonal and the strength of electron hopping between orbitals $i$ and $j$ in the off-diagonals. The matrix elements are real and satisfy $H^0_{ij} = H^0_{ji}$. In general, the basis orbitals may be nonorthogonal represented by the overlap integrals $S_{ij} = \langle i|j\rangle$. For simplicity, one may assume orthogonality and write $S_{ij} = \delta_{ij}$. For $sp^2$ carbon the simplest description includes just the $2p_z$ orbital at each carbon atom with nearest-neighbor hopping matrix elements $t = -2.7$ eV [28].

The time-independent Schrödinger equation for the TB Hamiltonian can be written as as a generalized eigenvalue problem:

$$\mathbf{H}^0 \boldsymbol{\psi}_\alpha = \varepsilon_\alpha \mathbf{S} \boldsymbol{\psi}_\alpha, \tag{2}$$

where $\varepsilon_\alpha$ is the eigenenergy corresponding to state $\boldsymbol{\psi}_\alpha = \sum_i |i\rangle\langle i|\alpha\rangle$.

Different TB approximations for the $\pi$-bands of graphene are shown in figure 2(a), constructed with the free SISL software [36] using typical parameters from the literature [28, 37]. In the simplest description with only nearest neighbor interactions $t_1$ and orthogonal basis states the bands are perfectly symmetric with respect to the Fermi level (full line blue bands, `1nn-o`). When a finite overlap is introduced (blue dashed bands, `1nn-no`) an asymmetry between empty and filled states

develops. Introduction of second-nearest neighbor interactions $t_2$ breaks the sublattice symmetry (red bands, `2nn`) and lowers the bands at Γ. Further, inclusion of third-nearest neighbor interactions $t_3$ (green bands, `3nn-o`), which represent atomic distances only marginally larger than the next-nearest pairs, enables a lowering of the empty band around $M$. For comparison, we also show the corresponding bands from DFT calculations (gray bands) [35].

Figure 2(b) concerns a similar comparison between TB and DFT calculations for a different system, namely the $\pi$-band states of a 7-atom wide armchair graphene nanoribbon (7-AGNR). The third-nearest neighbor parametrization from [38] (green bands, `3nn-o`) provides the most accurate description. Overall, TB provides a good description of the carbon $\pi$-electron system.

### 2.3. The Hubbard model

While the TB method is a well-established starting point for describing the electronic structure of carbon-based systems, the method itself cannot account for the emergence of $\pi$-magnetism due to the neglect of electron interactions. One way to include them is called the Hubbard model.

The Hubbard model was introduced in 1963 as an approximate description of electron correlation effects in narrow energy bands of solids, taking into account the atomistic nature in a minimal fashion [39]. It was initially proposed to understand the properties of transition and rare-earth metals with partly filled $d$- and $f$-bands. However, despite its apparent simplicity it contains very rich physics, and has been useful to describe phenomena such as correlated metal–insulator transitions, magnetism, and superconductivity.

In the (fermionic) Hubbard model one adds to the TB Hamiltonian $\hat{H}_0$ a term that accounts for short-range electron interactions. The model is defined by the Hamiltonian [39]:

$$\hat{H} = \hat{H}^0 + U_0 \sum_i \hat{n}_{i\uparrow}\hat{n}_{i\downarrow}, \tag{3}$$

where $\hat{n}_{i\sigma} = \hat{c}^\dagger_{i\sigma}\hat{c}_{i\sigma}$ is the number operator for site $i$ and $U_0 > 0$ is the onsite Coulomb repulsion energy. The model thus ignores long-range Coulomb effects by only considering the interaction energy when two electrons occupy the same orbital.

Solving the Hubbard model is in general a difficult problem due to the quartic structure of the operators appearing in (3) and the exponential growth of Fock-space with system size, thus sharing challenges with full many-body descriptions (section 2.5). In order to solve the Hubbard model for moderately large nanographenes, methods based on configuration interaction in the so-called complete active space (CAS) have been developed [40, 41]. This approximation consists of splitting the single-particle spectrum into 'frozen' low- and high-energy sectors and an active space which is handled numerically exact to capture the low-energy states accurately. For example, CAS(6, 6) formed by six electrons in six single-particle states was used to describe the low-energy states of triangulene dimers [42] and trimers [43]. The CAS-Hubbard approach to zero-modes in nanographenes has been useful to establish exchange rules for diradicals [44].

#### 2.3.1. Example: half-filled Hubbard dimer.

A simple, illustrative example of analytic solution of the Hubbard model is the case of a half-filled dimer, i.e. a system composed of two electronic orbitals and occupied by two electrons. We define it as:

$$\hat{H} = \sum_{\alpha=L,R}\sum_\sigma \varepsilon_\alpha \hat{n}_{\alpha\sigma} - t\sum_\sigma \left(\hat{c}^\dagger_{L\sigma}\hat{c}_{R\sigma} + \text{h.c.}\right) + \sum_{\alpha=L,R} U_\alpha\, \hat{n}_{\alpha\uparrow}\hat{n}_{\alpha\downarrow}, \tag{4}$$

where $\varepsilon_\alpha$ the single-particle energy of orbital $\alpha \in \{L,R\}$, $t$ the effective hopping matrix element between the orbitals, and

$$U_\alpha = U_0 \int d\mathbf{r}\, |\psi_\alpha(\mathbf{r})|^4, \tag{5}$$

the effective Coulomb repulsion for each orbital. Projecting this Hamiltonian on the following basis of two-electron states:

$$\left\{\hat{c}^\dagger_{L\uparrow}\hat{c}^\dagger_{R\downarrow}|0\rangle,\ \hat{c}^\dagger_{L\downarrow}\hat{c}^\dagger_{R\uparrow}|0\rangle,\ \hat{c}^\dagger_{L\uparrow}\hat{c}^\dagger_{L\downarrow}|0\rangle,\ \hat{c}^\dagger_{R\uparrow}\hat{c}^\dagger_{R\downarrow}|0\rangle\right\}, \tag{6}$$

where $|0\rangle$ represents the vacuum state, we arrive at the simple matrix form:

$$\hat{H} = \begin{pmatrix} \varepsilon_L+\varepsilon_R & 0 & -t & -t \\ 0 & \varepsilon_L+\varepsilon_R & t & t \\ -t & t & 2\varepsilon_L+U_L & 0 \\ -t & t & 0 & 2\varepsilon_R+U_R \end{pmatrix}, \tag{7}$$

which is readily diagonalized. In the symmetric limit $\varepsilon_L = \varepsilon_R = 0$ and $U_L = U_R = U$ the eigenenergies are:

$$E_{S_0} = U/2 - \sqrt{(2t)^2 + (U/2)^2}, \tag{8a}$$

$$E_T = 0, \tag{8b}$$

$$E_{S_1} = U, \tag{8c}$$

$$E_{S_2} = U/2 + \sqrt{(2t)^2 + (U/2)^2}, \tag{8d}$$

and the corresponding eigenstates:

$$|S_0\rangle \propto \left(\alpha\left[\hat{c}^\dagger_{L\uparrow}\hat{c}^\dagger_{R\downarrow} - \hat{c}^\dagger_{L\downarrow}\hat{c}^\dagger_{R\uparrow}\right] + \hat{c}^\dagger_{L\uparrow}\hat{c}^\dagger_{L\downarrow} + \hat{c}^\dagger_{R\uparrow}\hat{c}^\dagger_{R\downarrow}\right)|0\rangle, \tag{9a}$$

$$|T\rangle = \frac{1}{\sqrt{2}}\left(\hat{c}^\dagger_{L\uparrow}\hat{c}^\dagger_{R\downarrow} + \hat{c}^\dagger_{L\downarrow}\hat{c}^\dagger_{R\uparrow}\right)|0\rangle, \tag{9b}$$

$$|S_1\rangle = \frac{1}{\sqrt{2}}\left(\hat{c}^\dagger_{L\uparrow}\hat{c}^\dagger_{L\downarrow} - \hat{c}^\dagger_{R\uparrow}\hat{c}^\dagger_{R\downarrow}\right)|0\rangle, \tag{9c}$$

$$|S_2\rangle \propto \left(\beta\left[\hat{c}^\dagger_{L\uparrow}\hat{c}^\dagger_{R\downarrow} - \hat{c}^\dagger_{L\downarrow}\hat{c}^\dagger_{R\uparrow}\right] + \hat{c}^\dagger_{L\uparrow}\hat{c}^\dagger_{L\downarrow} + \hat{c}^\dagger_{R\uparrow}\hat{c}^\dagger_{R\downarrow}\right)|0\rangle, \tag{9d}$$

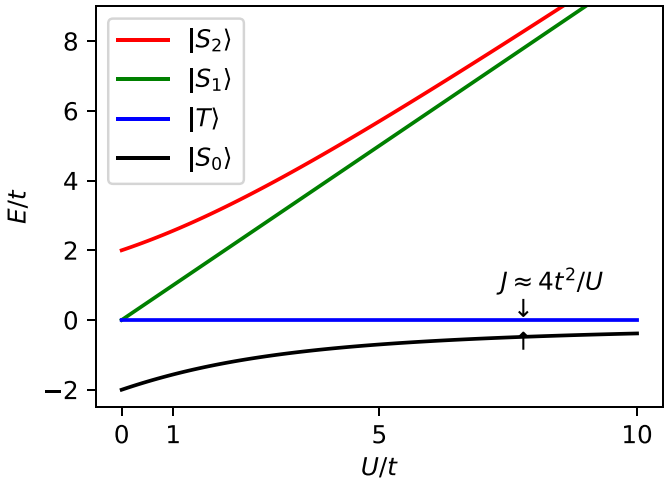


**Figure 3.** Energy spectrum of the half-filled Hubbard dimer. In absence of a magnetic field the ground state is a singlet $|S_0\rangle$ and the first excited state a triplet $|T\rangle$. In the limit of large $U/t$ the low-energy spectrum can be described by the Heisenberg spin dimer with antiferromagnetic exchange coupling $J = 4t^2/U$.

where $\alpha = -2t/E_{S_0}$ and $\beta = -2t/E_{S_2}$. Here $|S_i\rangle$ can be identified as the singlet states while $|T\rangle$ is the $S_z = 0$ triplet state. An illustration of the energy spectrum of the Hubbard dimer is shown in figure 3.

In the limit $U/t \to 0$, where $\alpha \to 1$, we see that the ground state is an equal mix of the open- and closed-shell configurations. Conversely, in the limit $U/t \to \infty$, where $\alpha \to \infty$, only the open-shell configuration remains. Here the ground state energy can be expanded in $t$ to read:

$$E_{S_0} \to -4t^2/U. \tag{10}$$

This allows to map the low-energy spectrum in this limit onto the antiferromagnetic Heisenberg model for a spin-1/2 dimer:

$$\hat{H}_{\text{eff}} = J\left(\vec{\mathbf{S}}_L \cdot \vec{\mathbf{S}}_R - \frac{1}{4}\right), \tag{11}$$

where $\vec{\mathbf{S}}_i$ is the spin-1/2 operator for site $i$ and the exchange coupling can identified as $J = 4t^2/U$. From the relations $2\vec{\mathbf{S}}_L \cdot \vec{\mathbf{S}}_R = (\vec{\mathbf{S}}_L + \vec{\mathbf{S}}_R)^2 - \vec{\mathbf{S}}_L^2 - \vec{\mathbf{S}}_R^2$ and $\vec{\mathbf{S}}^2 = S(S+1)$, it is easy to see that the eigenenergies of $\hat{H}_{\text{eff}}$ correspond to $-J$ for the singlet ($S = 0$) and 0 for the triplets ($S = 1$), exactly as derived above for the Hubbard dimer.

### 2.4. Mean-field Hubbard approximation

The Hubbard model can in principle be solved by numerically exact diagonalization, but the Hilbert space grows exponentially with the number of lattice sites. This makes a brute-force approach to even small nanographenes impractical.

Instead a dramatic simplification is achieved if one resorts to the mean-field approximation. By defining the occupation operators $\hat{n}_{i\sigma} = \langle \hat{n}_{i\sigma} \rangle + \delta\hat{n}_{i\sigma}$ in terms of the fluctuations

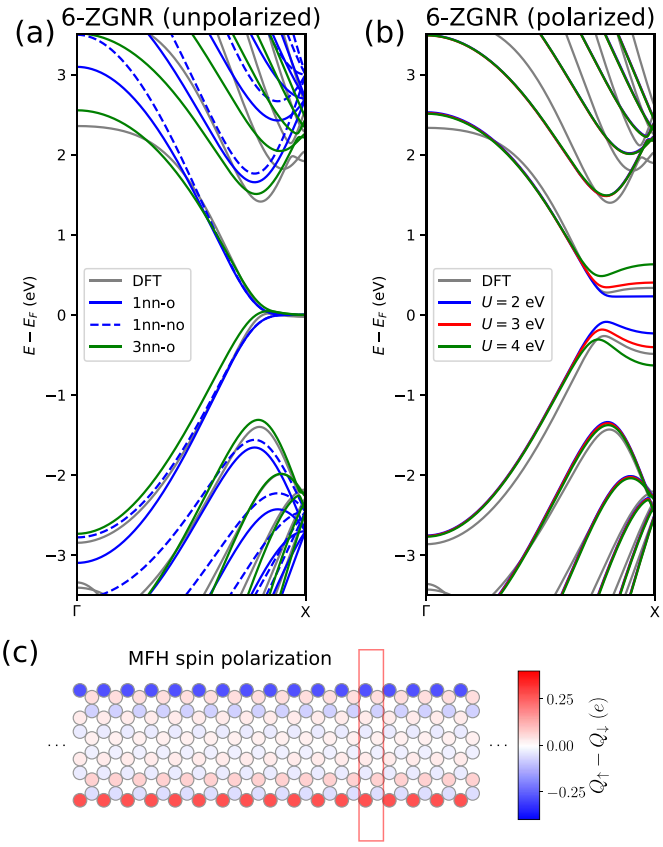


**Figure 4.** Comparison of electronic band structures from MFH and DFT for a hydrogen-terminated 6-ZGNR. (a) For spin-degenerate (unpolarized) calculations the ZGNR is metallic and displays a flat band towards $X$. The TB parameters are the same as those of figure 2. (b) Spin-polarized calculations leads to symmetry-broken solutions with edge-polarization [45, 54] and the opening of a correlation gap. The MFH model here is based on the third-nearest neighbor model (`3nn-o`) and $U$ is varied in the range 2–4 eV (colored bands). In both panels the gray bands correspond to SIESTA [35] DFT-GGA calculations using a DZP basis set and lattice constant of $a = 2.460$ Å. (c) Spin polarization from MFH calculations (3nn-o, $U = 3$ eV). The unit cell is indicated by the red box.

around their average values, one can write the product of operators as:

$$\begin{aligned}\hat{n}_{i\uparrow}\hat{n}_{i\downarrow} &= (\langle \hat{n}_{i\uparrow} \rangle + \delta\hat{n}_{i\uparrow})(\langle \hat{n}_{i\downarrow} \rangle + \delta\hat{n}_{i\downarrow}) \\ &= \hat{n}_{i\uparrow}\langle \hat{n}_{i\downarrow} \rangle + \langle \hat{n}_{i\uparrow} \rangle \hat{n}_{i\downarrow} - \langle \hat{n}_{i\uparrow} \rangle \langle \hat{n}_{i\downarrow} \rangle + \delta\hat{n}_{i\uparrow}\delta\hat{n}_{i\downarrow} \\ &\approx \hat{n}_{i\uparrow}\langle \hat{n}_{i\downarrow} \rangle + \langle \hat{n}_{i\uparrow} \rangle \hat{n}_{i\downarrow} - \langle \hat{n}_{i\uparrow} \rangle \langle \hat{n}_{i\downarrow} \rangle,\end{aligned} \tag{12}$$

where the fluctuations (last term) has been neglected. This leads to the mean-field Hubbard (MFH) model of the form:

$$\hat{H}_{\text{MFH}} = \hat{H}_0 + U\sum_i (\hat{n}_{i\uparrow}\langle \hat{n}_{i\downarrow} \rangle + \langle \hat{n}_{i\uparrow} \rangle \hat{n}_{i\downarrow} - \langle \hat{n}_{i\uparrow} \rangle \langle \hat{n}_{i\downarrow} \rangle). \tag{13}$$

An example of MFH results for the band structure of a 6-atom wide zigzag GNR (ZGNR) is shown in figure 4 (colored bands). It is well-established that symmetry-broken solutions (figure 4(b)) are in very good agreement with DFT-GGA calculations (gray bands) when using $U \sim 3$ eV on top

of the third-nearest neighbor parametrization [3, 38]. The MFH model has been shown as a useful model to understand the emergence of magnetism in $sp^2$ carbon systems [3, 24, 38, 45–52]. A free implementation of MFH in Python is available [53].

### 2.5. Wave-function based methods and many-body theory

The problem of electron correlation in open-shell nanographenes can also be addressed with full *ab initio* quantum chemistry approaches. This is particularly pertinent when strong correlation effects are at play. However, the computational cost of traditional wave-function based methods (configuration interaction, coupled cluster, multi-configurational self-consistent fields, etc) typically scale very unfavorable with the system size and are thus limited to rather small molecules. Examples of quantum chemistry calculations for graphene nanoislands include CAS-SCF and multireference NEVPT2 methods [55], restricted active space configuration interaction (RASCI) [56], and multi-reference averaged quadratic coupled cluster method (MR-AQCC) [57]. Other approaches are based on quantum chemical density matrix renormalization group (DMRG) that allows to address the full $\pi$-orbital space of large nanographenes [58–62]. Many-body diagrammatic techniques based on the GW approximation was also applied to the Hubbard model to describe correlation effects in GNR heterojunctions [63].

Another important aspect beyond the properties of *isolated* nanographenes is the impact of the interaction with a supporting surface. This can for instance give rise to Kondo-like phenomena on metal surfaces arising from the coupling of a magnetic system with the conduction electrons in the substrate. This situation has been described theoretically based on the multi-orbital Anderson model in the non-crossing approximation [43, 64, 65].

### 2.6. Topological band analysis

Another useful way to analyze, understand or predict radical states in $sp^2$-carbon structures is through topology [26, 66–71]. The topological classes are characterized by a $\mathbb{Z}_2$ invariant that takes on the values 0 or 1 for trivial and nontrivial characters, respectively. The relevant quantity to characterize the topological class of one-dimensional (1D) systems is the Zak phase $\gamma_n$ of its $n$ occupied bands, which is obtained from an integral of the Berry connection across the 1D Brillouin zone [72, 73]:

$$\gamma_n = i\frac{2\pi}{a}\int_{-\pi/a}^{\pi/a} dk \left\langle u_{nk}\left|\frac{\partial}{\partial k}\right|u_{nk}\right\rangle, \tag{14}$$

where $k$ is the wave vector, $a$ is the unit cell size, and $u_{nk}$ is the periodic part of the electron Bloch wave function in band $n$. Note that for systems with band-crossings or degenerate states there is an arbitrariness to the definition of the Zak phase for the individual bands. However, the total phase $\gamma = \sum_{n\in\mathrm{occ}}\gamma_n$ (i.e. summed over occupied bands) is invariant and unaffected by this arbitrariness as long as the filled and empty bands do not intersect [73].

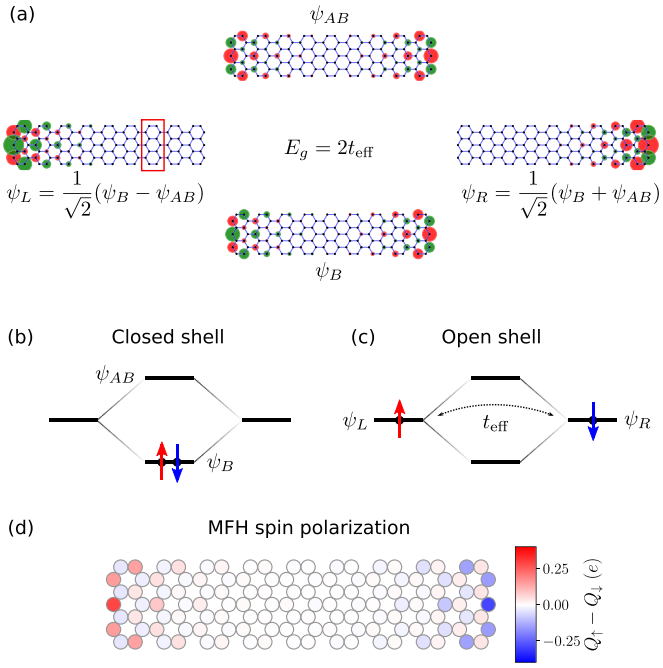


**Figure 5.** Illustration of the emergence of zero-modes in a finite 7-AGNR that belongs to the topology class $\mathbb{Z}_2 = 1$. The corresponding unit cell is indicated by the red box. (a) The bonding and antibonding single-particle orbitals $\psi_B$ and $\psi_{AB}$ (center column) fall inside the energy gap of the infinite ribbon and originate from the hybridization of two zero-modes $\psi_L$ and $\psi_R$ (outer columns) through the effective tunnel coupling $t_{\mathrm{eff}}$. (b) Simple picture of the closed-shell configuration for short 7-AGNRs ($t_{\mathrm{eff}} \gg U_B$), and (c) open-shell configuration for long 7-AGNRs ($t_{\mathrm{eff}} \ll U_B$). (d) Calculated spin polarization with MFH using $U = 3$ eV.

The Zak phase $\gamma$ depends on the choice of shape and origin of the unit cell and can in general take any value. However, if the unit cell possesses inversion or mirror symmetry, it is possible to choose the origin such that $\gamma$ (mod $2\pi$) is quantized to either 0 or $\pi$. The corresponding $\mathbb{Z}_2$ invariant is then obtained from:

$$(-1)^{\mathbb{Z}_2} = e^{i\gamma}. \tag{15}$$

The $\mathbb{Z}_2$ invariant is also related to the parity of the Bloch wave functions at the time-reversal invariant momentum points $\Gamma$ and $\pi/a$ by [66, 69, 71]:

$$(-1)^{\mathbb{Z}_2} = \prod_{n\in\mathrm{occ}} \langle\psi_{n\Gamma}|\widehat{P}|\psi_{n\Gamma}\rangle\langle\psi_{n\pi/a}|\widehat{P}|\psi_{n\pi/a}\rangle, \tag{16}$$

where $\widehat{P}$ is the parity operator (applying to either inversion or mirror symmetry) and $\psi_{nk}$ is the wave function of the $n$th occupied band at momentum $k$.

According to the bulk-boundary correspondence, at the interface between materials belonging to different topology classes one (or an odd number) of localized zero-energy modes will emerge. Such in-gap states in $sp^2$ carbon structures are also manifestations of $\pi$-radicals [26, 66–71].

As an example, applying these concepts to the band structure of a 7-AGNR described by the unit cell shown by the red box in figure 5(a), one concludes that this ribbon belongs to

the topological class $\mathbb{Z}_2 = 1$ [66]. As vacuum is trivial $\mathbb{Z}_2 = 0$, one zero-mode edge state is expected at each zigzag terminus. To illustrate this, the low-energy wave functions for a finite 7-AGNR are superimposed on the structures in figure 5(a). Two states, $\psi_B$ and $\psi_{AB}$ are found inside the energy gap of the infinite 7-AGNR (figure 2(b)), corresponding to the bonding and antibonding combinations of the topological zero-modes $\psi_L$ and $\psi_R$ coupled through the effective tunnel matrix element $t_{\text{eff}}$. The end states are readily identified by the proper linear combinations. As sketched in figures 5(b) and (c) this system may adopt either a closed- or open-shell configuration depending on the strength of the Coulomb repulsion energy of the bonding orbital $U_B = U\int |\psi_B|^4 dr$ with respect to the hybridization energy $|2t_{\text{eff}}|$. A crossover occurs naturally as the length of the GNR is increased due to the exponentially decaying matrix element $|t_{\text{eff}}|$. The characteristic spin polarization map computed from the local difference between up and down spin populations with MFH is shown in figure 5(d) for $U = 3$ eV.

## 3. Counting rules

### 3.1. Ovchinnikov's rule and Lieb's theorem

Graphene is a so-called bipartite system in which $sp^2$-hybridized carbon atoms are arranged in two alternating hexagonal sublattices. That is, carbon atoms of one sublattice are covalently bound only to carbons of the opposite sublattice. The low-energy electronic states that prevalently determine most physico-chemical processes of graphene and its nanostructured derivatives are $\pi$-orbitals that arise from the hybridization of the carbon $p_z$ electrons. Each $sp^2$-hybridized carbon atom has one $p_z$ electron. Indeed, as described in the previous sections, a one-orbital approximation with the TB or MFH models has been extremely successful to describe the properties of graphene and its nanostructured derivatives [3, 74].

In a bipartite structure, each $p_z$ electron can only form $\pi$-bonds with electrons belonging to atoms of the opposite sublattice. It automatically follows that, if the two sublattices have a different number of atoms, the electrons will not be able to bind pairwise. The electrons that remain unpaired become $\pi$-radicals with an associated spin $S = 1/2$. This is an intuitive basis for Lieb's theorem [75], which in turn follows from Ovchinnikov's rule [76]. The theorem states that bipartite systems with repulsive electron-electron interactions ($U > 0$), as is the case of graphene and carbon-based nanostructures, will display a ground state with net spin according to:

$$S = \frac{1}{2}|N_A - N_B|, \tag{17}$$

where $N_A$ and $N_B$ are the number of atoms belonging to each sublattice. A molecular system with an unbalanced amount of atoms in each sublattice will thus necessarily display a net spin.

A very intuitive example of such a system is defective graphene, in which the local removal of one $p_z$ electron endows the defect with magnetic properties [77]. Experimentally, the removal of a $p_z$ electron from graphene has been obtained

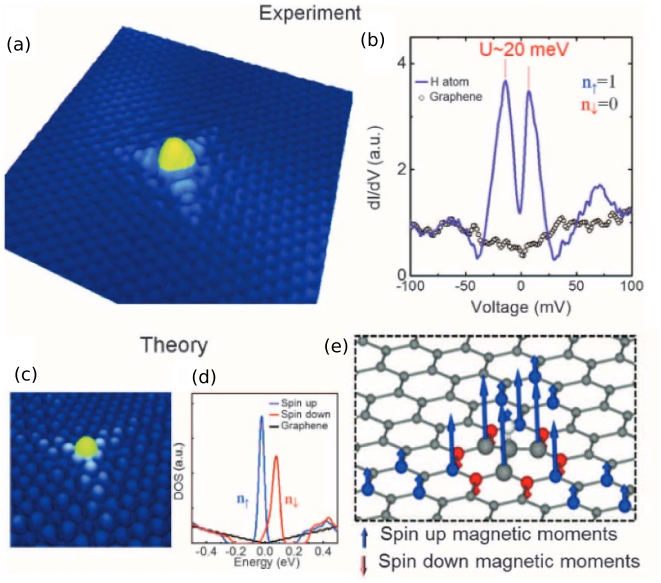


**Figure 6.** (a) STM topography of a single H atom chemisorbed on neutral graphene. (b) $dI/dV$ spectrum measured on the H atom, showing a fully polarized peak at $E_F$, and measured on bare graphene far from the H atom. (c) DFT-simulated STM image and (d) density of states of an H atom chemisorbed on neutral graphene. (e) Calculated magnetic moments induced by H chemisorption (the lengths of the arrows signify the relative magnitudes of the magnetic moments). From [78]. Reprinted with permission from AAAS.

by different means, like forming atomic vacancies by low-energy ion bombardment in combination with an annealing treatment [20], or by $sp^3$ rehybridization of a C atom upon hydrogenation when exposed to atomic hydrogen [78]. A scanning tunneling microscopy (STM) image for the latter case is shown in figure 6, and a spectroscopic analysis on top of it clearly revealed the Coulomb gap of the magnetic state (figure 6(b)). Theoretical modeling of such a hydrogenated defect not only nicely reproduces its contrast in STM images (figure 6(c)) but also the DOS in correlation to the STS spectra (figure 6(d)) [78]. The spin density distribution is further displayed in figure 6(e). In agreement with the experimental and calculated STM images, the magnetic state and therefore the net spin extends over several nm, but almost exclusively on carbon atoms of the sublattice not hosting the extra hydrogen (figure 6(e)). Only a residual oppositely oriented spin density is observed on the sublattice of the hydrogenated atom, which is a manifestation of the spin polarization caused by the exchange interaction of the unpaired electron with the fully populated states [3]. For cases in which two such defects are close to one another, DFT calculations and experiments reveal a clear magnetic signal and the spin's ferromagnetic alignment (total spin $S = 1$) for defect pairs on the same sublattice, and a totally quenched magnetic signal when they are on opposite sublattices [78]. These findings are in perfect agreement with Lieb's theorem, which predicts a ground state with $S = 0$ if the defects are on opposite sublattices, and with $S = 1$ if they are located on the same sublattice. It is important to keep in mind, however, that Ovchinnikov's rule and Lieb's theorem no longer apply for doped systems [79].

### 3.2. *Nullity*

Another simple and very useful counting rule to predict magnetic properties in electronically neutral carbon-based nanostructures is the analysis of the structure's so-called 'nullity' ($\eta$). Nullity represents the number of zero-energy states that result from solving the nearest-neighbor TB Hamiltonian for a specific nanostructure, dating back to early work on the spectral properties of unsaturated hydrocarbons [80]. Zero-energy states fulfill the Stoner criterion [3] and thus undergo spin-polarization for any $U>0$ to avoid the instability associated with low energy electrons, since alternative mechanisms like a Peierls distortion or charge ordering have been shown to be inefficient in the case of graphene nanostructures [3, 81]. As a consequence, nullity can be used to predict the number of $\pi$-radicals in a system, which is given by:

$$\eta = 2\alpha - N, \tag{18}$$

where $\alpha$ is the maximum number of sites that are not nearest neighbors to each other and $N$ is the total number of sites. Whereas for bipartite structures $\alpha$ often coincides with the number of atoms belonging to the dominant sublattice (or of either sublattice if they display the same number of sites), that is not always the case. This is shown by way of example in figure 7 with the iconic 'Clar's goblet' molecule.

We note that the nullity can be understood in terms of two contributions $\eta = \eta_{\text{pre}} + \eta_{\text{sup}}$, where $\eta_{\text{pre}} = |N_A - N_B|$ is the *predictable* number of zero modes from sublattice imbalance and $\eta_{\text{sup}} \in 2\mathbb{Z}$ is the remaining *supernumerary* zero modes (of topological origin) that come in pairs [82].

Figure 7(a) shows the molecular structure of Clar's goblet, differentiating with blue and red colors the sites belonging to either sublattice, $N_A$ and $N_B$. Following Lieb's theorem, the total spin of the molecule corresponds to $S=0$. However, counting the maximum number of non-adjacent sites $\alpha$ as displayed in figure 7(b), we obtain $\alpha = 20$. Given the total number of atoms $N=38$, the system's nullity amounts to $\eta = \eta_{\text{sup}} = 2$. This is corroborated with TB calculations, which indeed predict the presence of two zero-energy states (figure 7(c)) that become spin-polarized as Coulomb interactions are included with the Hubbard model (figure 7(d)). This is not in contradiction with the prediction of Lieb's theorem, but implies that the two $\pi$-radicals are antiferromagnetically oriented. This antiferromagnetic spin orientation is also confirmed with theoretical calculations as displayed in figure 7(h), in which the blue and red colors now denote the spin density with up and down orientation, respectively. The antiferromagnetic alignment of the two radical states may seem in contradiction with Hund's rule, according to which the spins should align ferromagnetically. The explanation of this apparent conflict is that the two spins can be considered as belonging to independent systems, each comprising one sublattice. Indeed, the stabilizing bonding interaction between nearest neighbor C atoms is promoted by the antiferromagnetic alignment of their spins (as opposed to the destabilizing effect of equal spins on adjacent sites) [83], which in bipartite structures leads to two sublattices displaying opposite spin orientations. The predictions from Lieb's theorem can therefore be understood as following Hund's rule separately on the two sublattices, and with the spins of each sublattice aligned antiferromagnetically due to a superexchange mechanism [3]. Indeed, as can be observed from figure 7(h), the up and down spin densities on Clar's goblet are each distributed over different sublattices [3, 24].

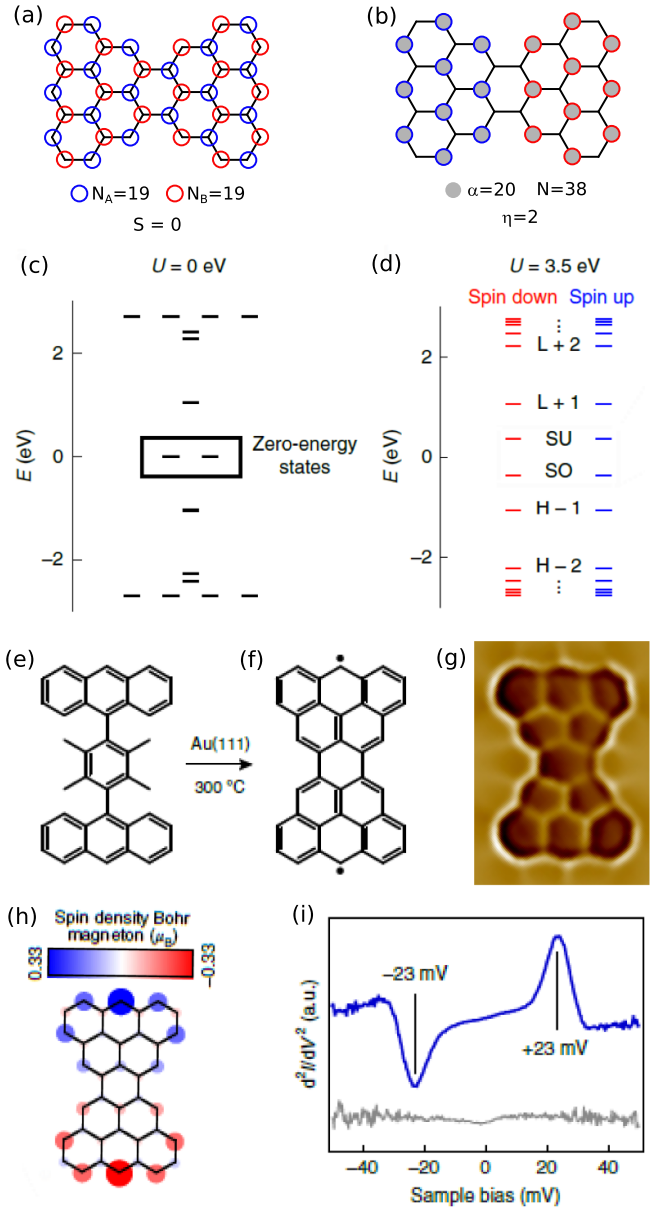


**Figure 7.** (a) Structure of Clar's goblet with carbon atoms belonging to sublattice A (marked in blue) and to sublattice B (marked in red). (b) Atoms that maximize the number of sites that are not nearest neighbor to each other, marking with the colored perimeter the sublattice they belong to. (c) Orbital energy spectrum of Clar's goblet calculated with TB and (d) with the MFH model. (e) Reactant utilized for the first successful synthesis of the Clar's goblet. (f) Chemical structure and (g) measured bonding structure of the product. (h) Calculated spin density distribution according to the MFH model. (i) $d^2/dV^2$ spectra acquired on Clar's goblet in the vicinity of the Fermi level, revealing inelastic spin excitation at $\pm 23$ mV. (c)–(i) Reproduced from [24], with permission from Springer Nature.

Although Clar's goblet was theoretically devised already in 1972 [23] it was not until 2020 that such molecule has been synthesized and characterized [24]. Starting from the reactant displayed in figure 7(e), its deposition and subsequent annealing on a Au(111) surface led to the formation of Clar's goblet (figure 7(f)), which could ultimately be imaged with bond-resolving microscopy as shown in figure 7(g) [24]. The magnetism associated to the $\pi$-radicals was proved by the characterization of inelastic singlet-to-triplet spin-flip excitations (figure 7(i)) that furthermore revealed a remarkably large exchange coupling of 23 mV.

### 3.3. Clar sextets

It is well-established that aromatization of conjugated structures increases their band gap and overall stability. An easy way to quantify the aromaticity with simple counting rules is analyzing the number of Clar sextets (a six-membered carbon ring comprising three conjugated $\pi$-bonds) contained within a molecular structure [23, 84, 85]. The energetically favored and therefore dominant resonance structure of polyaromatic hydrocarbons is supposed to be the structure displaying the largest number of Clar sextets, which is termed as the 'Clar formula'. The aromatic stabilization energy per Clar sextet is estimated to be in the order of $\approx$90 kJ mol$^{-1}$ [86, 87], which happens to be about one third of the energy of a C–C $\pi$-bond ($\approx$270 kJ mol$^{-1}$), as assessed from the rotational barrier of ethylene [87, 88]. From this comparison one may expect that the breaking of a $\pi$-bond, along with the associated generation of two $\pi$-radicals, may be favored if three or more additional Clar sextets can be gained [85, 89]. As will be shown in later sections with a number of examples, the ratio of three sextets per broken $\pi$-bond (that is, three sextets per pair of radicals) indeed marks an approximate threshold at which the molecules adopt an open-shell configuration. The larger the molecular structures are, the more possibilities there are to generate a sufficient number of Clar sextets to compensate for the generation of radicals, hinting at the stronger tendency of larger molecules to display radicals.

It must be kept in mind, however, that this proposed threshold is only indicative and may vary from structure to structure. Some of the factors affecting this threshold will be elaborated on in later sections.

## 4. Experimental approaches

### 4.1. On-surface synthesis

A key part in the booming development of carbon-based magnetism has been clearly the progress in the synthetic capabilities. As will be discussed later in more detail, carbon nanostructures with magnetic properties are normally very reactive, which complicates their synthesis and characterization. In this respect, OSS performed under vacuum conditions offers opportunities that were previously unavailable to more conventional approaches. The inert vacuum environment, along with the generally stabilizing effect of the supporting substrate surface, allow for the synthesis of carbon nanostructures that under different conditions would either degrade extremely fast or cannot be directly achieved. In spite of being a relatively young research field, OSS has been reviewed extensively and we refer the reader to more detailed descriptions on the virtues and possibilities offered by this approach [15–18].

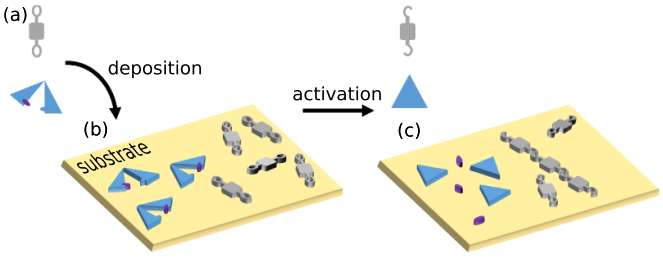


**Figure 8.** (a) Schematic representation of two reactant molecules. (b) Reactant molecules deposited onto a substrate. (c) Sample after the application of stimuli to activate the reactions, which occur at the intramolecular level for the blue reactants (along with the generation of byproducts represented by the purple molecular segments), and promote intermolecular coupling reactions for the grey reactants.

In short, the OSS approach consists in the deposition of appropriately designed molecular reactants (figure 8(a)) onto a substrate surface (figure 8(b)), on top of which the molecules react and remain adsorbed (figure 8(c)). Within this frame, there is huge space for variations. Most of all with regard to the starting reactants, but also for the deposition step and the activation method. The starting reactants are designed so as to form the target product either by intramolecular reactions (as represented with the blue reactants in figure 8), by intermolecular coupling processes (as represented with the grey reactants in figure 8), or by combinations thereof. The utilized reactions (and the associated functional groups required on the precursors) are manifold [15–18], but the most common ones applied to date in the synthesis of magnetic carbon-nanostructures are cyclodehydrogenation reactions and dehalogenative aryl–aryl coupling, which is commonly referred to as Ullmann coupling. When it comes to the deposition step, the most common approach for surfaces under vacuum is sublimation from Knudsen cells. However, there are also alternatives like the deposition from the gas phase through leak-valves [90], or from solution by controlled injection sources [91–93]. Finally, for the activation step the vast majority of reported works utilize heat. Nevertheless, local activation by scanning probes have also been proved successful and provide exquisite control over the reaction process [94–96]. Alternatively, photoactivation is another option that has also been proved successful and, although hardly exploited to date in OSS, bears great potential [97].

The fact that the products obtained by OSS remain adsorbed on the surface is probably the most important difference with respect to heterogeneous catalysis [18], for which chemical reactions are equally supported/catalyzed by solid substrates, but the products desorb again after reacting. Although this difference may at first seem minor, it has important implications. On the one side, it severely limits the scalability of OSS as a production method, since it can be considered

as heterogeneous catalysis suffering from poisoning and the transfer of products onto different surfaces or environments requires relatively complicated protocols [15]. Besides, also reaction byproducts may remain on the surface (see for example the purple parts of the blue reactant in (figure 8), which may in turn be detrimental for the characterization or for the functionality of the system or following reactions. However, on the positive side, it allows using a battery of surface science techniques (specially for OSS performed under vacuum) that can result in a delightfully detailed characterization of the products even at the single molecule level by, e.g. SPM. Although the OSS approach can be applied in different environments, it is most commonly performed under vacuum, which is certainly the case for the synthesis of magnetic carbon nanostructures due to their mentioned lack of stability. The progress achieved within the last few years with the OSS of carbon nanostructures displaying magnetic properties or at least with zigzag edges (which as mentioned earlier generally promote the appearance of magnetism in the nanostructures) has been specifically summarized in recent review articles [4, 19].

### 4.2. Characterization techniques

As mentioned above, most of the progress achieved in the field has been thanks to the new synthetic capabilities offered by OSS under vacuum. As occurs with conventional chemistry, also in OSS the yield with which the target product is obtained varies largely from system to system. However, because target as well as byproducts remain on the surface and no means have been developed yet for purification processes, ensemble averaging measurement techniques may be hampered depending on the nature and amount of byproducts contributing to it. This is one of the reasons for which SPM are the most popular characterization techniques applied in the wider field of OSS, as well as more specifically to the study of magnetic carbon nanostructures. Nevertheless, SPM techniques specifically developed to directly measure the magnetism with spatial resolution like spin-polarized STM (SP-STM) [98] or electron-spin-resonance STM (ESR-STM) [99] have not yet been applied successfully to carbon nanostructures. Only ensemble ESR measurements have provided direct measurement of magnetism and the coherent manipulation of edge states on functionalized GNRs [7]. A magnetic signal that has been experimentally measured with spatial resolution by means of SPM is the Zeeman splitting under magnetic fields [100, 101]. Other than that, most evidences for magnetism in carbon nanostructures by SPM-based measurements with single molecule resolution have been obtained by indirect means.

The conceptually simplest signal utilized to indirectly prove the single occupation of molecular orbitals and the associated magnetism of molecular nanostructures is the presence of a Coulomb gap. An example thereof is shown in figures 9(a)–(c) [102]. Figure 9(a) displays STS data revealing the onsets of the valence and conduction bands (blue curve) of 7-AGNRs and, at the zigzag ends (red curve), two resonances within the ribbon's band gap below and above the Fermi level, respectively. These resonances are associated with magnetic GNR end states, whose origin was briefly outlined in figure 5 and will be discussed further in later sections. The resonance below the Fermi level (negative sample bias) corresponds to the singly occupied state as probed when extracting the electron by the scanning probe, whereas the one above the Fermi level (positive sample bias) is the same state as probed when injecting a second electron into the magnetic state. The second electron suffers the Coulomb repulsion from the first electron and the resonance thus appears at an energy $U$ above the negative resonance. The similar spatial distribution of the two resonances (figure 9(b)) supports their common origin from the same singly occupied radical state, and final proof is given by the good match with the calculated density of states (DOS) predicted for those magnetic end states (figure 9(c)) [102]. The magnitude of the Coulomb gap depends on several parameters, one of which is the screening potential of the state's environment. Magnetic states in molecules adsorbed directly on metals will, e.g. display much smaller Coulomb gaps than if adsorbed on a thin dielectric layer [102]. Another important parameter is the electronic state's extension. That is, the more extended the orbital is that hosts the unpaired electron, the lower the Coulomb repulsion will be if filled with a second electron [103]. All in all, the magnitudes of reported Coulomb gaps can vary from the meV range, as found for example for point defects in graphene on SiC substrates [78], to the eV range in more localized states of molecules adsorbed on metals [24, 42], which can grow to several eV by simply intercalating some thin dielectric layer between molecule and metal substrate [22, 102].

An alternative signal that is often used as proof for magnetism is a zero-bias resonance, namely a so-called Kondo resonance, that can appear when magnetic states interact with a metallic substrate [105–107]. A magnetic state with energy $\varepsilon_0$ hosts an unpaired electron with spin $S = 1/2$ whose $z$-component displays up or down orientation. Quantum mechanically there is a limited time of the order of $h/|\varepsilon_0|$ or $h/|\varepsilon_0 + U|$ (typically some femtoseconds) during which the magnetic state can be empty or doubly occupied, respectively [105–107]. The former requires the electron in the magnetic state to populate an empty state of the substrate, whereas the latter requires the population of the magnetic state by a second electron from the metal. Either case can subsequently relax leaving the magnetic state with a single electron of reversed spin. That is, the impurity's spin state is constantly fluctuating and a combination of all these spin exchange processes results in the appearance of an additional Kondo resonance at the Fermi energy that can thus be directly related to the magnetic moment of the screened state [105–107].

An example of such a Kondo resonance in carbon nanostructures is shown in figures 9(d)–(f), in particular at the junctions of chiral GNRs [52]. Such junctions in principle display two radical states. However, one often appears passivated by hydrogen, which leaves a single magnetic state with $S = 1/2$ per junction. Conductance spectra at those positions display a clear zero-energy resonance that corresponds to a Kondo peak and therefore proves the presence of the local spin (black curves in figure 9(f)).

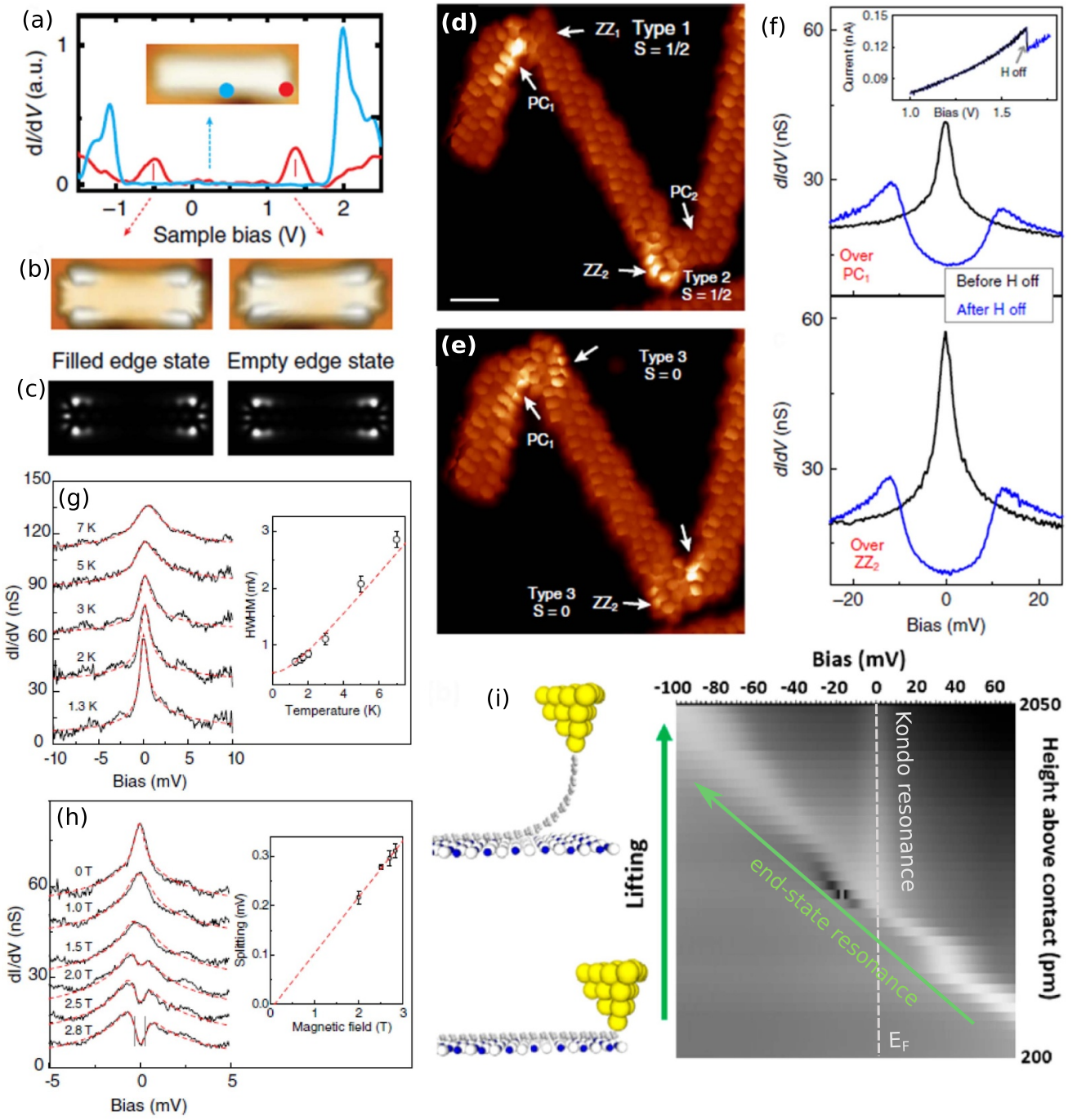


**Figure 9.** (a) Conductance point spectra in the center (blue) and towards the ends (red) of a zigzag-terminated 7-AGNR on NaCl decoupling layers on Au(111). The exact location for each of the spectra is shown in the inset. In the central part the signal reveals the valence and conduction band onsets, whereas the spectra at the reveal in-gap end states. (b) Conductance maps of the two in-gap states. (c) Calculated density of states for the end states at 4 Å above the carbon backbone. (d) Constant height STM image of two GNR heterojunctions, each with one extra H atom that passivates a radical. (e) Similar STM image after tip-induced removal of the extra H atoms. (f) Conductance point spectra at each of the two junctions before (black line) and after (blue line) removal of the H atom. The inset shows the current trace during removal of one of the H atoms. (g) Temperature dependence of the Kondo resonance for an extended triangulene molecule. The inset plots the half width at half maximum (HWHM) at each temperature extracted by fitting a Frota function (red dashed lines) and corrected for the thermal broadening of the tip. The plot includes the fit to the empirical Fermi liquid model expression. (h) Magnetic field dependence of the Kondo resonance with the field strength indicated in the figure, measured at $T = 1.3$ K. The red dashed lines show the simulated curves using a model for a $S = 1$ system. The inset shows the dependence of Zeeman splitting of the Kondo resonance with magnetic fields, determined from the bias position of steepest slope (indicated on the spectrum at 2.8 T). The dashed line fits the Zeeman splitting with a g factor of $1.98 \pm 0.07$. (i) Stacked conductance spectra as a function of the lifting height (as measured with respect to the contact point) of a 22 unit cell long 5-AGNR on top a NaCl decoupling layer on Au(111). (a)–(c) Reproduced from [102]. CC BY 4.0. (d)–(f) Reproduced from [52]. CC BY 4.0. (g), (h) Reprinted figure with permission from [100], Copyright (2020) by the American Physical Society. (i) Reprinted with permission from [104]. Copyright (2020) American Chemical Society.

However, an unambiguous discrimination of the Kondo origin normally requires differentiating it from other possible sources of zero-bias features like tip-effects or low-energy inelastic excitations [106]. There are multiple ways to do so. In scanning probe spectroscopy experiments, this is most commonly performed analyzing the temperature-dependent width of the resonance [100, 108], which displays an anomalous broadening at a much faster pace than expected from a conventional thermal broadening, as shown, e.g. in figure 9(g) with measurements obtained on extended triangulene molecules [100]. Furthermore, the width and its temperature dependence determine the radical's Kondo temperature, which is in turn like a measure for the interaction of the magnetic impurity with the supporting substrate and its electron reservoir [106]. Alternatively, the same information can also be extracted from the temperature-dependent resonance intensity [109].

Proof for the magnetic origin of the zero-bias resonance can also be obtained analyzing its response to a magnetic field, which causes a Zeeman splitting of the resonance that becomes observable at sufficiently strong fields that depend on its width or Kondo temperature [100, 101]. An example thereof is shown in figure 9(h), corresponding to the field-dependent conductance spectra on the same extended triangulene molecules as the temperature-dependent data of figure 9(g) [100].

Another approach is ramping the associated state's energy, which can in turn modify its occupation. This approach is often utilized in devices [110, 111] but not so often in SPM because in its most obvious application mode it requires a gateable system [112]. However, a similar 'gating' effect can be obtained, e.g. when gradually lifting a molecule with the scanning probe. The fading electrostatic influence of the substrate causes the molecular states to gradually realign. This can be seen for example in figure 9(i), which displays conductance spectra while lifting a 5-atom wide AGNR (5-AGNR) [104]. These ribbons feature magnetic end states that, when adsorbed on a Au(111) surface, become unoccupied due to charge transfer to such high work-function substrate. However, while lifting the ribbon from one of its ends, the associated end state realigns, approaching the Fermi level and becoming singly occupied again. From that moment on, the Kondo resonance appears in the conductance spectra [104]. Other transport phenomena with partially lifted GNRs have also been reported [52, 70, 113–116].

A different type of signal that has been also used to demonstrate the magnetism of carbon nanostructures by SPM and spectroscopy is the presence of inelastic spin-flip excitations. A beautiful example thereof is shown again in figures 9(d)–(f) with the GNR junctions [52]. By a controlled tip-induced dehydrogenation of the passivated carbon site, a second radical can be recovered. The proximity of the two radicals, along with the respective extension of the associated spin-densities, allows for a notable exchange interaction between the two spins. The ground state is a singlet, but the tunneling electrons can excite the electrons into a triplet configuration with ferromagnetically aligned spins, which appears as clear steps in the conductance spectra at $V \approx \pm 10$ mV that corresponds to the excitation energy. The steps therefore not only prove the presence of spins within the carbon nanostructure, but additionally provide information on their exchange interactions.

## 5. Origin of magnetism in carbon-based materials

### 5.1. Sublattice imbalance

As already explained above in section 3.1, molecules formed by alternant structures but with a different number of atoms in each sublattice, $N_A$ and $N_B$, display a net spin of magnitude $S = |N_A - N_B|/2$ [75]. An intuitive example thereof, shown earlier in figure 6, are defects in graphene in which certain $p_z$ electrons are removed from the network either by creating C vacancies [20] or by $sp^3$ rehybridization upon hydrogenation [78]. However, there is also a large variety of finite molecular structures that display sublattice imbalance. Some iconic examples are triangular molecules with their sides made up by zigzag edges (figure 10), so called [$n$]-triangulenes, where $n$ is the number of hexagons along each molecular edge. In particular, the cases with $n = 2$ and $n = 3$ are also called phenalenyl and triangulene, respectively. The latter is pictured in figure 10(a). Whereas 12 of its atoms belong to sublattice A, only 10 atoms belong to sublattice B, which according to Lieb's theorem [75] implies a net spin $S = 1$. On the other hand, the largest number of atoms that are not nearest neighbors to each other is 12, coinciding with the atoms of sublattice A. Given that the total number of atoms is 22, the nullity $\eta$ amounts to 2. That is, the counting rules predict for triangulene two $\pi$-radicals and $S = 1$, implying a ferromagnetic alignment of the two radical states. Indeed, it can be immediately realized that no Kekulé structure can be drawn for triangulene. Although different resonance structures may be drawn, all of them require the addition of two $\pi$-radicals, which furthermore are located in the same sublattice. It is energetically most favorable for spins in adjacent sites to be antiferromagnetically coupled, so as to allow for bonding interactions between them [83]. In bipartite lattices this generic assumption causes atoms on the same lattice to share the same spin, while being antiferromagnetically aligned to atoms of the opposite sublattice. The presence of two radicals located on atoms of the same sublattice is thus in perfect agreement with Lieb's theorem and the nullity parameter.

Although triangulene was already hypothesized by Clar and Stewart in 1953 [21], its synthesis by conventional chemistry has only been achieved recently, and only with the help of bulky edge substituents to sterically protect the radical sites at its zigzag edges [119, 120]. Instead, OSS under UHV conditions allowed its first synthesis without further substituents in 2017 (figure 10(a)) [22]. Its magnetism was indirectly confirmed by the characterization of its singly occupied molecular orbitals. Soon after, larger members of the triangulene family have been synthesized and characterized under vacuum as well, as is the case of [4]-triangulene (figure 10(b)) [117], [5]-triangulene (figure 10(c)) [118], [7]-triangulene with [121] and without [122] a well-defined hole in its center, or other extended triangulene derivatives [100]. As the size is increased, also the nullity and the sublattice imbalance become greater (figures 10(b) and (c)), which

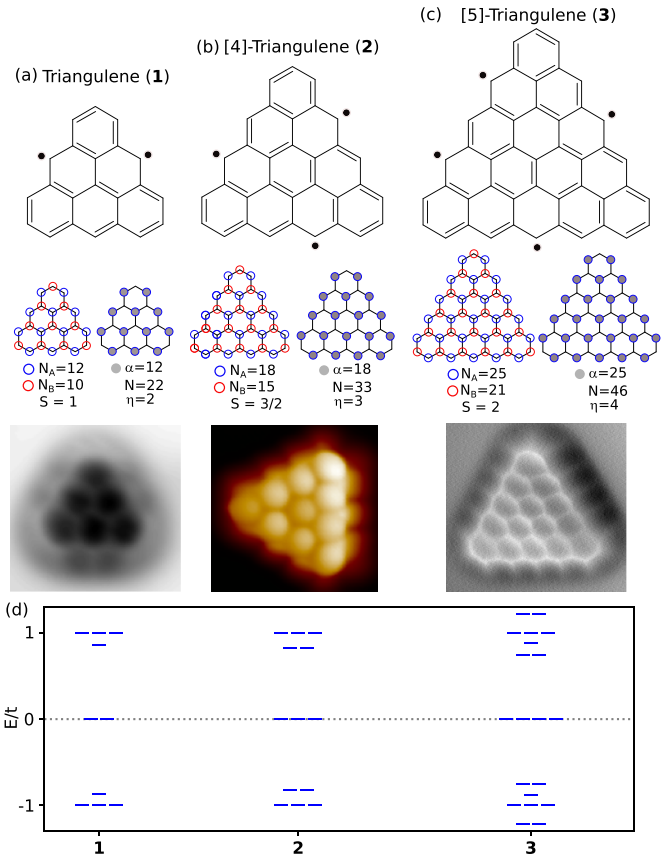


**Figure 10.** Molecular structure, atoms belonging to each sublattice marked in blue ($N_A$) and red ($N_B$), atoms making for the largest number of non-adjacent sites marked in grey ($\alpha$), and the bond-resolving SPM images of the associated structures for (a) triangulene, (b) [4]-triangulene, (c) [5]-triangulene, (d) Calculated low-energy spectrum for each of the structures within a TB model with nearest neighbor hopping $t$. (a) Reproduced from [22], with permission from Springer Nature. (b) Reprinted with permission from [117]. Copyright (2019) American Chemical Society. (c) Reproduced with permission from [118]. 

translates into high-spin molecules whose magnetic properties have been further confirmed with calculations and experiments [100, 117, 118, 121, 122]. By way of example, the calculated low-energy spectrum for triangulene, [4]-triangulene and [5]-triangulene are displayed in figure 10(d), confirming the increasing number of zero-energy states in each for the structures from two to three and four, which correspond also to the number of radicals on the molecule. Indeed, that is exactly the number of radicals that need to be drawn on the resonance forms to satisfy the valence four of its carbon atoms.

Further examples with sublattice imbalance are, e.g. heptauthrene, in which $N_A - N_B = 2$ and the net spin is therefore $S = 1$ [123], or rhombus-shaped molecules whose symmetry is broken by a missing C atom, causing a sublattice imbalance of 1 and thus $S = 1/2$ [124]. As explained above for the graphene case, the hydrogenation of finite molecules can equally cause a rehybridization of C atoms from $sp^2$ to $sp^3$, which in terms of the $p_z$ electron counting rules is equivalent to the removal of that atomic site. Therefore, under a SPM, a controlled tip-induced dehydrogenation of $sp^3$ hybridized C atoms can be used to effectively add $p_z$ orbitals and thereby change the magnetic properties of the molecules in a controlled manner [24, 52, 100, 123]. An example thereof was already shown in figures 9(d)–(f), in which doubly hydrogenated edge atoms in GNR junctions were dehydrogenated, creating additional radical states whose interaction with already present radicals could be assessed from inelastic spin-flip excitations in STS measurements [52]. The graphene $sp^2$-to-$sp^3$ rehybridization by hydrogen or other adsorbates/defects, and their implications for $\pi$-magnetism, has been studied extensively by calculations [12, 48, 49, 77, 125–130].

### 5.2. *Topological frustration*

By topological frustration it is meant that there is no possible way to draw a Kekulé structure for the molecules. All the molecular structures discussed in the previous section displaying sublattice imbalance suffer topological frustration. Chemical structure drawings require the addition of explicit radicals to satisfy the valence four of carbon atoms. This is easily understood with the qualitative arguments outlined in the description of the counting rules for bipartite lattices as in nanographenes. Each carbon atom has one $p_z$ electron that can only bind to electrons of the opposite sublattice. It automatically follows that, if the two sublattices have a different number of atoms, the electrons will not be able to bind pairwise, leaving some unpaired electron as a radical. A similar scenario can also apply to non-benzenoid structures in which the sublattices are no longer well-defined. By way of example, the presence of odd-membered rings may result in structures with an odd number of $p_z$ electrons, which automatically prevents their pairwise coupling. An example thereof can be found in structure **6** of figure 1. However, topological frustration can also occur for benzenoid carbon nanostructures displaying sublattice balance, which were formerly termed as 'concealed non-Kekuléan' structures [131]. The smallest of such structures (as counted by the number of comprised hexagons) consist of eleven hexagons, which can be arranged in eight different configurations that display topological frustration (see structures I–VIII in figure 11(a)). The number of possible 'concealed non-Kekuléan structures' rapidly grows with increasing molecular size [131].

As illustrated in figures 11(b) and (c) with structures II and VIII (as well as with the Clar's goblet I in figure 7), each of the 'concealed non-Kekuléan structures' in figure 11 displays sublattice balance and therefore singlet character according to Lieb's theorem. However, all of them display $\eta = 2$, as confirmed also with the TB calculations displayed in figure 11(d), which reveal two zero-energy states for each of the structures. This can be reconciled with the singlet character by an antiferromagnetic orientation of the two radicals' spins. The antiferromagnetic alignment can also be also expected from the location of the radicals, which may be drawn in the chemical structures at various positions, but with the constraint of having always one on each sublattice (figures 11(b) and (c)). Structures that display sublattice balance and topological frustration at the same time and that have been synthesized and

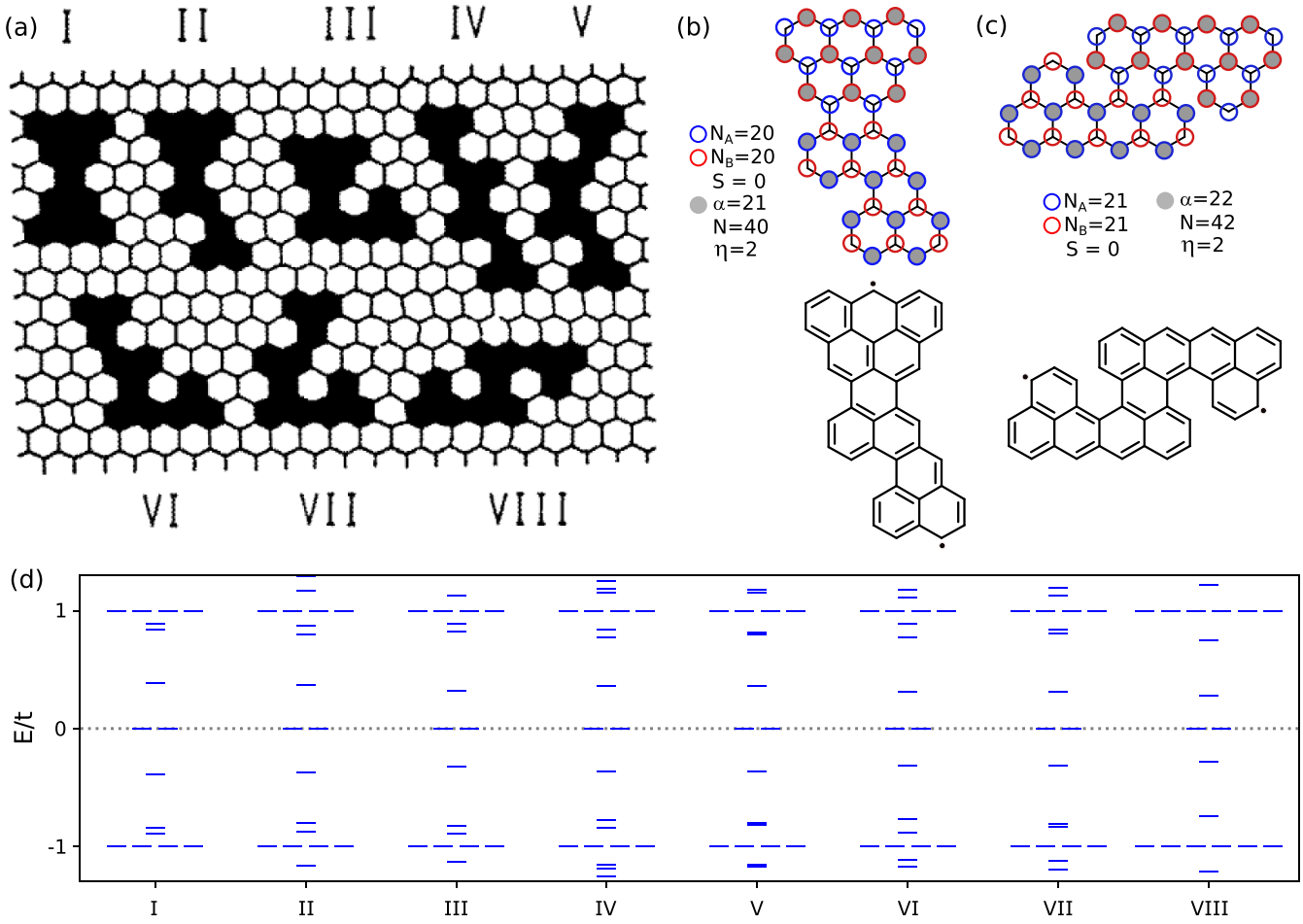


**Figure 11.** (a) The eight smallest structures comprising eleven hexagons that display topological frustration in spite of their sublattice balance. (b) Chemical structure and marked atoms belonging to each sublattice as marked by blue and red circles, respectively, as well as the atoms making for the largest number of non-adjacent sites (filled in grey) for structure II. (c) Same for structure VIII. (d) Calculated low-energy spectrum within a TB model with nearest neighbor hopping $t$ for structures I–VIII. (a) Reproduced from [131], with permission from Springer Nature.

**Table 1.** Examples of structure classification.

| | Kekulé | non-Kekulé |
|---|---|---|
| Sublattice balance ($N_A = N_B$) | ZGNRs, chiral GNRs [132], rhombenes [133] ($S = 0$) | Clar's goblet [24] (figure 11) ($S = 0$) |
| Sublattice imbalance ($N_A \neq N_B$) | *None* | Triangulene family (figures 10(a)–(d)), Extended triangulene (ETRI) [100] (figures 21(a)–(c)) ($S > 0$) |
| Mechanism | Coulomb repulsion vs. hybridization gap | Topological frustration (zero-energy states) |

characterized experimentally are for example the Clar's goblet shown in figure 7 [24] (structure I in figure 11(a)) or triangulene dimers linked at their vertices [42].

### 5.3. *Polarization of low-energy states*

The carbon-based nanostructures discussed in previous sections (see also table 1) with sublattice imbalance and topological frustration all feature zero-energy states (as predicted by the nullity parameter $\eta$), for which any repulsive Coulomb interaction triggers a spin-polarization that reduces the density of states around the Fermi level and thereby avoids the associated instability. However, the same scenario can happen also with molecular states that are not strictly at zero energy ($\eta = 0$), requiring a larger Coulomb repulsion the farther the orbitals are from the Fermi level. At this point it is worth remarking that the Coulomb repulsion discussed in this context is not the on-site Coulomb repulsion included in the Hubbard-model, but the effective Coulomb repulsion felt by an electron upon double population of a molecular orbital. The latter is proportional to the former, but depends on additional parameters like the molecular state's extension. That is, a

more extended $\pi$-radical state will normally display a lower Coulomb repulsion than a more localized one [103]. In turn, the extension of the radical state depends on its hybridization with the following fully occupied (unoccupied) low-energy electronic states [134]. The lower the carbon nanostructure's electronic band gap, the closer the HOMO and LUMO will be to the in-gap radical states, promoting their hybridization and thereby the radical's delocalization [69, 135].

In a simplified two-electron picture, the polarization of low-energy states takes place when the Coulomb energy of putting a second electron into one orbital is larger than the energy cost of creating two spatially separated radical states (with reduced Coulomb repulsion) that can be understood as a linear combination of the frontier occupied and unoccupied states (figure 5) [13, 136–138]. A similar argumentation also holds for more extended systems with more electrons, as for example the case of ZGNRs, for which one-third of its valence band forms a nearly zero-energy flat band that consequently undergoes spin polarization and forms the so-called GNR edge-states [3, 25, 45, 54, 139, 140].

There are multiple ways to qualitatively understand the behavior of molecular nanostructures undergoing (or not) such spin polarization, which often shows a notable size-dependence with relatively well-defined thresholds. Although with some exceptions [141, 142], in conjugated materials the band gap typically shrinks with increasing size [143]. Recalling that the closer the electronic states are to the Fermi level, the lower the Coulomb repulsion is needed to favor the formation of spatially separated spin-polarized states [3], larger structures with lower band gaps will thus facilitate the spin-polarization.

A complementary explanation to the size-dependent spin-polarization is that two singly occupied radical states hybridize into a fully occupied HOMO and a fully unoccupied LUMO as they are brought sufficiently close to one another in carbon nanostructures below a certain size threshold. Such threshold is again dependent on the radical's delocalization described above, and thus strongly dependent on the particular bonding structure. By way of example, finite GNRs with longitudinal armchair-shaped edges and five carbon atoms across their width are open-shell structures with radical states at their zigzag ends [104]. However, as the ribbon's length drops to 14 unit cells or less (which basically comprise 28 rows or less of zigzag C atoms from end to end), the two end-states hybridize, conferring the ribbon a predominantly closed-shell character [104]. For comparison we now focus on differently shaped GNRs, namely chiral (3, 1) ribbons, whose longitudinal edges are formed by a regular alternation of three zigzag and one armchair unit [144, 145]. This type of ribbons hosts spin-polarized edge-states. However, as their width drops to 4 or less rows of zigzag C atom from side to side, the edge-states hybridize and result in a conventional closed-shell semiconducting structure [146, 147].

*5.3.1. Chemical counting rules to predict spin polarization of low-energy states.* The perhaps most intuitive way to qualitatively understand the spin polarization of low-energy states is based on chemical counting rules. As already explained in section 3.3, the stabilization energy of three new Clar sextets approximately compensates the energetic cost of forming a pair of radicals by breaking a $\pi$-bond. Thus, as we will see with a number of examples, if three or more sextets can be formed for each new pair of radicals, this will normally be favorable, marking an approximate threshold at which polarization of low-energy states sets in. The larger are the molecular structures, the more possibilities there are to generate a sufficient number of Clar sextets, supporting again the stronger tendency of larger molecules to produce radicals by polarization of low-energy states.

In a first example, we analyze the number of Clar sextets (four) in the Clar formula of a molecule consisting of two fused triangulene moieties (figure 12(a)). As shown in figure 12(b), the number of Clar sextets can be increased from four to five if two $\pi$-radicals are included into the structure. This molecule has been synthesized under vacuum supported on an Au(111) surface (figure 12(c)) and its characterization revealed a closed-shell ground state, as expected from the sub-threshold amount of new Clar sextets per pair of radicals [100] On the same substrate, a similar molecular structure with an extended molecular backbone as shown in figures 12(d)–(f) has also been studied [108]. Figure 12(d) shows its Clar formula, characterized by six Clar sextets. A non-Kekuléan structure including two radicals increases the number of sextets to nine (figure 12(e)). That is, this larger molecule reaches the threshold of three additional sextets per pair of radicals and is thus expected to undergo spin polarization. Its detailed analysis indeed confirmed the open-shell nature of its ground state, as can be readily inferred indirectly from the STM image in figure 12(f) that shows the characteristically enhanced contrast associated with low-energy states around the two molecular ends superposed to the resolved molecular backbone structure [108].

In the following we describe another example of more extended structures, namely chiral GNRs of varying width. Chiral GNRs display an alternating number of zigzag and armchair segments. They are predicted to be open-shell structures with so-called edge states consisting of $\pi$-radicals [148]. There is, however, a threshold width below which the ribbons become conventional closed-shell structures [79, 132, 146, 149]. This threshold width depends on the chirality, being lower the closer the ribbon's edge orientation is to a pure zigzag direction [79, 146, 149]. The chirality dependence can also be explained with Clar sextet counting rules, but in the following we will focus on the width dependence for a fixed chirality. In particular, we focus on (3, 1)-chiral GNRs, which is the only type of atomically precise chiral GNRs that have been synthesized to date with varying width [132, 144, 145]. These ribbons have three zigzag units per unit cell, followed by an armchair segment. Calculations on ribbons with four zigzag lines across the width of its unit cell predict no magnetization, whereas increasing the unit cell width by only two zigzag lines more already results in an open shell-structure with magnetic edge states [132, 146]. For the narrow ribbons, the Clar formula displays two sextets per unit cell (figure 12(g)), which can be increased to four upon creation of a pair of radicals

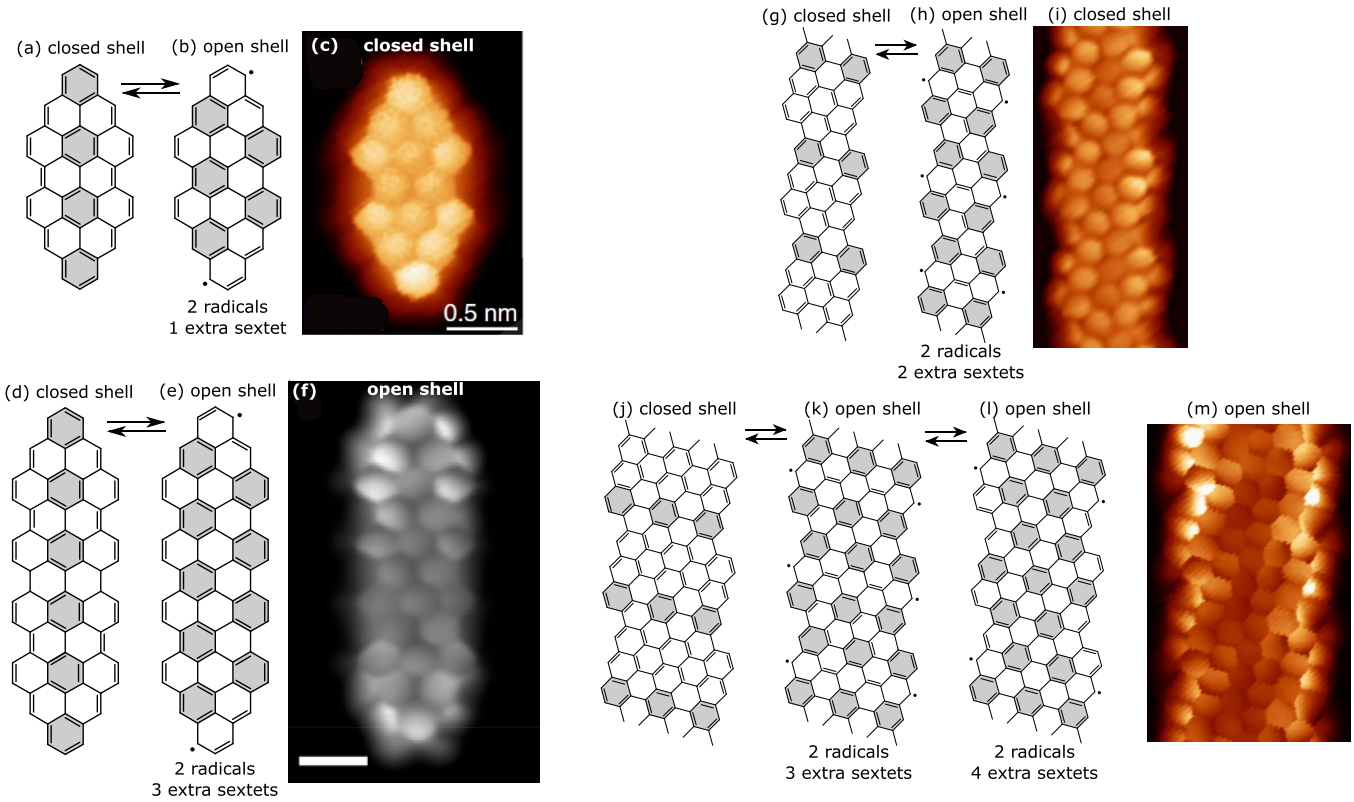


**Figure 12.** Closed-shell (a) and open-shell (b) chemical structure drawings for a triangulene dimer, along with an experimental bond-resolving STM image of the structure on Au(111) (c). Closed-shell (d) and open-shell (e) chemical structure drawings for an isomorphic structure with an extended carbon backbone in the central part, along with an experimental bond-resolving STM image of the structure on Au(111) (f). Closed-shell (g) and open-shell (h) chemical structure drawings for (3, 1) chiral GNRs with four zigzag lines across the width of their unit cell, along with an experimental bond-resolving STM image of the structure on Au(111) (i). Closed-shell (j), open-shell (k) and another open-shell structure with a larger supercell (l) for (3, 1) chiral GNRs with six zigzag lines across the width of their unit cell, along with an experimental bond-resolving STM image of the structure on Au(111) (m). For each chemical structure, the Clar sextets are highlighted in grey. (c) Reprinted figure with permission from [100], Copyright (2020) by the American Physical Society. (f) Reprinted with permission from [108]. Copyright (2020) American Chemical Society. (i), (m) Reproduced from [132]. CC BY 4.0.

(figure 12(h)). In line with the calculations, this is below the proposed threshold and these ribbons are thus not expected to present magnetic edge states. The synthesis and characterization of this type of ribbons (figure 12(i)) has indeed proved the absence of edge states, interpreted as a rehybridization of the edge states from either side with one another as they are brought excessively close [147]. For the wider ribbons, the Clar formula displays three sextets per unit cell (figure 12(j)), which can be increased to six (three extra sextets) in an open shell structure with two radicals per unit cell (figure 12(k)). In fact, considering the extended nature of the ribbons that allows creating larger supercells, the ratio of newly created sextets per radical pair can be increased up to four (figure 12(l)). In any case it is beyond the proposed threshold and is thus expected to favor the open-shell structure, in agreement with the theoretical predictions [146]. Ribbons of this width have also been synthesized and characterized (figure 12(m)) [132]. The results confirm the presence of the edge states, as may already be inferred from the obvious density of states around the Fermi level that provides the characteristic enhanced contrast at the GNR edges in the bond-resolving STM images at low bias (figure 12(m)) [132].

The same threshold also explains the transition from closed-shell to open-shell in other molecules as a function of their size, like in the case of periacenes [61, 150, 151]. A non-Kekuléan structure with two additional radicals allows for the creation of two extra Clar sextets in the case of bisanthene. This is sub-threshold and bisanthene is therefore expected to show a predominantly closed-shell character. However, as the periacene's size is increased, e.g. to peripentacene or periheptacene, the non-Kekuléan structure with two radicals already allows for the creation of three extra Clar sextets, whereby the threshold is reached and an open-shell structure becomes in principle favorable. SPM experiments on those structures have indeed confirmed the open shell character of peripentacene and periheptacene and the closed-shell character of bisanthene [61, 150]. Similar conclusions and the same threshold can be extracted comparing, e.g. rhombene molecules of different sizes [133].

*5.3.2. Alternative factors influencing the counting rule thresholds.* It should be kept in mind, however, that these counting rules are only a guidance and not at all

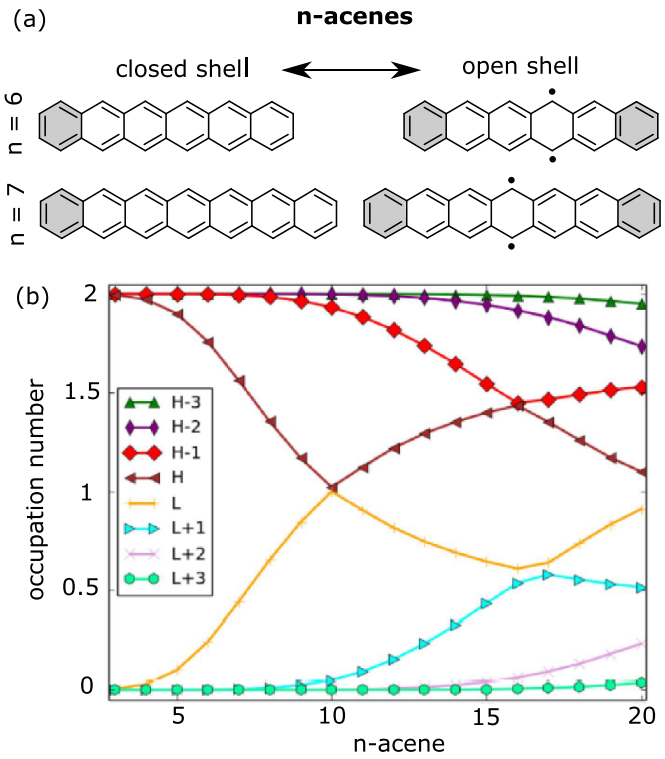


**Figure 13.** (a) Closed-shell and open-shell structure drawings for two acenes, namely hexacene and heptacene. (b) Active orbital occupation numbers of the low-energy orbitals for the lowest singlet states of n-acenes as a function of the acene length n, as calculated with DFT. (b) Reproduced from [137]. CC BY 4.0.

rigorous. Additional factors may affect the energies of open- and closed-shell structures and thereby shift the proposed threshold value of three Clar sextets per radical pair.

An example thereof are acenes, which consist of linearly fused six-membered rings. A characteristic of this family of molecules is that they only display one single Clar sextet independently of their size (figure 13(a)). The Clar sextet can furthermore migrate freely to any of the six-membered rings, diluting even more the effect of the sextet's aromatic stabilization. Indeed, calculations reveal that the homodesmic stabilization energy per $\pi$-electron scales inversely with the acene size [86]. All this endows the acenes with a particularly low-energy gap as compared to similarly sized molecules of different topologies [152, 153]. As a result, above a certain size threshold that is typically assumed to be around hexacene [58, 154], the molecules develop an increasing open-shell character that can be understood as a growing occupation of the LUMO orbital at the expense of the HOMO occupation (figure 13(b)) [58, 137] since the radical states actually correspond to linear combinations of the occupied and unoccupied molecular orbitals [13, 138]. An occupation of HOMO and LUMO, each by one electron, would correspond to a full diradical, whereas the gradual occupancy of higher orbitals (e.g. LUMO+1) at the expense of lower lying orbitals (e.g. HOMO–1) marks the onset of polyradical character, as has been predicted to occur for longer acenes (figure 13(b)). Indeed, as a 'rule-of-thumb' one can roughly associate an initiating radical pair generation with every six rings [58]. This is also the reason for the strongly compromised stability for higher acenes with six or more rings [152, 155], which correlates well with the acene size at which a certain diradical character starts to set in. For the same reason, it is only recently that higher acenes are being successfully synthesized [152]. Whereas acenes as large as undecacene have been synthesized under cryogenic matrix isolation conditions [156], the largest acene that has been synthesized to date is dodecacene [142], obtained by OSS under ultra-high-vacuum conditions.

In any case, as can be seen in figure 13(a), acenes are a rare case in which the open-shell character sets in in spite of gaining only one Clar sextet for each pair of radicals created. The radicals are largely delocalized over all the rings spanned between the sextets, which lowers their energy and thereby justifies the anomalous threshold at which acenes become open-shell. In addition, as mentioned above, it also relates to the continuously decreasing ratio of Clar sextets (fixed to one) per carbon atom as the acenes grow longer, rendering the acenes less and less stable with increasing size. For ratios beyond a lower limit of one Clar sextet for approximately 26 atoms (those forming the 'threshold' value of six rings) the stabilization energy becomes too low and the generation of an additional Clar sextet becomes favorable, along with the appearance of two radicals.

Alternative factors that also lower the threshold of new Clar sextets per radical pair are topological defects, as will be discussed in section 5.4.

*5.3.3. Associating spin-polarization to competing aromatic-quinoid conjugation patterns.* Many of the cases undergoing spin-polarization of low-energy states can be understood from the point of view of a competition between aromaticity and $\pi$-electron delocalization, the latter being typically promoted by quinoid conjugation patterns [157]. In fact this applies to carbon-based materials beyond pure hydrocarbons and hexagonal patterns, as for example shown in figure 14 with polythiophene. The change between aromatic and quinoid structures brings about a reversal of HOMO and LUMO levels (figure 14(a)) [158]. This reversal implies changes in its properties, particularly notable when such structures are made finite. An example thereof is shown in the following with tetracyanoquaterthiophenequinodimethane [134]. Its closed-shell structure is displayed in figure 14(b), characterized by its quinoid conjugation pattern. As the thiophene units change to their aromatic form, two radicals are concomitantly generated at its ends (figure 14(d)). The generation of $\pi$-radicals implies an energetic cost that may be lowered by their hybridization with the electrons of the following doubly occupied orbitals (HOMO′ in figures 14(c)–(e)) [134]. The lowered energy of such hybridized radicals facilitates its compensation by the aromatic stabilization, which may promote the diradical character of the molecule. Several properties of the radicals can be explained by this hybridization scenario.

One is the usual antiferromagnetic alignment of the $\pi$-radicals in symmetric and linear molecules of this kind, which renders their ground state a singlet. Under these conditions, the

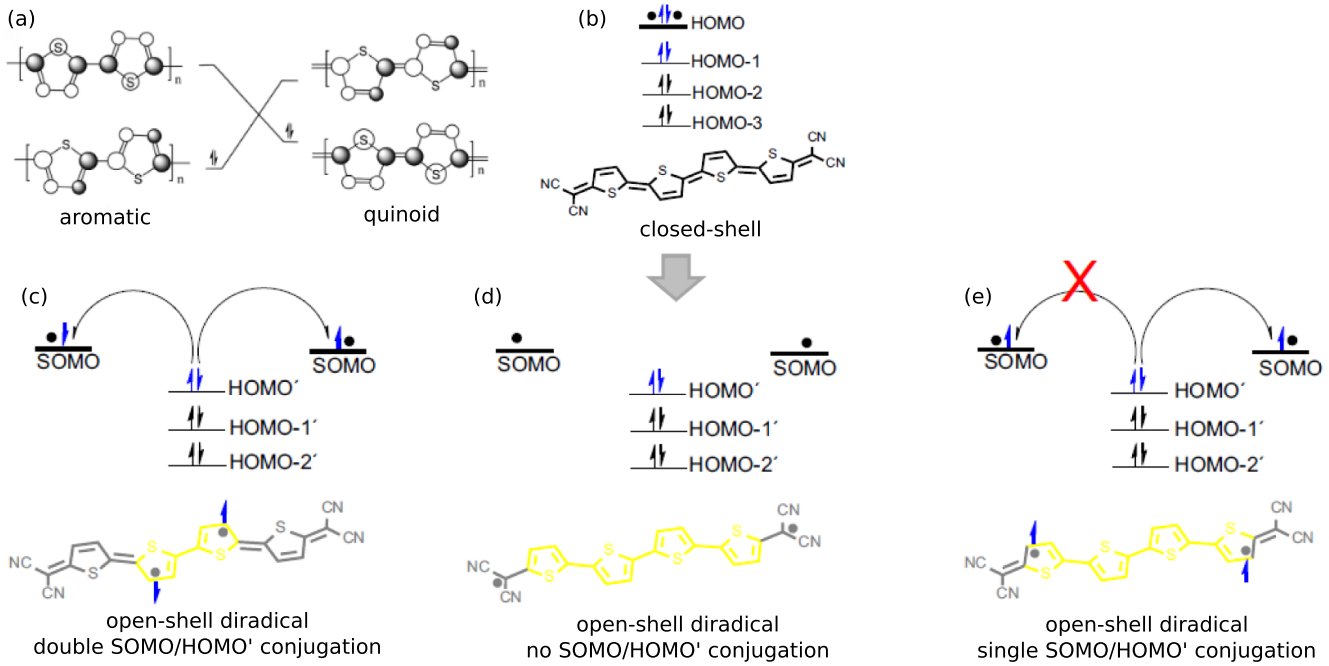


**Figure 14.** (a) Calculated wave functions at the onset of valence and conduction band for polythiophene in its aromatic and quinoid forms. Molecular structure drawings and associated orbitals with spin-up and spin-down electrons in closed-shell quinoid tetracyanoquaterthiophenequinodimethane (b), in its open-shell diradical configuration with no SOMO/HOMO′ hybridization (d), in its open-shell singlet configuration with double SOMO/HOMO′ hybridization (c) and in its open-shell triplet configuration with single SOMO/HOMO′ hybridization. Note the differentiation between the SOMO/HOMO′ orbitals, which do not correspond to each other. In fact, HOMO′ in the open-shell relates to the HOMO–1 in the closed-shell configuration. (a) Reproduced from [158] with permission from the Royal Society of Chemistry. (b)–(e) Reproduced from [134], with permission from Springer Nature.

'spin-up' electron of the HOMO′ can hybridize with the 'spin-down' singly-occupied molecular orbital (SOMO) electron and vice versa (figure 14(c)), contributing to the delocalization and stabilization of the radicals. Instead, if the two radicals align ferromagnetically into a triplet, only one of the ′ electrons (spin-down) can hybridize with one of the two spin-up radicals, whereas the hybridization of the second (spin-up) HOMO′ electron with the SOMO electrons is hindered by the Pauli exclusion principle (figure 14(e)) [134]. The double hybridization/stabilization of the singlet in comparison to the single hybridization/stabilization of the triplet cause the former to be often energetically favored and thus commonly the ground state in linear diradical molecules.

Another characteristic property of the radical states, namely their spatial distribution, can also be related to the hybridization picture. The hybridization of the radical states with the extended doubly occupied orbitals allows for their increased delocalization. Given that the hybridization increases the closer the in-gap radical states are to the following doubly occupied orbitals, the radical delocalization scales inversely with the molecular band gaps [69, 135]. As can be easily discerned from the wireframe chemical structure drawings (figure 14), the radical states appear at the ends of the aromatic structure independently of whether this coincides with the molecular ends or with the junction to a quinoid section. The delocalization of the radical states away from the edges thus implies a change of conjugation back to the quinoidal form near the molecular ends (figure 14(c)). Eventually, this may result in a maximum radical density displaced away from the molecular ends, an effect that has indeed been characterized [69] and directly observed in real space by SPM on different diradical molecular structures [69, 104].

*5.3.4. Analysis from a topology viewpoint.* As explained in section 2.6, a useful alternative way to understand and predict the presence of radical states in certain molecular structures is topology. From the symmetries of the filled bands of infinite systems, or from the calculated Zak phase, the materials are classified as trivial or nontrivial. For the latter, zero energy modes appear at the structure's ends as they are made finite.

The simplest organic conjugated chain for which to calculate this is polyacetylene, which has only two $p_z$ electrons per unit cell and thus only one filled $\pi$-band. It can be easily modeled with TB by a linear array of electronic states coupled with alternating hopping constants $t_n$ and $t_m$ (figure 15(a)) in what is called the Su–Schrieffer–Heeger (SSH) model [159] The solutions to the Hamiltonian are given by:

$$E_{\pm}(k) = \pm\sqrt{t_n^2 + t_m^2 + 2t_n t_m \cos(k)}, \tag{19}$$

and the associated bands are plotted in figure 15(a) for a variety of values of $\delta = t_n - t_m$, showing how the band width increases and the band gap shrinks with a decreasing $\delta$ parameter, eventually becoming metallic for $\delta = 0$. Double bonds display a larger hopping constant than single bonds, which in

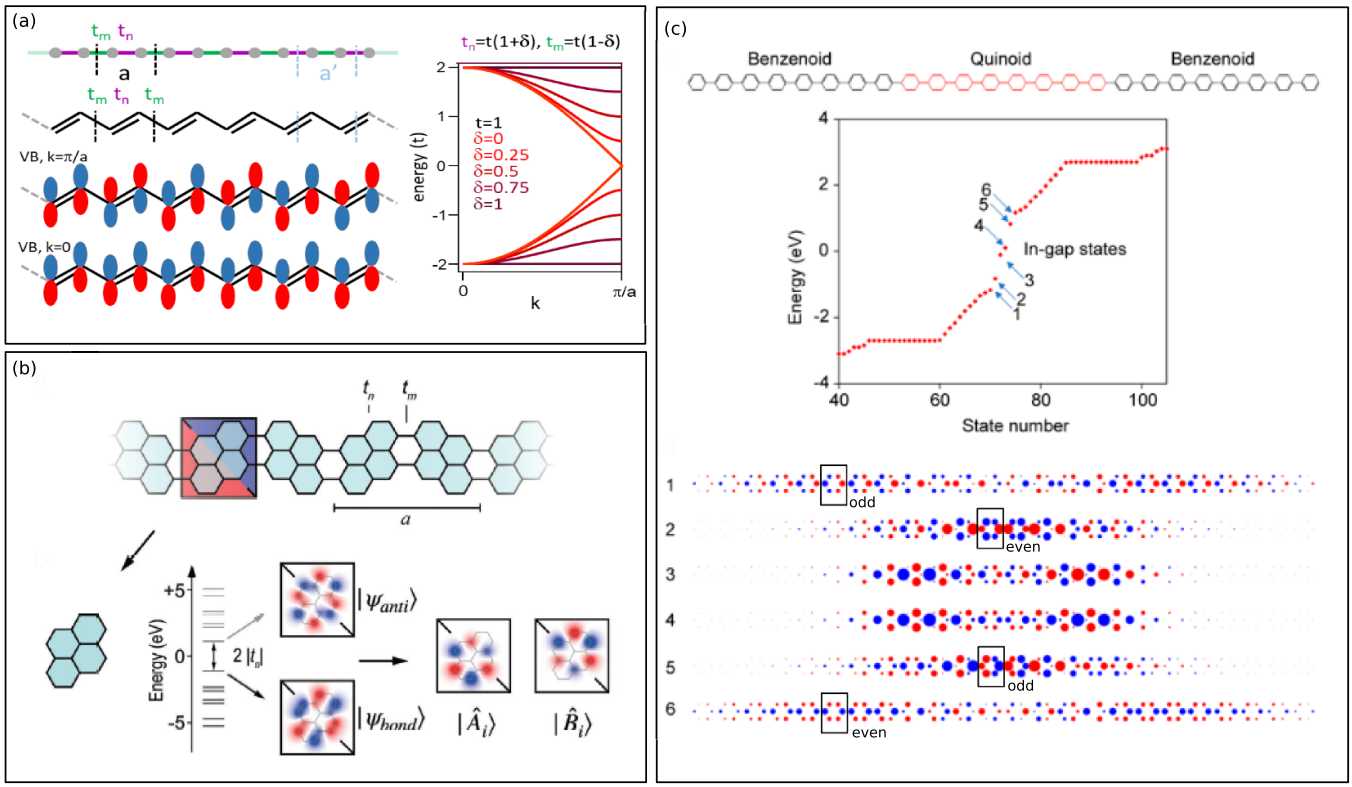


**Figure 15.** (a) Model of linear atoms with electrons coupled by alternating hopping constants $t_n$ and $t_m$ and two possible unit cell choices $a$ and $a'$. Below is the chemical structure of polyacetylene, formed by carbon atoms with one $p_z$ electron each and alternating single and double bonds, that can be represented by this model. The calculated band structure is shown on the right for varying $t_n$ and $t_m$ values, and the wave functions of the valence band at the Γ point and at the zone boundary are shown at the bottom. (b) Carbon backbone of a GNR formed by pyrene units and the modeling of its low-energy bands with the SSH model. The calculated HOMO and LUMO levels are represented as the bonding and antibonding combinations of the two orbitals that conform the SSH chain. The intra-unit cell hopping constant $t_n$ corresponds to half of the unit cell's HOMO–LUMO gap, whereas the inter-unit cell hopping constant depends on the inter-pyrene coupling motif and is obtained from fitting the SSH band-structure to that of the actual polymer. (c) Polyparaphenylene oligomer comprising benzenoid and aromatic sections, along with the energy spectrum for all of its electronic states. The six lowest energy states are labeled 1 to 6 and their calculated wave functions shown below. They can be assigned to the valence- and conduction-band onsets of the aromatic and quinoid sections (with accordingly reversed symmetries, as can be recognized from the marked unit cells in the boxes), plus two in-gap interface states. (b) [160] John Wiley & Sons. © 2020 WILEY-VCH Verlag GmbH & Co. KGaA, Weinheim. (c) Reprinted with permission from [161]. Copyright (2020) American Chemical Society.

our diagram implies that $t_n > t_m$ and $\delta > 0$. The wave functions are shown for the valence band states at the Γ point and at the Brillouin zone boundary (figure 15(a)). What remains to be determined is the unit cell, which is defined according to the finite chain's ends in such a way that the unit cell is commensurate with the chain's boundary conditions. If the chain ends with a double bond (that is, the chain is 'cut' through a single bond), the unit cell will be given by $a$, marked with dashed black lines. On the contrary, if the chain ends with single bonds (that is, the unit cell's ends and therefore the chain's ends 'cut' through double bonds), the unit cell will be given by $a'$, marked with bright blue dashed lines. Whereas for $a$ the larger hopping constant is intra-unit cell, it is inter-unit cell for $a'$.

Calculations of the Zak phase according to (14) provide the same result as that extracted from the parity of the Bloch wave functions according to (16). From figure 15(a), we can observe that the parity of the valence band (VB) at $k = 0$ is even (+1) regardless of the unit cell choice. However, at the zone boundary the parity of the VB states is even (+1) for $a$ but odd (−1) for $a'$. Consequently also the $\mathbb{Z}_2$ invariant changes from 0 (topologically trivial) for $a$ to +1 (topologically nontrivial) for $a'$. The topologically non-trivial character of $a'$ comes along with the appearance of radical states at the chain's ends. An intuitive picture of these state's origin is that the chain's ends 'cut' through what would have been a $\pi$-bond, leaving an unpaired electron behind.

The usefulness and simplicity of this SSH Hamiltonian is such that also other more complex polyaromatic structures have been mapped onto this model under the assumption that the HOMO and LUMO orbitals of the unit cell can be viewed as the bonding and antibonding dimer states of the SSH chain [69, 160]. This is exemplified in figure 15(b) with pyrene-based GNRs [160]. The topological class of the structures is then simply determined from comparing the resulting intra ($t_n$) and inter-unit cell ($t_m$) hopping constants. If the inter-unit cell hopping constant is larger, the structure is topologically non-trivial and will display end states.

In fact, those radicals appear at any topological interface. Vacuum can be considered as a topologically trivial material, and the ends of the chains discussed earlier represent an interface between a topologically non-trivial polyacetylene chain and vacuum. However, substituting the vacuum by another topologically trivial carbon-based material results in a similar radical state at the interface. For example, as discussed earlier, the change from aromatic to quinoid structures brings about a reversal of HOMO and LUMO levels (figure 14(a)). Such crossing is exactly what one expects when changing the topological class of a given material, as can be immediately concluded also from analyzing their respective symmetries. For the polythiophene pictured in figure 14(a) the HOMO or VB onset wave function is characterized by an odd parity, whereas it becomes even for the quinoid structure. Assuming that no other symmetry inversion occurs at the zone boundary or on other bands, this implies a change in the topological class and therefore the presence or absence of radical end-states (figure 14). In fact, figure 14(c) also shows how the radical states appear at the junction between aromatic and quinoid sections that come along with the hybridization of the end states with the fully occupied HOMO′-orbital.

Another instructive case is polyparaphenylene (PPP), which can also display aromatic and quinoid conjugation character, with the associated cross-over of valence and conduction band onsets. Figure 15(c) shows calculations of a finite PPP chain with a quinoid section embedded between two aromatic (benzenoid) regions, each of them 8 unit cells long [161]. The electronic states associated with this structure are calculated and the low-energy orbitals (labeled 1 to 6 in figure 15(c)) are analyzed. Aromatic structures normally display larger band gaps than their quinoid counterparts [161, 162]. It is therefore not surprising to see that the third occupied and unoccupied orbitals (labeled as 1 and 6) correspond to what can be seen as the valence and conduction band onsets of the aromatic segments (or rather the first confined state of the bands in these finite aromatic segments). The second occupied and unoccupied orbitals (labeled as 2 and 5) in turn correspond to the analogous valence and conduction band onsets of the quinoid segment. Looking at their respective wave functions and the associated longitudinal symmetry within the unit cells (marked with squares for the aromatic and quinoid segments separately), one can easily distinguish their reversal, confirming the different topological classes of either conjugation pattern. Most interestingly, two in-gap states appear (labeled 3 and 4) around the aromatic-quinoid junctions, although extending further into the quinoid segment that displays the lower band gap, exactly as expected from topological interface states. Samples resembling the calculated structure have been realized experimentally on Cu(111) surfaces and their characterization by SPM and STS has confirmed the presence of those in-gap states [161].

At this point it should be remarked that a topology analysis can be understood as if the bulk properties determine the properties at its edges or interfaces. Although it thus allows predicting the presence or absence of radical states in finite systems from calculations performed for infinite systems, it loses significance for systems of reduced dimensions. Nevertheless, many of the radical states studied in carbon-nanostructures can be understood from topological arguments, as are the end-states of different types of one-dimensional polymers [69], GNRs [66, 102, 104], interface states at GNR heterojunctions of varying width [68], or of varying backbones with, e.g. heteroatoms [70]. However, it is also worth reminding that such radical states can be equally well explained with alternative arguments, as are for example the conjugation patterns discussed in the previous section, or counting rules for 'locally uncompensated' lattice sites at the ends of long one-dimensional systems with two ends that are 'independent' from one another.

*5.3.5. Controlling the aromatic-quinoid balance and topological class.* The inspiring examples described above, along with many others, have motivated the rational design of molecular structures with premeditated conjugation patterns to obtain materials according to our needs. Controlling the topological class determines the presence (or absence) of magnetic topological interface or end-states, which may be even rationally coupled by a tailored distance between them. In addition, creating materials that carefully balance between their quinoid and aromatic structures typically have the lowest band gaps and also low reorganization energies, thereby promoting high charge mobilities [69, 160, 163]. Figure 16(a) shows an example thereof, in which the band gap of a variety of conjugated polymers is displayed as a function of their parametrized quinoid character [163]. The data display a characteristic V-shape whose zero band gap value roughly coincides with a balanced aromatic-quinoid structure. Interestingly, that balance (and therefore the polymer's band gap) can be controlled by an appropriate combination of more aromatic and more quinoid moieties. Figure 16(a) illustrates a sample case with two constituents whose polymeric form displays comparable band gaps but with quinoid (blue) or aromatic (green) character. Their combination in mixed polymers results in structures with a relatively balanced aromatic/quinoid structure and a greatly diminished band gap [163].

Closely related to this, a recent work demonstrated how the use of differently sized units within acene-based polymers linked by ethynyl bridges can be used to promote aromatic–ethynyl or cumulene–quinoid conjugation patterns (figure 16(b)), each belonging to a different topological class [69, 164]. The pentacene case is closest to the cross-over point and is therefore the polymer with lowest band gap, which amounts to only 0.35 eV as measured by STS on a Au(111) surface. Whereas the anthracene-based polymers are topologically trivial, the pentacene-based polymers display a topological nontrivial character, as predicted from calculations and confirmed experimentally with the absence and presence of topological end-states, respectively (see bottom part of figure 16(b) [69, 164]. For the latter, the low band gap promotes a significant hybridization of the end-states with the frontier orbitals, causing the end state's pronounced delocalization and a maximum intensity shifted away from the actual polymer's ends, as discussed earlier in section 5.3.3. The associated rehybridization into a predominantly ethynyl-aromatic

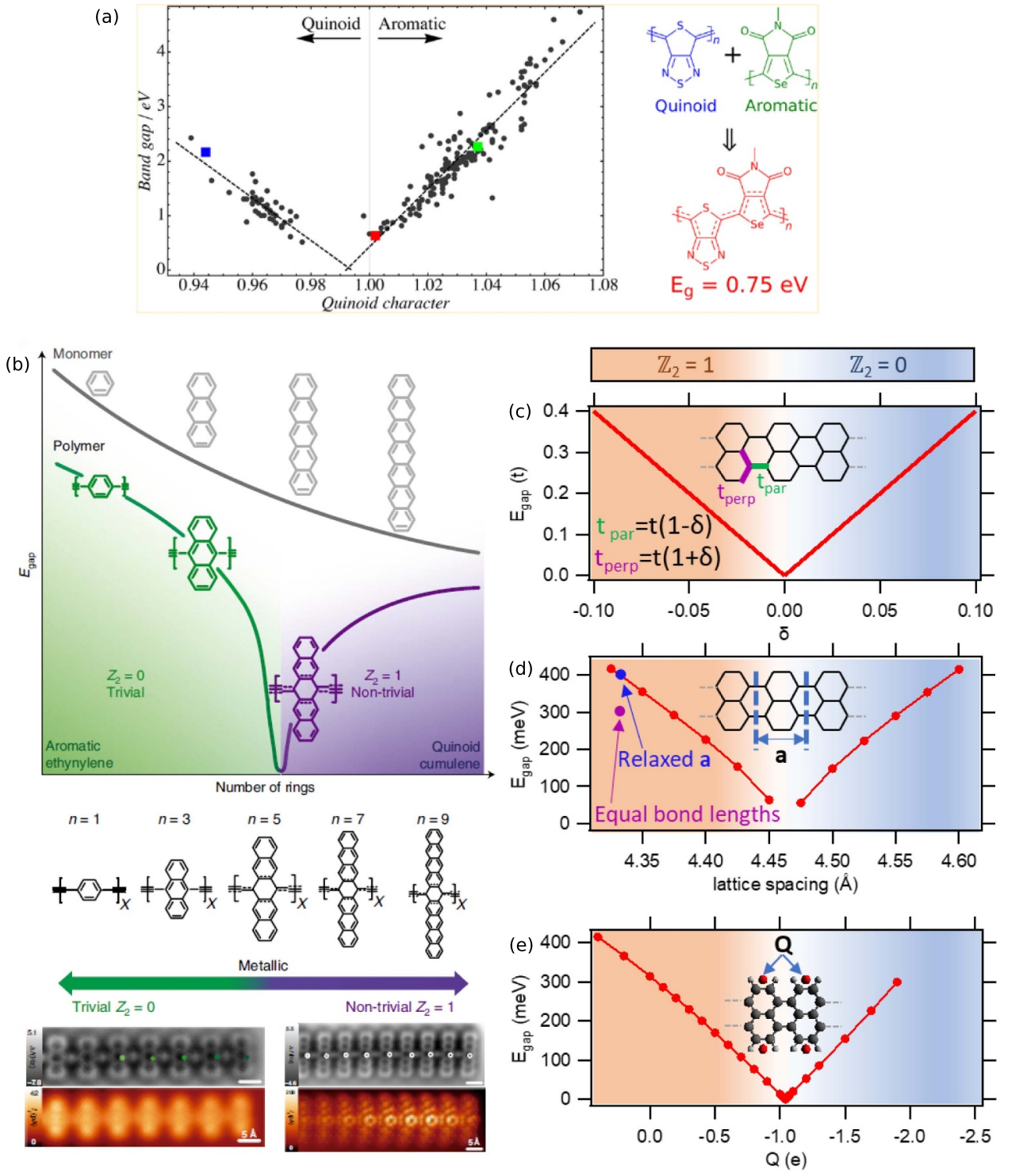


**Figure 16.** (a) Calculated band gap of homopolymers and copolymers according to their quinoid or aromatic character, as represented by a parameter that indicates an increasing quinoid (<1) or aromatic (>1) character as the values depart from 1. Mixing aromatic (green) and quinoid (blue) units results in more balanced conjugation structures with consequently lower band gaps (red). (b) Schematic evolution of the band gap of acene monomers and acene-based polymers with increasing size of acene monomer. The latter case shows a phase transition between trivial and non-trivial topological classes accompanied by transformation of the $\pi$-conjugation of the polymer. At the bottom, noncontact-AFM and STM images of the ends of an anthracene-based polymer and a pentacene-based polymer are shown, revealing an end-state for the latter but not for the former. (c) Calculated band gap and topological class for 5-atom wide AGNRs as a function of the hopping constants in the bonds parallel to the ribbon's longitudinal axis ($t_{par}$) or perpendicular to it ($t_{perp}$). (d) Calculated band gap topological class for the same ribbons as a function of its lattice spacing $a$. (e) Calculated band gap topological class for the same ribbons as a function of the charge on the Yukawa potentials marked in the inset. (a) Reprinted with permission from [163]. Copyright (2013) American Chemical Society. (b) Reproduced from [69], with permission from Springer Nature. (c) Reprinted with permission from [104]. Copyright (2020) American Chemical Society.

structure at the polymer's ends can be nicely resolved from the bond-resolving nc-AFM measurements [69].

There are also alternative ways that have been proposed to move across the aromatic/quinoid or topological phase map that do not even modify the backbone structure of the $p_z$ orbital network. Taking into account that topology can be associated to orbital symmetries, it seems intuitively easy to modify those by changing the carbon backbone and thereby the network of $p_z$ electrons. However, it is less intuitive to assume their modification for a fixed electron network. One of the various ways is through a polymer length control. By way of example, the previously described pentacene-based polymers undergo a topological transition and become trivial for lengths below ~26 unit cells [165]. The reason underlying such length-dependent topological transition is a pseudo Jahn–Teller effect driven by vibronic coupling of low-lying excited states to vibrational modes of specific symmetries, whereby a new ground state is established [165, 166]. This mechanism may impose a similar length-dependence in the topological class also to other $\pi$-conjugated systems like GNRs.

Alternatively, TB simulations have shown that a key to move across the topological phase diagram is the control of the hopping constants between lattice sites, in such a way that differences can be created for different types of bonds [54, 104]. For example, the topological class of AGNRs with five atoms across its width (5-AGNRs) and ending with a row of zigzag atoms changes from trivial to nontrivial if the $\pi$-bonds parallel to the ribbon's axis display a weaker or stronger hopping constant than the transverse bonds (figure 16(c)) [104]. In fact, the same results were obtained if only the hopping constant of the outermost parallel bonds between the singly hydrogenated carbon atoms at both sides of the ribbon are made different from the rest. One way to controllably modify the hopping constants of parallel and transverse bonds is by the application of uniaxial strain, as calculated in figure 16(d) for varying 5-AGNR lattice constants [104]. However, a similar effect can be obtained if the electrons feel a modulated electrostatic potential on different bonds. This has indeed been found to be the reason for 5-AGNRs to be topologically nontrivial. The positive partial charge on the hydrogen atoms at the sides make the electrostatic potential for the electrons to be more favorable on the outer bonds parallel to the ribbon, increasing the associated hopping constant and rendering 5-AGNRs nontrivial. This effect can, however, be inverted by a modified electrostatic potential. This has been proved at the theoretical level by adding a varying charge to Yukawa potential centers located in between the hydrogen atoms (figure 16(e)) [104], but could eventually be realized experimentally, e.g. with varying edge functionalization with polar groups [167, 168] or electron-rich atoms like fluorine instead of hydrogen.

A somewhat related concept that has also been proposed at a theoretical level is based on a topological inversion process driven by transverse electric fields. GNRs that are asymmetric across their width can be engineered so as to have the valence and conduction bands displaying opposite energy shifts in response to transverse electric fields, potentially enabling a band inversion above a critical electric field that would bring along a change in the topological class. A type of ribbons that has been proposed to fulfil the requirements for transverse electric field-induced topological changes is 11-AGNRs with nitrogen and boron heteroatom dimers on opposite sides of the ribbon [169]. Taking a step beyond merely moving across the topological phase diagram for the whole ribbon, a superlattice electric field of modulated strength or direction (as may, e.g. be created by a periodic array of parallel gates with alternating bias values), has been further proposed to allow for the controlled generation of periodic topological interface states whose coupling can be programmed by the spatial profile of the electric field that determines the interface state spacing [169].

All in all, controlling the topological class of carbon nanostructures allows for the tailored generation of magnetic states at the ends, edges, or topological interfaces within their carbon backbones, which represents an extraordinary playground for the generation of custom-made materials.

### 5.4. Topological defects

Most of the structures discussed above are benzenoid, made up by hexagonal carbon rings. However, the presence of topological defects as given by carbon rings with a different number of atoms has a notable impact on the materials' properties, including their magnetism. For example we analyze in the following the effect of four-membered rings on two closely related linear conjugated structures. Both consist in acene segments fused by four-membered rings. In one case the acene segments are fused in a linear configuration (figure 17(a)), whereas the other displays a staggered configuration (figure 17(b)). Interestingly, whereas the linear structure displays closed shell character [170], the staggered structure is predicted to be predominantly open-shell [170, 171]. As explained in section 5.3.2, acenes in their closed-shell structure display one Clar sextet independently of their length and it is only for higher acenes that they display a notable open-shell character. The structures shown in figures 17(a) and (b) feature periodically fused tetracene segments, which on their own are closed-shell structures. Each tetracene segment hosts one Clar sextet in its closed-shell form, which can be located on any of its rings and can thus avoid being next to the four-membered rings. When the tetracene units are fused in a linear way (figure 17(a)), resonannce structures can be drawn such that no $\pi$-bond locates on the four-membered ring. However, that is no longer possible when the tetracene units are fused in a staggered way (figure 17(b)). In this configuration, $\pi$-bonds necessarily participate in the four-membered rings, which promotes their antiaromatic character (marked in red in figure 17(b)) [172] and is energetically unfavorable. However, this can be avoided in the open-shell structure shown in figure 17(b). The drawn resonance structure has no $\pi$-bond on the four-membered rings, avoiding their antiaromaticity [173, 174]. For the linear structure, an open-shell structure would thus gain one Clar sextet per unit cell at the expense of two radicals, which is not energetically favored for short acene constituents (see sections 3.3 and 5.3.1). Instead, for the staggered structure the open-shell configuration similarly gains only one Clar sextet, but additionally

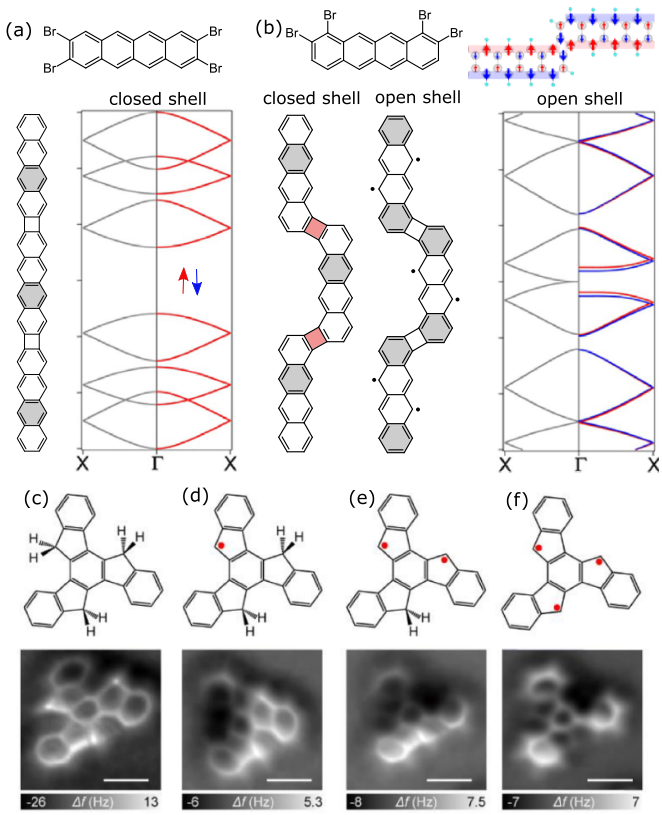


**Figure 17.** (a) Reactant and product structure, along with the calculated band structure for the linearly fused acenes displaying four-membered rings at the junctions. (b) Proposed reactant and expected product structure in its closed-shell and open-shell forms, along with the calculated band structure for the polymer comprising staggered acenes fused by four-membered rings. The top drawing depicts the schematic spin configurations with the carbon tetragon acting as a spin switch. In the molecular structures the Clar sextets are highlighted in grey and antiaromatic ciclobutadiene moieties in red. Chemical structure and associated nc-AFM images of truxene (c) and its derivatives after dehydrogenation of one (d), two (e) and three (f) of its $sp^3$ carbon atoms at the pentagonal rings. (a) and (b) [170] John Wiley & Sons. © 2019 Wiley-VCH Verlag GmbH & Co. KGaA, Weinheim. (Inset of (b)) Reprinted figure with permission from [171], Copyright (2016) by the American Physical Society. (c) Reproduced from [179]. CC BY 4.0.

limits the antiaromatic character of its four-membered rings. Under these circumstances, the open-shell configuration is favored, representing a clear case in which the topological defect in form of four-membered rings lowers the threshold number of extra Clar sextets required to favor open-shell structures.

Interestingly, in addition to promote the open-shell character of these structures, the four membered rings act as spin-switches [171]. This can be understood from a conceptually very simple idea, namely that opposite spins in neighboring C atoms allow for their $\pi$-bonding and therefore are stabilizing, whereas for equal spins the Pauli exclusion principle prohibits their bonding and such configuration is therefore destabilizing [83]. Even-membered rings allow for configurations in which the spins of all neighboring C atoms are antiferromagnetically oriented. The same applies to the four-membered rings in the staggered structure of figure 17(b). However, the spin alternation causes a reversal of the spin when comparing the same side of neighboring acene segments (figure 17(b)).

The scenario with odd-membered rings is different, since it does not allow for configurations in which all atoms display an alternant spin alignment. This causes spin-frustration [50], which reduces the stability of such structures [83], and is typically mirrored in lower HOMO–LUMO gap values [175]. This is, e.g. illustrated in figure 1, with structure **5** displaying a comparable gap to structure **3** in spite of its lower number of carbon atoms. These low HOMO–LUMO gaps in turn facilitate their spin-polarization. Examples of structures synthesized and studied under vacuum in which odd-membered rings facilitate the spin-polarization are polyindenoindene [176] or polyindenofluorene [177, 178], in which their prevailing open-shell configurations gain only two Clar sextets for every pair of radicals, both cases being therefore below the common 'three sextets per radical pair' threshold described in section 3.3. Nanographenes with a single pentagonal ring [52, 108] and GNRs with five-membered rings at the edges [27] have been characterized.

Besides facilitating the spin-polarization of low energy states by reducing the HOMO–LUMO gaps, topological defects in the form of odd-membered rings also have the peculiarity of potentially resulting in structures with an odd number of $p_z$ electrons, which automatically causes topological frustration and the concomitant appearance of radical states, as exemplified with structure **6** in figure 1 [101, 108].

A nice example systematically following the magnetism of molecules arising from topological defects is based on truxene derivatives (figures 17(c)–(f)) [179, 180]. The as-deposited truxene molecule displays three doubly hydrogenated $sp^3$ carbon atoms at the outer pentagon vertices (figure 17(c)). As readily explained in previous sections, their dehydrogenation and $sp^3$ to $sp^2$ rehybridization can be triggered by tip-induced manipulations, controllably affecting one (figure 17(d)), two (figure 17(e)), or the three pentagonal rings (figure 17(f)). Dehydrogenation of one ring results in an odd number of $p_z$ electrons and thus one radical and a spin state $S = 1/2$. Dehydrogenantion of a second pentagonal ring makes the total number of $p_z$ electrons even again and the resonance structure can be drawn both as a closed- and open-shell. Interestingly, calculations predict the latter to dominate, with the two radical spins aligned ferromagnetically and a $S = 1$ ground state. The same scenario holds when the third radical is generated, ultimately generating a high-spin quartet [179, 180]. These topological defects thus facilitate the generation of high-spin molecules with smaller molecular weights as compared to, e.g. [n]-triangulenes, and predictions are such that the same ferromagnetic alignment would hold also for an increasing number of radicals in two-dimensional networks based on these truxene-derivatives [179].

### 5.5. Heteroatoms

Although always in close relation to the previous sections, the origin of magnetism in carbon-based nanostructures (or alternatively a way to tune it) can also be sought in the presence

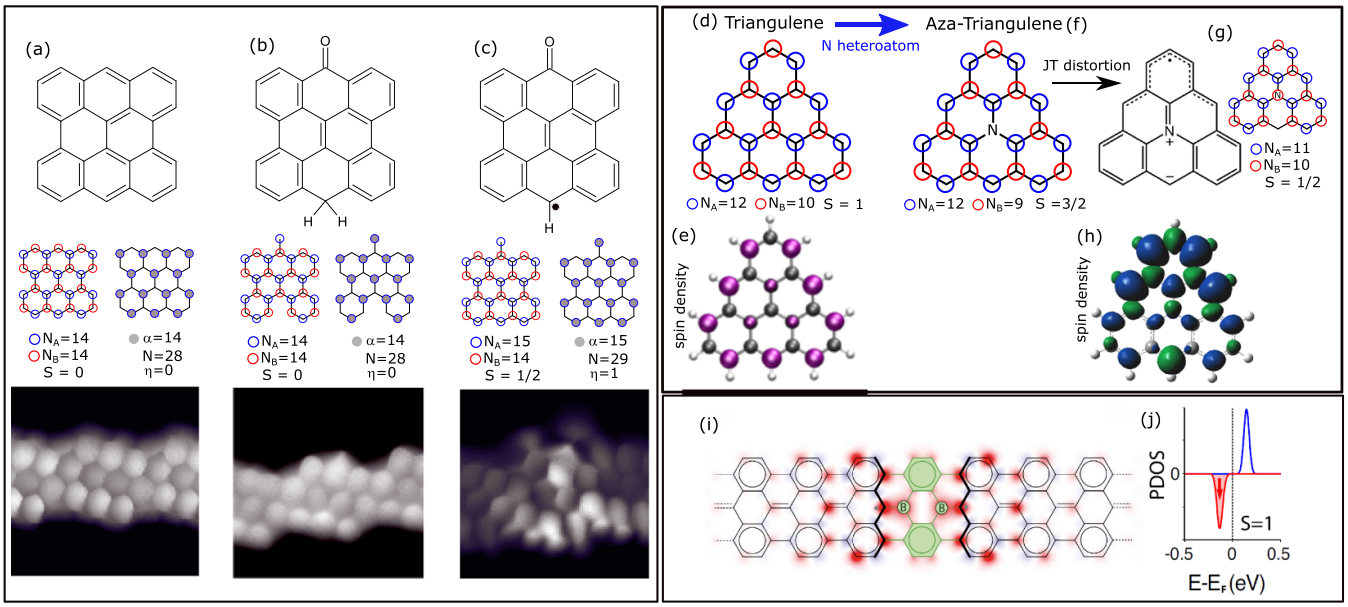


**Figure 18.** The unit cell, sublattice balance and $\eta$ analysis of (a) a chiral GNR with four zigzag lines across its width, (b) the same unit cell with the central edge atom functionalized on one side with a ketone and on the other side with an extra hydrogen, and (c) for the same unit cell with only one central edge atom functionalized with a ketone. Below are the corresponding bond-resolving STM images. (d) Counting rules applied to triangulene. (e) Spin density for triangulene. (f) Counting rules applied to aza-triangulene in its undistorted 3-fold symmetric form. (g) Best fitting resonance structure for the ground state of aza-triangulene undergoing a Jahn–Teller distortion and application of the counting rules. (h) Calculated spin density for aza-triangulene in its ground state. (i) Structure and spin density around a 2B substitution in 7-AGNRs. (j) Projected DOS (PDOS) on the structure displayed in panel (i). (a)–(c) Reprinted figure with permission from [181]. Copyright (2021) American Chemical Society. (e) Reproduced from [22], with permission from Springer Nature. (h) Reproduced from [182]. CC BY 4.0. (i), (j) Reproduced from [70]. CC BY 4.0.

of heteroatoms. Let us first focus on edge functionalization. Just as hydrogenation can cause an $sp^2$ to $sp^3$ rehybridization and thereby effectively remove a $p_z$ electron (and the process can be reversed by dehydrogenation), different types of chemical functionalization can have the opposite effect. An example is pictured in figures 18(a)–(c), which shows the unit cell of chiral GNRs that have been synthesized on surfaces under vacuum [144, 145]. Sublattice imbalance and nullity of the pristine ribbons are both zero, displaying no magnetism (figure 18(d)). As will be discussed later on, these structures are highly unstable and easily react with gases like $O_2$ even at room temperature (RT) [181]. The most common reaction product is a ketone side-functionalization of the ribbon's edges. In the oxidation process, the oxygen displaces the previously present hydrogen atom, whose migration to the opposite edge is favorable and thus very common (figure 18(e)) [181]. The oxygen displays an $sp^2$ configuration and therefore contributes with an extra $p_z$ electron to the product structure, in particular to sublattice A, whereas the hydrogenation on the opposite side removes a $p_z$ electron from that same sublattice. The sublattice balance and $\eta$ are consequently unaffected. However, as the extra hydrogen is controllably removed by a scanning probe, the missing $p_z$ electron is recovered and, with the extra $p_z$ electron of the ketone group, a sublattice imbalance is generated and $\eta$ becomes 1. That is, a new radical is created, which experimentally becomes evident from the enhanced contrast in the low bias bond-resolving STM images due to the associated Kondo resonance (figure 18(c)) [181].

A similar scenario occurs for chiral GNRs in which each unit cell is doubly functionalized with a ketone on either side [183]. Whereas the perfect structure shows sublattice balance and no magnetic states, defective unit cells with one missing ketone develop a radical state [103]. These systems are very interesting to study the magnetic interactions between those states when more than one is present on the same ribbon at sufficiently close distances. A relevant conclusion from such studies is that Ovchinnikov's rule [76] or Lieb's theorem [75] do not necessarily apply any longer as heteroatoms are involved. Along the same lines, the description of these heteroatoms as mere additional $p_z$ states in a TB approach turns out to be insufficient, and additional chemical information in the form of modified hopping constants and on-site energies are required for an adequate modeling [103].

In a similar way as edge functionalization with heteroatoms can bring about or modify the magnetism of carbon nanostructures, the same occurs within the backbone structure. By way of example, the addition of substitutional nitrogen is predicted to trigger ferromagnetism in graphene [184, 185]. Its effect on well-defined nanographene structures has been studied for example in aza-triangulene, which allows for an interesting comparison with the magnetic properties of conventional triangulene. As discussed in earlier sections and reminded in figure 18(d), the latter has a sublattice imbalance of 2 and thus displays a triplet ground state with $S = 1$. The associated spin density displays a three-fold symmetric distribution as shown in figure 18(e) [22]. If the central atom is exchanged by a

nitrogen atom in aza-triangulene, naively one would assume a double occupancy of its $p_z$ orbital, which would in turn remove its contribution to the $N_B$ count in Ovchinnikov's rule and result in a quartet ground state ($S = 3/2$, figure 18(f)). However, DFT calculations predict this molecule to have a doublet ground state ($S = 1/2$). The odd number of $p_z$ electrons makes it favorable for the molecule to undergo a Jahn–Teller distortion [56] and adopt a structure with lower symmetry that is best represented by the zwitterionic resonance form displayed in figure 18(g) [182]. As can be observed, the zwitterion displays only one radical that is delocalized around one of the molecule's vertices, in agreement with its predicted spin ($S = 1/2$) and its spatial distribution (figure 18(h)). Besides, it also reconciles the ground state $S = 1/2$ with Ovchinnikov's rule, since the bonding nature of the N $p_z$ orbital justifies its counting towards $N_B$, whereas the carbon atom hosting the negative charge at the low side edge has its $p_z$ orbital doubly occupied and does not count towards $N_A$ ($N_A = 11$, $N_B = 10$, $S = 1/2$, figure 18(g)) [182].

Another nice example of backbone heteroatom doping is the substitution of carbon by boron atoms. In contrast to N, B in its $sp^2$ configuration has its $p_z$ orbital empty. Naively this would equally remove it from its sublattice count and thereby cause a net spin according to Ovchinnikov's rule, in a similar way as the $sp^2$ to $sp^3$ rehybridization by hydrogenation of graphene does [78]. This is, however, not the case in graphene, where it merely acts as a point potential rather than rupturing the conjugated electron system [186]. However, if two boron atoms are introduced into the backbone of GNRs instead, they can trigger a sufficiently strong modification of the conjugation pattern in their close proximity to modify the orbital's symmetry and thus their topology [66, 70, 187]. As a result, topological interface states appear at the junctions to the undoped GNR regions. This has been realized for example with B atoms within 7-AGNRs as pictured in figure 18(i), which also represents the spatial distribution of the spin density [70]. The latter looks reminiscent of the spin density associated to the end-states of 7-AGNRs (assuming a termination at the thicker solid lines), which distribute symmetrically to either side of the borylated section. Most interestingly, the two spins align ferromagnetically into a $S = 1$ ground state (figures 18(i) and (j)) in spite of their distribution on either side of the borylated section on opposite sublattices, which would normally favor an antiferromagnetic alignment. This surprising result has been ascribed to the strong barrier imposed by the borylated section, which prevents conjugated electrons from hopping across. The disconnection of the two boundary states at each side hinders the (antiparallel) kinetic exchange between them. The stabilization of the triplet configuration is then the result of the weak direct overlap between both spin-polarized boundary states through the 2B barrier, which, due to the tiny hopping between them, dominates the exchange interaction and induces the ferromagnetic alignment of the spins according to Hund's rule [70].

It is worth noting that, apart from causing the appearance of magnetism via one mechanism or another, the introduction of heteroatoms has also been found to allow for the stabilization of magnetic states and their electronic decoupling from the underlying metallic substrates merely by a modification of the molecular adsorbate's adsorption geometry [188, 189].

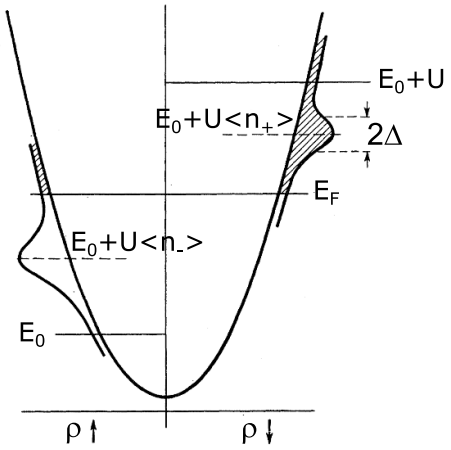


**Figure 19.** Density of state distribution for spin up (left) and spin down (right). The 'humps' at $E_0 + U\langle n_-\rangle$ and $E_0 + U\langle n_+\rangle$ are the virtual levels of the magnetic state, of width $2\Delta$, for up and down spins, respectively. The number of electrons $\langle n_-\rangle$ and $\langle n_+\rangle$ occupying them correspond to the integration of their unshaded region below the Fermi level and determine the Coulomb repulsion they feel from electrons of the opposite spin and thereby the energy deviation of the virtual states with respect to $E_0$ and $E_0 + U$. Reprinted figure with permission from [190]. Copyright (1961) by the American Physical Society.

### 5.6. Charge transfer

All examples that have been reviewed so far correspond to carbon-based nanostructures that intrinsically display an open-shell character. When molecules are adsorbed on solid substrates, another very important factor needs to be considered. The effects of the molecule-substrate interactions on the magnetic properties of the molecular structures can be manifold. They may quench the intrinsic magnetism of the molecules or instead endow magnetic properties to carbon nanostructures that in a free-standing configuration would display a conventional closed-shell character. In this respect it is instructive to analyze the simple picture of the Anderson model for single magnetic states (figure 19) [190].

This model describes a magnetic state at energy $E_0$. Placing a second electron into that same state implies a Coulomb repulsion $U$ between the two electrons, thus requiring an addition energy of $E_0 + U$. However, as the states interact with their environment (e.g. the substrate) and get a finite width, if their tails cross the Fermi level their occupation deviates from 1 and 0 and instead becomes $\langle n_+\rangle$ and $\langle n_-\rangle$ for spin up and spin down, respectively. The partial occupation $\langle n_-\rangle$ causes Coulomb repulsion on the spin up state and increases its energy to $E_0 + U\langle n_-\rangle$, whereas the Coulomb repulsion on the spin down state is lowered to $E_0 + U\langle n_+\rangle$ (figure 19). As may be directly inferred from this simple picture, the net spin density ($\langle n_+\rangle - \langle n_-\rangle$) is maximized for large $U$ values, low $\Delta$ values and for binding energies $E_0$ as close as possible to $U/2$.

All of these relevant parameters can be affected by the substrate and the supramolecular environment. By way

of example, the binding energy $E_0$ of an electronic state will greatly vary with substrates of different work function [191–193]. In addition, the state's width $\Delta$ is crucially dependent on the specific substrate–adsorbate interactions and hybridization [191, 193]. At the same time, the latter determines the adsorption height that, along with the dielectric properties of the substrate, have an important effect on the Coulomb energy $U$ [102, 191]. However, not only the substrate plays a role, but also the supramolecular environment. Besides the possibility of intermolecular charge transfer in so-called 'charge-transfer complexes', different intermolecular interactions can also bring along modified interaction strength and hybridization with the substrate [193–196], as mirrored, e.g. in varying adsorption heights [194, 195]. Also the energy level alignment may vary [193–195], which can eventually cause changes in the adsorbate's charging state [192, 197].

If a closed-shell adsorbate undergoes charge transfer to or from the substrate, it may display molecular magnetism if the following conditions are additionally met. According to the Anderson model [106, 190], the Coulomb interaction $U$ should be greater than $\Delta$ and the binding energy $E_0$ should be in the range of 0 to $U$, being most favorable for magnetism if it is around $E_0 = U/2$ [190]. These conditions guarantee a close to integer charge state of the adsorbate, with well-differentiated spin-up and spin-down electron population. A low $\Delta$ value, which translates into a sufficiently small electronic coupling of adsorbate and substrate, is thus a key parameter to promote magnetism.

A good example is the case of pentacene on Ag(001) (figures 20(a) and (b)). Experiment and calculations both reveal the transfer of nearly a full electron from the silver substrate to pentacene's LUMO level [191]. However, $E_0$ is roughly centered around the Fermi level and the state's width $\Delta$ is much greater than $U$ (figure 20(c)) [191]. The spin-up and spin-down population on pentacene is thus similar and the result is a non-magnetic molecule-adsorbate system in spite of the quasi integer charge transfer. However, as the pentacene molecule is decoupled from the Ag(001) by a MgO monolayer (figures 20(d) and (e)), the effect is two-fold. On the one hand, the screening from the substrate is significantly reduced, which translates into a greatly enhanced $U$. On the other hand, the molecule's electronic coupling to the silver is much more limited, which consequently reduces $\Delta$. In the end, two well-defined molecular resonances are observed below and above the Fermi level that are associated to the SOMO and SUMO, respectively (figure 20(f)) [191]. This situation exactly fits the Anderson model applied to a magnetic molecule-substrate system.

A closely related system with an intermediate molecule-substrate coupling between that of the systems described above was studied with 5,18-dihydroheptacene directly on the Ag(001) surface [198]. This molecule shares the carbon backbone of heptacene but displays doubly hydrogenated C atoms at its second ring (figure 20(g)). The $sp^3$ hybridization of these atoms breaks the conjugation along the molecule, for which the frontier electronic states are determined by the longest conjugated segment within the molecule [198–200], that is, a pentacene segment. This confers the 5,18-dihydroheptacene molecule electronic properties that are strikingly similar to those of pentacene, as sustained, e.g. by the energy and shape of its frontier orbitals (figures 20(h) and (i)) [198, 199]. However, the $sp^3$ C atoms within the carbon backbone endow the molecule with a non-planar structure that causes its self-decoupling from the underlying substrate (figure 20(j)). Although a less effective decoupling than that provided by insulating buffer layers like MgO, it is still sufficient for the molecules to display in STM experiments charging peaks (with its associated vibronic satellites) that are associated to a double tunneling barrier and, most importantly, magnetism as proved by an associated Kondo resonance at zero bias [198]. The Kondo resonance still implies a minor molecule-substrate coupling, since it relates to the screening of the molecular spin by the substrate electrons. It is, however, small enough to stabilize a singly charged molecule with net spin $S = 1/2$.

Although exemplified above with pentacene or its derivatives on Ag substrates, the appearance of magnetism upon adsorption in molecules that in their free-standing configuration are conventional closed-shell structures has been observed also with other molecules and substrates [109, 197, 202, 203].

Nevertheless, just as charge transfer may cause the appearance of magnetism in otherwise non-magnetic materials [197, 198], it can equally well quench the magnetism of intrinsically magnetic carbon-based molecules [104, 182, 204–206] or graphene defects [78]. For the latter, this could be nicely tested by comparing the magnetism of defects in pristine and doped graphene samples. Whereas indirect but unambiguous fingerprints of magnetism were observed with pristine graphene, the use of $p$- or $n$-doped graphene removed the electron sustaining the unpaired spin moment or paired it up with an extra electron, respectively, in either case resulting in non-magnetic systems [78]. Depending on the system, it may also be important to consider in which direction the electron transfer takes place. By way of example, aza-triangulene, which in its neutral form is predicted to display a ground state with $S = 1/2$ [56, 182], presents a triplet ground state ($S = 1$) when it donates an electron to the substrate (as occurs on Au(111)), but becomes a closed-shell molecule when it receives an extra electron from the underlying substrate (as occurs on Ag(111)) [182].

In the case of carbon-based nanostructures that have been obtained by OSS, the most commonly utilized substrate is Au(111). Its high work function endows this substrate a strong tendency to receive electrons from the molecular adsorbates atop [207]. The molecule's loss of spin-carrying electrons to the substrate can modify or even quench their associated magnetism. This situation, in which the resonances of the magnetic states appear at energies above the Fermi level and are thus unoccupied, has been observed with many disparate molecular systems, like the end-states of AGNRs [102, 104, 208] or other linear polymers [69], a variety of topological interface states [26, 68], or the radical $\pi$-states of porphyrin derivatives [204]. For the latter, the charge transfer of some specific derivatives could be controlled by modifying the adsorption

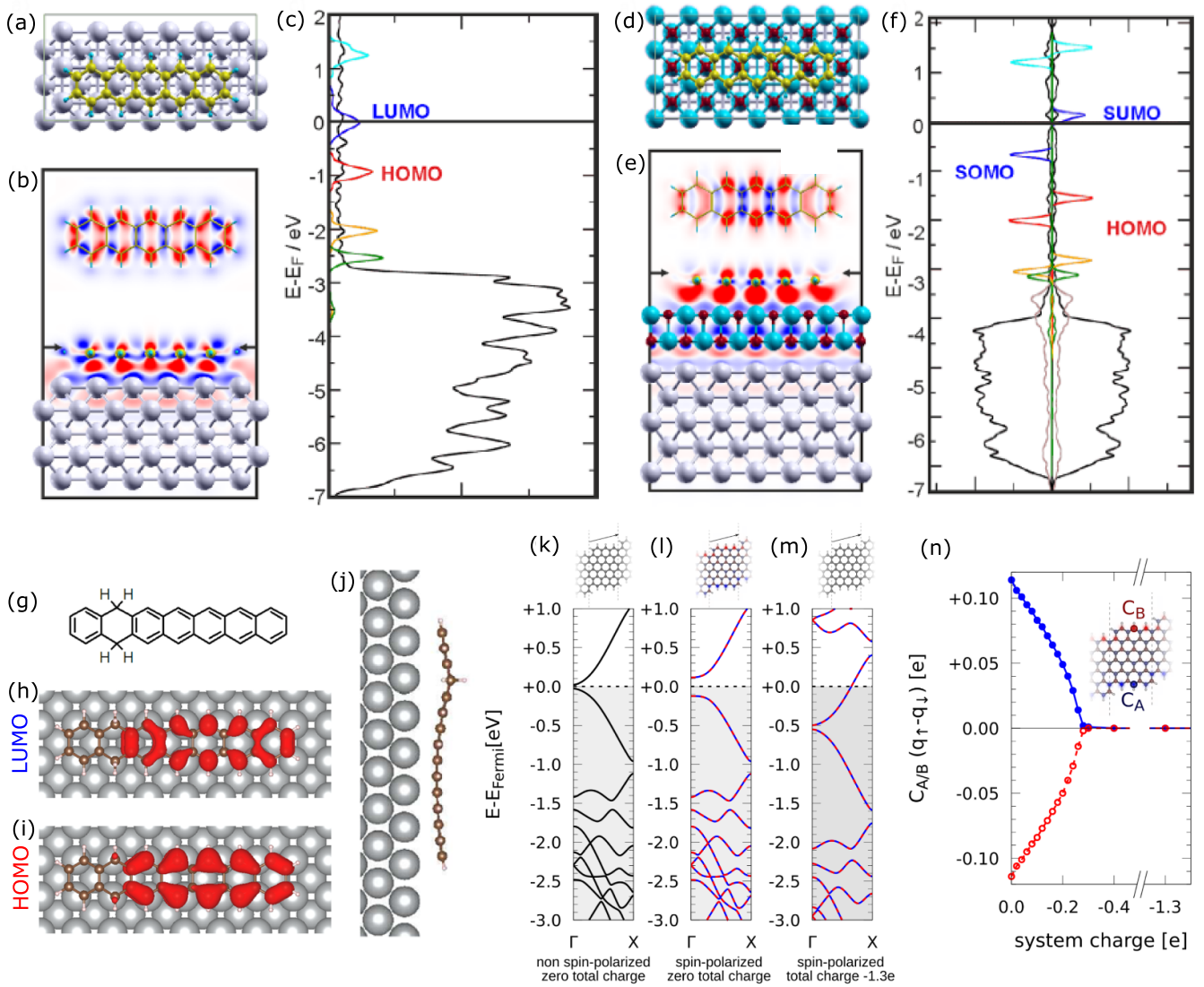


**Figure 20.** (a) Top view of the most stable adsorption configuration of pentacene on Ag(001). (b) Horizontal (top) and vertical two-dimensional cuts showing the charge density differences induced by pentacene adsorption on the Ag(001) substrate. The arrows indicate where the horizontal cut has been made. Red shows accumulation and blue depletion of charge, respectively. (c) PDOS obtained for the pentacene/Ag(001) interface using the GGA functional. The DOS projected onto the Ag atoms (black) has been reduced for better visibility. In addition, the projections on the molecular orbitals are shown for LUMO+1 (cyan), LUMO (blue), HOMO (red), HOMO–1 (orange), and HOMO–2 (dark green). Equivalent calculations for the (d) adsorption configuration, (e) charge density differences and (f) spin-polarized PDOS for the pentacene/MgO/Ag(001) interface, the latter obtained with the HSE functional. (g) Chemical structure of 5,18-dihydroheptacene, calculated charge densities associated with (h) its LUMO and (i) its HOMO level, as well as (j) a lateral view of its adsorption configuration on Ag(001). (k) Relaxed atomic configuration (top) and electronic band structure (bottom) of chiral (3,1,6)-GNRs without spin-polarization. (l) and (m) Spin density (top) and spin-polarized band structure (bottom) for the neutral case and upon charge transfer of 1.3 electrons per unit cell, respectively. (n) Spin-polarized electron density at the marked carbon atoms at the ribbon's edges as a function of charge transfer. (a)–(f) Reproduced from [191]. CC BY 4.0. (g)–(j) Reproduced from [198]. CC BY 4.0. (k)–(n) Reproduced from [201]. CC BY 4.0.

geometry through scanning probe manipulations, which consequently allowed tuning its magnetic state accordingly [204].

It should also be mentioned that even for systems in which the magnetism is associated to more electrons, like in chiral or ZGNRs, charge transfer is predicted to similarly affect the magnetism [79, 201, 205]. By way of example, chiral (3, 1)-GNRs with six carbon atoms across their width develop spin-polarized edge states, whereby their band structure widens its gap to avoid the instability associated with large density of states near the Fermi level (figures 20(k) and (l)). However, a charge transfer of around one electron per unit cell, as experimentally observed on silver surfaces, quenches the magnetization and causes the band structure to become like that of non-spin-polarized ribbons (figure 20(m)) [201]. A more detailed analysis of the spin-polarization in this kind of ribbons as a function of charge transfer indeed reveals that an electron transfer of only 0.3 electrons per unit cell is already enough to fully quench any magnetization (figure 20(n)) [201].

Another example are ZGNRs with six atoms across their width. An indirect fingerprint of their magnetism (in particular the observation of a correlation gap) was only observed when adsorbed on a NaCl buffer layer, but not directly on Au(111) [25]. For this latter case, however, no evidence of the flat band was observed even above the Fermi level. Therefore, besides charge transfer, an excessively large hybridization of the flat band with the underlying substrate cannot be discarded either as the reason for the lacking magnetism, as indeed suggested by the appearance of those resonances in closely related ZGNRs with nitrogen dopants that allow for their electronic decoupling from the substrate by a modified adsorption geometry [188, 189]. This same hybridization scenario may also be the reason for the lacking magnetism in superheptazethrene on Au(111). Whereas in solution and in the solid state it was found to have an open-shell character [209], adsorbed on Au(111) it displays a closed-shell character in spite of no obvious charge transfer evidences, with comparably shaped HOMO and LUMO resonances almost symmetrically positioned around the Fermi level [210]. Only its larger 'sister molecule' supernonazethrene, with a consequently more robust magnetism, shows clear magnetic fingerprints on Au(111) [211]. As discussed later on in the frame of the carbon nanostructure's reactivity, comparative studies on weakly and more strongly interacting surfaces also show how the magnetism of molecules like, e.g. [7]-triangulene may survive on the former but be quenched by the strong hybridization with the substrate on the latter [122].

Another important point to remind regarding charge transfer is that Ovchinnikov's rule and Lieb's theorem no longer apply for doped systems. Applied to GNRs this means that, for doping levels at which the magnetization is not yet quenched, ground states other than that predicted for neutral ribbons (whether chiral or zigzag edged) are allowed and may thus not correspond to the expected ferromagnetic alignment of the spins along each edge of the ribbons and an inter-edge antiferromagnetic alignment [79, 212, 213].

## 6. Magnetic interactions

### 6.1. Electron spin pairs

As we have seen in figures 7 and 9 the emergence of two unpaired electrons in a graphene nanostructure can lead to a sizable spin interaction on the $J \sim 1$–$100$ meV scale, promising for potential applications in RT spin-logic operations [24] Some characteristic observations of exchange-coupled spins are listed in table 2. The current record of $J = 102$ meV was observed in [5]-rhombene on Au(111) [133]. Distance-dependent effects in the spin interaction have been reported [24, 42, 103, 215], including dimers of asymmetric rhombus-shaped nanographenes [101, 124], in which the exchange coupling clearly correlates with the spacing between the rhombus sides displaying the largest spin density.

A variety of analytical arguments and more complex calculations have been utilized to model and understand the interactions between the spins of different electrons in singly occupied molecular states [41, 44]. The dependence of exchange coupling $J$ on structural parameters have also been analyzed theoretically [216, 217].

**Table 2.** Examples of reported exchange-coupled electron spins in open-shell nanographenes.

| System | Substrate | $J$ (meV) | Reference |
|---|---|---|---|
| (3, 1)-chiral GNR junctions | Au(111) | 3 to 10 | [52] |
| Clar's goblet | Au(111) | 23 | [24] |
| [3]-Triangulene | gas phase | $-570$[a] | [56] |
| Extended triangulene (ETRI) | gas phase | $<-60$[b] | [100] |
| Triangulene dimer | Au(111) | 14 | [42, 43] |
| Triangulene nanostar | Au(111) | 18 | [214] |
| Triangulene rings and chains | Au(111) | 14[c] | [43] |
| [5]-rhombene | Au(111) | 102 | [133] |
| Super-nonazethrene | Au(111) | 51 | [211] |
| Ketone-functionalized chiral GNRs | Au(111) | $-14$–$42$ | [103] |
| Defective [3]-rhombene dimers | Au(111) | $-6.6$–$42.9$ | [124] |
| Peripentacene | Au(111) | 40.5 | [61] |
| Periheptacene | Au(111) | 49.2 | [150] |

[a] Calculation based on the restricted active space configuration interaction (RASCI) method.
[b] MFH calculations with $U > 3$ eV.
[c] This work considers spin interactions beyond Heisenberg exchange within the bilinear-biquadratic (BLBQ) model.

Considering the simplest case of exchange coupling $J$ between only a pair of electron spins, we have seen that it can manifest itself in an antiferromagnetically (AFM) ordered ground state ($J > 0$), exemplified by the Hubbard dimer (section 2.3.1) and Clar's goblet (figure 7), or by a ferromagnetic (FM) ground state ($J < 0$), exemplified by [3]-triangulene (figure 10). It is worth to mention that ferromagnetic exchange $J$ is maximal for $C_3$ diradicals and that the symmetry also imposes that the lowest-energy excited state is a degenerate pair of closed-shell states [44] On the other hand, ferromagnetic exchange $J$ is minimal for $N_A = N_B$ diradicals, due to the disjointed nature of their zero modes [27, 44].

A typical fingerprint of the magnetic interactions may be seen in inelastic electron tunneling spectroscopy (IETS), i.e. symmetric features in $dI/dV$ at characteristic energies $|eV| = \Delta E_{ST}$ due to inelastic transitions between the singlet and triplet states. This is similar to spin IETS of single or few magnetic atoms with STM [218–223]. The possibility to split the triplet states by an external magnetic field allows to unambiguously confirm the spin origin of the IETS features. However, the Zeeman energy of $g\mu_B \sim 0.12$ meV T$^{-1}$ is typically much smaller than the resolution in IETS (thermal broadening $5.4k_BT \sim 2$ meV at liquid He temperatures, lock-in amplifier modulation voltage, finite lifetime of the spin states, etc) making such detection difficult in practice.

We note here that the intrinsic singlet-triplet gap of a molecule is also known to be reduced on a surface due to renormalization of the energies by coupling with substrate electrons [65, 224].

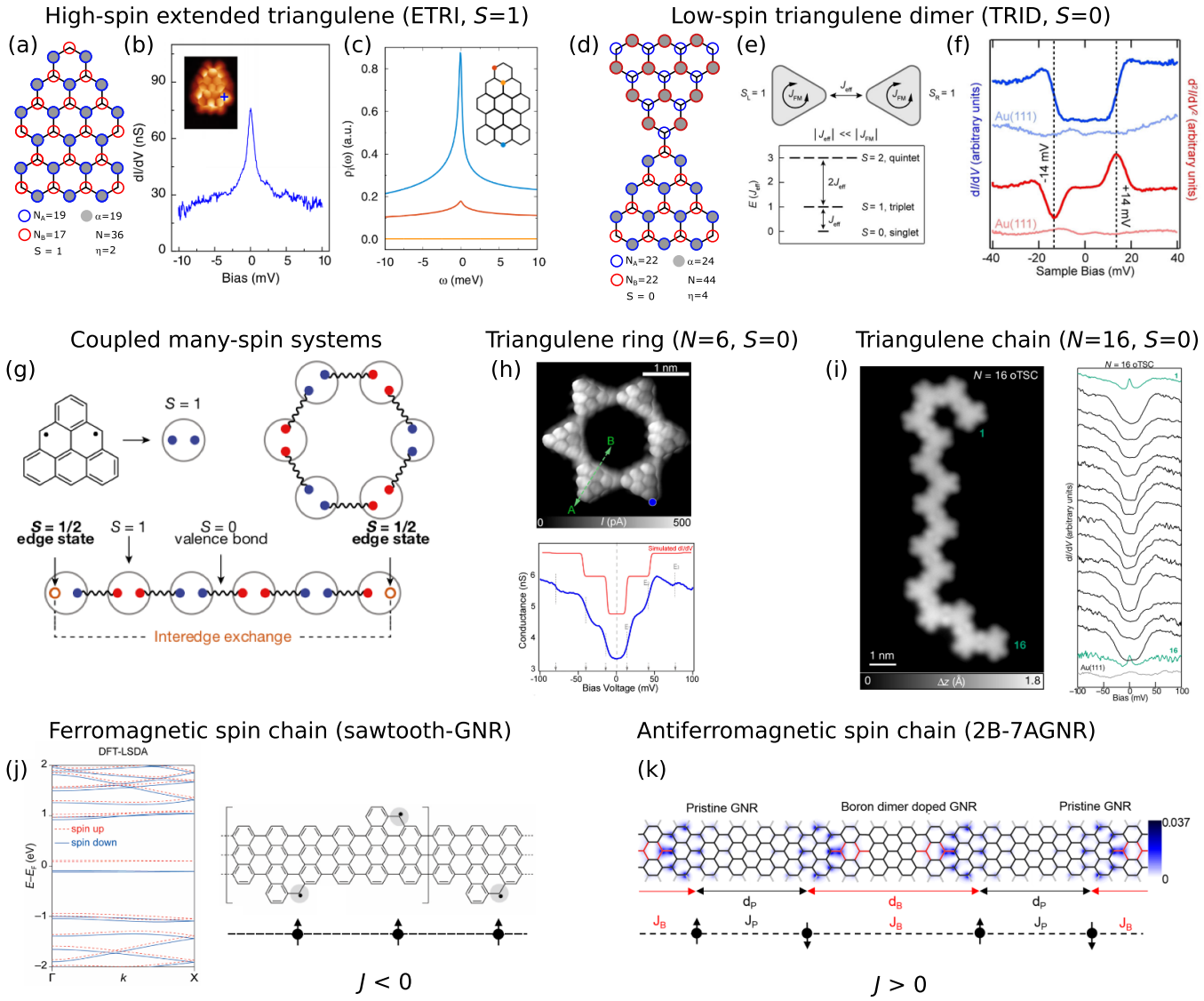


**Figure 21.** Interacting spins in graphene nanostructures and nanoribbons. (a) Structure of extended triangulene (ETRI) with indication of the sublattice imbalance. (b) Experimental signature of a zero-bias $S = 1$ Kondo resonance related to the triplet ground state of ETRI. (c) Spectral functions computed for ETRI coupled to the conducting electrons in the substrate, confirming the $S = 1$ Kondo effect. (d) Structure of a triangulene dimer (TRID) with sublattice balance. (e) Heisenberg dimer model and level diagram for the TRID with intra-triangulene ferromagnetic exchange and inter-triangulene antiferromagnetic exchange. (f) Experimental $dI/dV$ (blue curve) and IETS (red curve) spectra acquired on TRID, revealing inelastic the singlet-triplet excitation at 14 meV. (g) Heisenberg spin chains and rings of antiferromagnetically coupled $S = 1$ triangulenes. (h) Experimental bond-resolving STM image of a triangulene nanostar composed of $N = 6$ units and corresponding experimental and theoretical $dI/dV$ spectra. (i) Experimental STM image of a triangulene chain of $N = 16$ units and corresponding experimental $dI/dV$ spectra recorded over each unit. The zero-bias feature observed at the ends of the chain are Kondo resonances associated with the $S = 1/2$ edge states illustrated in panel (g). (j) Spin-polarized electronic band structure predicted from LSDA-DFT calculations for a sawtooth-GNR with radicals at each zigzag segment at the edges of a 7-AGNR backbone. The obtained ferromagnetic ordering ($J < 0$) is in accordance with Lieb's theorem due to sublattice imbalance. (k) Theoretical prediction of antiferromagnetic ordering ($J > 0$) between periodic interfaces of pristine and borylated 7-AGNR units. (b) Reprinted figure with permission from [100], Copyright (2020) by the American Physical Society. (c) Reprinted figure with permission from [65], Copyright (2021) by the American Physical Society. (e), (f) Reproduced from [42]. CC BY 4.0. (g), (i) Reproduced from [43], with permission from Springer Nature. (h) Reproduced with permission from [214]. CC BY-NC-ND 4.0. (j) From [27]. Reprinted with permission from AAAS. (k) Reprinted figure with permission from [66], Copyright (2017) by the American Physical Society.

Although IETS features for high-spin systems like [3]-triangulene or the related extended triangulene (ETRI) [100] have not been reported experimentally, another manifestation of magnetism for these $S = 1$ systems is the emergence of an underscreened Kondo resonance [225] which can further be split by an external magnetic field. Such features have recently been reported [100, 123] (figures 21(a)–(c)).

### 6.2. Interactions in few-spin systems

Going beyond a pair of electron spins, IETS features have also been observed in open-shell nanographenes such as the triangulene dimer with four unpaired electrons (figure 21(d)). Consistent with Lieb's theorem, the ground state is a singlet with the low-energy spectrum effectively described by an AFM ordering between two $S = 1$ units (figure 21(e)). The singlet-to-triplet excitation by IETS was observed around $V = 14$ meV (figure 21(f)). The direct transition to the quintet state ($S = 2$) by single tunneling electrons is forbidden according to the selection rule $\Delta S = 0, \pm 1$ [218–223].

Very recently, [3]-triangulene has also been demonstrated as a suitable $S = 1$ building block for realizing one-dimensional AFM systems through OSS strategies [43, 214]. As conjectured by Haldane [223, 226, 227], antiferromagnets for integer spins exhibit a finite excitation gap in the bulk, in contrast to the spin-half case. Furthermore, open-ended $S = 1$ chains are expected to host fractional $S = 1/2$ (topological) edge states at the boundaries. Figure 21(g) sketches the formation of coupled rings and chains of triangulene $S = 1$ units, with the latter exhibiting fractional $S = 1/2$ edge states. The collective spin states in these systems were revealed by multiple IETS features (figures 21(h) and (i)) well explained by the many-body spectrum obtained from exact diagonalization of the 1D Heisenberg model or its extension including a biquadratic coupling term as in the exactly solvable Affleck–Kennedy–Lieb–Tasaki (AKLT) model [228]. Notably, the fractional $S = 1/2$ termini states expected for open chains were revealed by a Kondo resonance in tunnel spectroscopy (green spectra in figure 21(i)). Antiferromagnetically coupled $S = 1/2$ and $S = 1$ molecular 1D chains have also been reported with metal-free porphyrins [229].

### 6.3. Extended spin chains and associated band-engineering

One-dimensional spin chains constructed with extended GNRs have also been proposed through topological band engineering with heterostructures or heteroatoms [26, 27, 63, 66–68, 70, 206, 230–232]. By rational design of precursor molecules and their mixtures, it is possible to vary the inter-radical spacing (and therefore their coupling) to engineer regular or disordered spin arrangements.

In figure 21(j) we show an example of a 7AGNR decorated with sawtooth-like, short zigzag edges that host radical states. Since the location of the radicals are on the same sublattice sites, it follows from Lieb's theorem that the ground state is a FM order of the spins, also confirmed by DFT calculations in the local spin density approximation (LSDA) as seen in the corresponding spin-polarized band structure [27]. This GNR structure was experimentally realized in [27, 230]. A metallic behavior was reported on the Au(111) substrate, instead of the gapped FM phase predicted for the freestanding ribbon, a difference that was explained as due to a combination of $p$-doping and surface electric fields induced by the substrate [27].

Another class of GNR spin chains is that of AGNRs with borylated segments as shown in figure 21(k) [66, 233]. As discussed in section 5.5 the combination of pristine 7AGNR and 2B-7AGNR segments results in topological interface states that, depending on their spatial separation, may either hybridize as filled closed-shell states or exhibit spin polarization at the ends of the pristine segments. We note that in the shown example the exchange couplings $J_P > 0$ and $J_B > 0$ lead to an AFM ordering. However, for a single 2B-AGNR unit between pristine segments, DFT calculations have shown a FM ordering [70].

## 7. Reactivity

### 7.1. Reactivity under UHV

Radical states are intrinsically associated with a pronounced reactivity, although the latter may be reduced by steric protection of the radical sites, by electronic stabilization or by a combination of these two strategies [12, 13, 119, 120, 234]. One of the ways in which electronic stabilization can be promoted is by radical delocalization, which as discussed earlier can be enhanced by the hybridization of the radical states with the following doubly occupied orbitals. Such delocalization reduces the spin density at the radical site, which, although not the only one, is the main determining factor in the reactivity [12, 13]. For that reason, molecular structures with large spin density like Clar's goblet [24] or triangulenes [122] show a remarkable tendency to react and polymerize on their supporting surfaces, lowering the yield of the isolated target products. It is particularly instructive to compare the reactivity of closely related molecules with and without spin polarization, as is the case of extended triangulene and double triangulene [100]. The latter shows a prevalent closed-shell character, whereas the former is an open-shell structure with notable spin polarization. As a result, the sample preparation of extended triangulene by OSS on Au(111) results mostly in dimerized units, with monomers amounting to only about 12.5% [100]. In contrast, in the synthesis of double triangulene nearly all molecules remain as monomers. A similar scenario is found comparing rhombene molecules of different size, namely [4]-rhombene and [5]-rhombene, which display a prevailing closed-shell and open-shell character, respectively [133]. The former is obtained by OSS on Au(111) in quasi full yield, whereas the latter is only rarely found as a monomer (figures 22(a)–(f)) [133]. Similar conclusions were reached from theoretical calculations comparing zigzag- and armchair-edged GNRs [235].

The high reactivity of radical states has indeed also been used as an indirect hint or support for the partial open-shell character of molecular structures on which no other magnetic fingerprint was experimentally measured. For example, this is the case of higher acenes. Heptacene, and to a greater extent nonacene, show a tendency to coordinate to metal adatoms at their most reactive central ring [155, 236, 238] when adsorbed on Au(111) (figure 22(g)), although the adatoms can be controllably be removed by scanning probe manipulation (figure 22(h)) [236]. The fact that shorter acenes remain stable and uncoordinated under the same conditions has been thus correlated with the closed-shell character of short acenes and

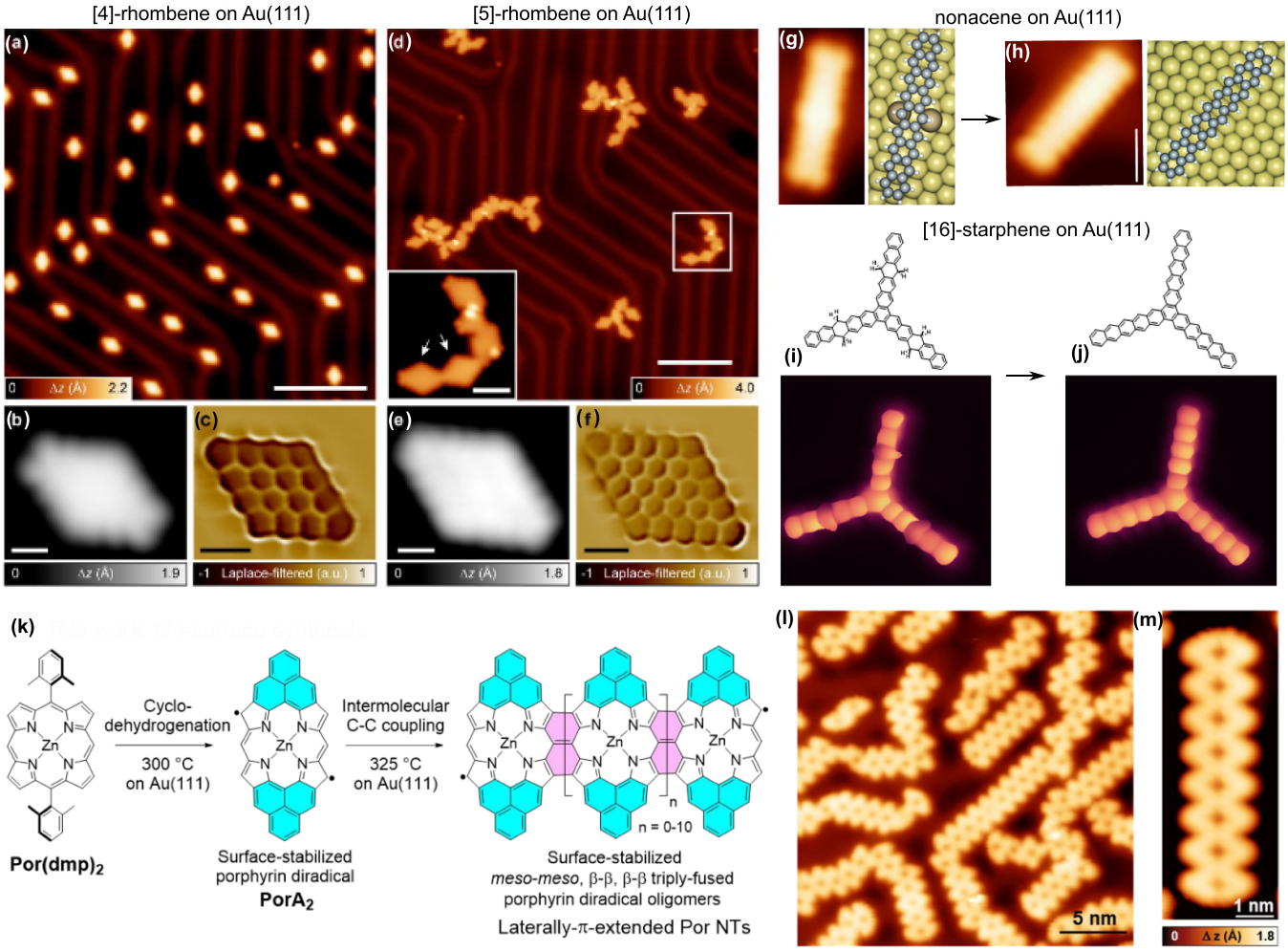


**Figure 22.** (a) Overview STM image of the sample after annealing the [4]-rhombene precursor on a Au(111) surface. (b) STM and (c) bond-resolving STM image of a single [4]-rhombene product. (d) Overview STM image of the sample after annealing the [5]-rhombene precursor on a Au(111) surface. (e) STM and (f) bond-resolving STM image of a single [5]-rhombene product. (g) STM image and associated model structure of nonacene on Au(111) interacting with Au adatoms. (h) STM image and associated model structure of nonacene on Au(111) in the absence of Au adatoms. (i) Bond-resolving STM image of [16]-starphene on Au(111) hydrogenated at its most reactive rings and (j) the same molecule after tip-induced dehydrogenation. (k) Reactant and synthetic route for porphyrine nanotapes. (l) Overview and (m) zoom-in image of the porphyrine nanotapes on Au(111). (a)–(f) Reproduced from [133], with permission from Springer Nature. (g), (h) Reproduced from [236]. CC BY 4.0. (i), (j) [91] John Wiley & Sons. © 2021 Wiley-VCH GmbH. (k)–(m) Reproduced from [237]. CC BY 4.0.

the increasing open-shell character of acenes as they grow longer (in particular above hexacene), as supported also by calculations [236]. A similar reasoning has been applied to the case of [16]-starphene on Au(111), whose notable tendency to become hydrogenated at the central rings of each of its arms (figure 22(i)), although easily reversible by scanning probe manipulation (figure 22(j)), has also been associated to its partial open-shell character [91].

Although the examples outlined above present the increased reactivity of open-shell molecules as a downside, it may also be used constructively. A beautiful example is the formation of porphyrine nanotapes, in which an initial cyclodehydrogenation step first forms surface-supported porphyrine diradical molecules (figure 22(k)) [237]. The reactivity of the associated radicals is particularly high at specific molecular positions, ultimately driving a relatively well-defined and selective polymerization process towards atomically precise porphyrine nanotapes (figures 22(k)–(m)) [237].

A very important parameter with regard to the reactivity of the molecules is the supporting substrate, which can affect it in different ways. For example, a strong molecule-substrate interaction may quench the radical character of the molecules and thereby their reactivity, although at the expense of an equally quenched magnetism. However, even if the molecules retain their radical character, strong molecule-substrate interactions may also be associated to strongly corrugated adsorption energies that limit the molecule's diffusion and thereby the potential polymerization events. Either way, the substrate can limit the molecule's reactivity and thereby increase the yield and selectivity during their synthesis. By way of example, whereas isolated [7]-triangulene could not

be obtained on the weakly interacting Au(111) because its pronounced reactivity caused the molecule's covalent coupling into molecular clusters, on Cu(111) the yield of isolated [7]-triangulene was dramatically improved [122]. However, the desired open-shell septet ($S = 3$) anticipated from counting rules and confirmed by gas-phase calculations turned out to become a trivial closed-shell electronic structure on Cu(111) [122]. Similar findings were observed also for other molecules like [5]-rhombene, which in its isolated form is only a minority product on Au(111) because its pronounced radical character and high diffusion promote the molecule's random polymerization (figure 22(d)), while on the more interactive Cu(110) its yield is orders of magnitude higher [133].

### *7.2. Reactivity in controlled atmospheres and ambient conditions*

The previous section discussed the reactivity of open-shell carbon-nanostructures under ultra-high-vacuum, which, as already seen, is of key importance for their synthesis. However, most of the potential applications envisioned for these materials requires further processing [239–243]. By way of example, the metallic substrates commonly used in their synthesis a detrimental or directly impedes many optoelectronic applications, therefore requiring the material's transfer to other functional substrates. Besides, scalable device applications need to be applicable out of the vacuum environment. Whereas closed-shell structures with armchair edges have successfully survived transfer processes and ultimate device utilization that included exposure to a multitude of environments like different solvents or air [239–243], the same scenario poses serious challenges for open-shell carbon-based nanostructures.

By way of example, it has been recently shown that narrow (3, 1)-chiral GNRs, which display an alternating edge structure composed by three zigzag and one armchair units (figures 12(h)–(j) and 23), are dramatically affected by oxidizing environments in spite of their predominantly closed-shell character [181]. This can be observed in figure 23, which shows overview and bond-resolving STM images of the GNRs before and after exposure to air. The overview images show the long and straight shape of the as-synthesized ribbons (figure 23(a)), which turns curvy after air exposure (figure 23(b)), already hinting at their chemical modification. The bond-resolving images confirm the degradation scenario, on which the protruding signals from many of the C atoms at the GNR edges, as well as modification of the shapes, sizes and brightness of the hexagons that form the carbon backbone (figure 23(d)), all relate to the chemical alteration after the air exposure [181]. The characterization of the air-exposed sample required an additional annealing treatment at 200 °C to desorb the largest part of contaminants that came with the air exposure (although as may be observed in figure 23(c), many remained still adsorbed around the GNRs in spite of the treatment). This posed the question, whether the degradation had been thermally activated by the annealing [244] or was already occurring at RT. More controlled experiments with exposure to low pressure ($3 \times 10^{-5}$ mbar) of pure oxygen gas at RT confirmed that a multitude of oxidation products appear also

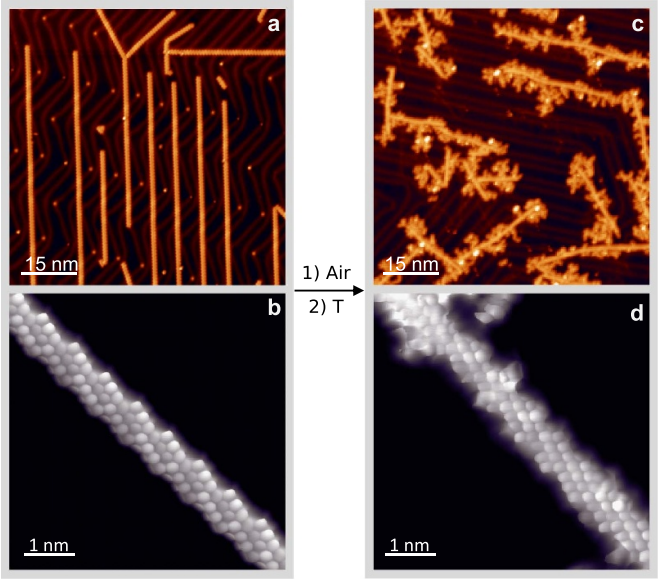


**Figure 23.** Overview STM images (a), (c) and bond-resolving STM images (b), (d) of the chiral GNRs as grown on Au(111) under UHV (a), (b), and after exposure to air for 3 days, followed by an annealing at 200 °C for 15 h (c), (d). Reprinted with permission from [181]. Copyright (2021) American Chemical Society.

under those more gentle conditions, further revealing the most reactive sites and the nature of the most prevalent reaction products [181]. The rationalization of the remarkable reactivity invoked the small but apparently already sufficient open-shell character of the structure.

Similar findings with regard to the lack of stability and of the most common reaction product, were found also for the zigzag ends of 5-AGNRs [104]. Exposure to low pressures ($2 \times 10^{-5}$ mbar) of pure oxygen resulted in ketone-functionalized ribbon ends independently of the ribbon length that determines its varying open- to closed-shell character [104]. Along the same lines, a low band gap pyrene-based GNR that also displays periodic zigzag-oriented edge sites (figure 23(b)) [160, 245], has been equally shown to oxidize already at RT with a 20 min exposure to only $10^{-6}$ mbar of pure oxygen [245].

At this point it is important to remark various issues. First, that the examples discussed above show a predominantly closed-shell character and that the lack of stability will be even worse in structures with increasing open-shell character. Second, that all these cases already suffered irreversible damage upon exposure to low pressures of pure oxygen (still in the high-vacuum range), which is beyond doubt a lower limit regarding the harshness of the treatment to which the carbon-based nanostructures may be exposed, if compared to a conventional transfer process or device implementation in solvents or air. Altogether, this brings up the need to revise the approaches and devise new strategies for the actual implementation of magnetic carbon-based nanostructures in scalable devices. Although still far from allowing for this ultimate goal, the development of chemical protection and deprotection strategies may be a first step in that direction [183].

## 8. Outlook

As stressed throughout the first sections of this review, the rapid progress made in the development of magnetic carbon-based materials is intimately linked to the advances in the field of OSS. For that reason, it also shares many of its challenges. The latter have been analyzed and listed in several OSS reviews [15–19, 246, 247], and range from the development of purification methods to get rid of all the byproducts of non-selective reactions, to the need of non-metallic substrates [248] for many technological applications (or even just for a better characterization), which thus requires either new synthetic approaches or efficient, non-invasive transfer methods. The latter are particularly challenging when dealing with open-shell nanostructures, given their unstable and reactive character. The development of chemical protection and deprotection methods seem promising in this respect [183], but would require further optimization and its combination with other forms of protection like, e.g. capping layers to allow for the eventual implementation of such open-shell carbon nanomaterials in actual devices. Another challenge faced by the field is the ability to bridge from the nanoscale functionality at the molecular level to the mesoscale for actual device engineering, maintaining the atomic precision to avoid the problems associated with defects [249], and all of it in a scalable manner.

Besides these more generic challenges, there are many others specifically for magnetic carbon nanostructures. One of them is, e.g. the direct measurement of their magnetic properties by spin-polarized STM and electron-spin-resonance STM. On the theory side, there are corresponding challenges to develop complete quantum descriptions of the $\pi$-electron spin physics of nanographenes taking explicitly into account the various environmental interactions (e.g. electronic coupling to substrates/electrodes and hyperfine coupling to nuclear spins) and the spin dynamics that can be probed or induced by time-dependent external drives (nonequilibrium). Electrical spin manipulation is one example of the latter [250].

When it comes to actual applications, open-shell carbon nanostructures have been proposed as a promising platform for many disparate uses. By way of example, radical molecules may act as particularly efficient photon emitters, whose doublet-spin nature avoids the formation of triplet excitons that limit the electroluminescence efficiency of non-radical emitters [11, 251–253]. This may be of good use in conventional applications like organic light-emitting diodes [251–253], but also in more advanced quantum applications like the generation of efficient single-photon emitters [11]. In fact, bright, narrow-band, and tunable light emission from individual GNR junctions has already been demonstrated [114].

Graphene-based nanostructures have been also proposed for a variety of other spintronics [49] or quantum applications, including spin and valley filters [254, 255], spin rectification [256], logic gates [216, 217, 257], or spin qubits hosted by structures that range from zero to two dimensions [10, 258]. Another area of application is for electron quantum optics, in which GNR-based beam splitters have been proposed as a platform for controlled motion of charge/spin, interferometry, and entanglement [259–263]. Graphene nanostructures thus seem promising for use in the emergent field of quantum-coherent nanoscience [264]. Furthermore, in analogy with nitrogen-vacancy (NV) color centres in diamond [265], they could also become components in quantum sensors for various metrology applications.

Most of these applications, however, have been only proposed at the theoretical level and their experimental realization still needs to be demonstrated in coming years. Many of them also require a controlled manipulation of the associated spin states, which remains a challenge. Electron-spin-resonance STM could allow for their manipulation, as well as for the characterization of their subsequent dynamic response, but its potential still needs to be demonstrated on carbon-based materials. With many groups worldwide working in the field, we will surely witness important advances in a near future addressing many of the above mentioned challenges and creating new ones aiming at novel directions.

## Data availability statement

The data that support the findings of this study are available upon reasonable request from the authors.

## Acknowledgments

The authors acknowledge fruitful discussions with Alejandro Berdonces-Layunta, Pedro Brandimarte, Jan Patrick Calupitan, David Casanova, Martina Corso, David Ecija, Ferdinand Evers, Roman Fasel, Niklas Friedrich, Carlos Garcia, Aran Garcia-Lekue, Geza Giedke, Jingcheng Li, Ricardo Ortiz, Jose Ignacio Pascual, Diego Peña, Francisco Romero Lara, Daniel Sanchez-Portal, Sofia Sanz, Shiyong Wang and Tao Wang. This work was funded by the Spanish MCIN/AEI/ 10.13039/501100011033 (PID2020-115406GB-I00 and PID2019-107338RB-C63), the Basque Department of Education (PIBA-2020-1-0014), and the European Union's Horizon 2020 (FET-Open Project SPRING Grant No. 863098).

## ORCID iDs

Dimas G de Oteyza https://orcid.org/0000-0001-8060-6819
Thomas Frederiksen https://orcid.org/0000-0001-7523-7641

## References

[1] Coronado E 2020 Molecular magnetism: from chemical design to spin control in molecules, materials and devices *Nat. Rev. Mater.* **5** 87–104
[2] Ferrando-Soria J, Vallejo J, Castellano M, Martínez-Lillo J, Pardo E, Cano J, Castro I, Lloret F, Ruiz-García R and Julve M 2017 Molecular magnetism, *quo vadis*? A historical perspective from a coordination chemist viewpoint *Coord. Chem. Rev.* **339** 17–103

[3] Yazyev O V 2010 Emergence of magnetism in graphene materials and nanostructures *Rep. Prog. Phys.* **73** 056501
[4] Song S, Su J, Telychko M, Li J, Li G, Li Y, Su C, Wu J and Lu J 2021 On-surface synthesis of graphene nanostructures with $\pi$-magnetism *Chem. Soc. Rev.* **50** 3238–62
[5] Min H, Hill J E, Sinitsyn N A, Sahu B R, Kleinman L and MacDonald A H 2006 Intrinsic and Rashba spin-orbit interactions in graphene sheets *Phys. Rev.* B **74** 165310
[6] Yazyev O V 2008 Hyperfine interactions in graphene and related carbon nanostructures *Nano Lett.* **8** 1011–5
[7] Slota M *et al* 2018 Magnetic edge states and coherent manipulation of graphene nanoribbons *Nature* **557** 691–5
[8] Yazyev O V and Katsnelson M I 2008 Magnetic correlations at graphene edges: basis for novel spintronics devices *Phys. Rev. Lett.* **100** 047209
[9] Lombardi F, Lodi A, Ma J, Liu J, Slota M, Narita A, Myers W K, Müllen K, Feng X and Bogani L 2019 Quantum units from the topological engineering of molecular graphenoids *Science* **366** 1107
[10] Trauzettel B, Bulaev D V, Loss D and Burkard G 2007 Spin qubits in graphene quantum dots *Nat. Phys.* **3** 192
[11] Zhao S *et al* 2018 Single photon emission from graphene quantum dots at room temperature *Nat. Commun.* **9** 3470
[12] Pizzochero M and Kaxiras E 2022 Hydrogen atoms on zigzag graphene nanoribbons: chemistry and magnetism meet at the edge *Nano Lett.* **22** 1922–8
[13] Stuyver T, Chen B, Zeng T, Geerlings P, De Proft F and Hoffmann R 2019 Do diradicals behave like radicals? *Chem. Rev.* **119** 11291–351
[14] Das S and Wu J 2015 *Open-Shell Benzenoid Polycyclic Hydrocarbons* (New York: Wiley) ch 1, pp 1–36
[15] Clair S and de Oteyza D G 2019 Controlling a chemical coupling reaction on a surface: tools and strategies for on-surface synthesis *Chem. Rev.* **119** 4717
[16] Wang T and Zhu J 2019 Confined on-surface organic synthesis: strategies and mechanisms *Surf. Sci. Rep.* **74** 97–140
[17] Held P A, Fuchs H and Studer A 2017 Covalent-bond formation via on-surface chemistry *Chem. Eur. J.* **23** 5874–92
[18] Dong L, Liu P N and Lin N 2015 Surface-activated coupling reactions confined on a surface *Acc. Chem. Res.* **48** 2765–74
[19] Liu J and Feng X 2020 Synthetic tailoring of graphene nanostructures with zigzag-edged topologies: progress and perspectives *Angew. Chem., Int. Ed.* **59** 23386–401
[20] Ugeda M M, Brihuega I, Guinea F and Gómez-Rodríguez J M 2010 Missing atom as a source of carbon magnetism *Phys. Rev. Lett.* **104** 096804
[21] Clar E and Stewart D G 1953 Aromatic hydrocarbons. LXV. triangulene derivatives *J. Am. Chem. Soc.* **75** 2667–72
[22] Pavlicek N, Mistry A, Majzik Z, Moll N, Meyer G, Fox D J and Gross L 2017 Synthesis and characterization of triangulene *Nat. Nanotechnol.* **12** 308–11
[23] Clar E 1972 *The Aromatic Sextet* (New York: Wiley)
[24] Mishra S *et al* 2020 Topological frustration induces unconventional magnetism in a nanographene *Nat. Nanotechnol.* **15** 22–28
[25] Ruffieux P *et al* 2016 On-surface synthesis of graphene nanoribbons with zigzag edge topology *Nature* **531** 489–92
[26] Gröning O *et al* 2018 Engineering of robust topological quantum phases in graphene nanoribbons *Nature* **560** 209–13
[27] Rizzo D J, Veber G, Jiang J, McCurdy R, Cao T, Bronner C, Chen T, Louie S G, Fischer F R and Crommie M F 2020 Inducing metallicity in graphene nanoribbons via zero-mode superlattices *Science* **369** 1597
[28] Castro Neto A H, Guinea F, Peres N M R, Novoselov K S and Geim A K 2009 The electronic properties of graphene *Rev. Mod. Phys.* **81** 109–62
[29] Meunier V, Souza Filho A G, Barros E B and Dresselhaus M S 2016 Physical properties of low-dimensional $sp^2$-based carbon nanostructures *Rev. Mod. Phys.* **88** 025005
[30] Torres F, Luis E F, Roche S and Charlier J C 2020 *Introduction to Graphene-Based Nanomaterials: From Electronic Structure to Quantum Transport* 2nd edn (Cambridge: Cambridge University Press)
[31] Martin R M 2004 *Electronic Structure: Basic Theory and Practical Methods* (Cambridge: Cambridge University Press)
[32] Sherrill C D, Manolopoulos D E, Martínez T J and Michaelides A 2020 Electronic structure software *J. Chem. Phys.* **153** 070401
[33] Jacob C R and Reiher M 2012 Spin in density-functional theory *Int. J. Quantum Chem.* **112** 3661–84
[34] Ashcroft N W and Mermin N D 1976 *Solid State Physics* (Philadelphia, PA: Saunders College Publishing)
[35] Soler J M, Artacho E, Gale J D, García A, Junquera J, Ordejón P and Sánchez-Portal D 2002 The SIESTA method for *ab initio* order-*N* materials simulation *J. Phys.: Condens. Matter* **14** 2745–79
[36] Papior N 2022 sisl: v0.12.1 (Zenodo) (available at: https://github.com/zerothi/sisl)
[37] Reich S, Maultzsch J, Thomsen C and Ordejón P 2002 Tight-binding description of graphene *Phys. Rev.* B **66** 035412
[38] Hancock Y, Uppstu A, Saloriutta K, Harju A and Puska M J 2010 Generalized tight-binding transport model for graphene nanoribbon-based systems *Phys. Rev.* B **81** 245402
[39] Hubbard J 1963 Electron correlations in narrow energy bands *Proc. R. Soc.* A **276** 238–57
[40] Dutta S, Lakshmi S and Pati S K 2008 Electron-electron interactions on the edge states of graphene: a many-body configuration interaction study *Phys. Rev.* B **77** 073412
[41] Ortiz R and Fernández-Rossier J 2020 Probing local moments in nanographenes with electron tunneling spectroscopy *Prog. Surf. Sci.* **95** 100595
[42] Mishra S *et al* 2020 Collective all-carbon magnetism in triangulene dimers *Angew. Chem., Int. Ed.* **59** 12041–7
[43] Mishra S *et al* 2021 Observation of fractional edge excitations in nanographene spin chains *Nature* **598** 287–92
[44] Ortiz R, Boto R A, García-Martínez N, Sancho-García J C, Melle-Franco M and Fernández-Rossier J 2019 Exchange rules for diradical $\pi$-conjugated hydrocarbons *Nano Lett.* **19** 5991–7
[45] Fujita M, Wakabayashi K, Nakada K and Kusakabe K 1996 Peculiar localized state at zigzag graphite edge *J. Phys. Soc. Japan* **65** 1920–3
[46] Fernández-Rossier J and Palacios J J 2007 Magnetism in graphene nanoislands *Phys. Rev. Lett.* **99** 177204
[47] Yazyev O V 2008 Magnetism in disordered graphene and irradiated graphite *Phys. Rev. Lett.* **101** 037203
[48] Soriano D, Muñoz Rojas F, Fernández-Rossier J and Palacios J J 2010 Hydrogenated graphene nanoribbons for spintronics *Phys. Rev.* B **81** 165409
[49] Soriano D, Tuan D V, Dubois S M M, Gmitra M, Cummings A W, Kochan D, Ortmann F, Charlier J C, Fabian J and Roche S 2015 Spin transport in hydrogenated graphene *2D Mater.* **2** 022002
[50] Ortiz R, Lado J L, Melle-Franco M and Fernández-Rossier J 2016 Engineering spin exchange in nonbipartite graphene zigzag edges *Phys. Rev.* B **94** 094414

[51] Gregersen S S, Power S R and Jauho A P 2017 Nanostructured graphene for spintronics *Phys. Rev.* B **95** 121406

[52] Li J, Sanz S, Corso M, Choi D J, Peña D, Frederiksen T and Pascual J I 2019 Single spin localization and manipulation in graphene open-shell nanostructures *Nat. Commun.* **10** 200

[53] Sanz S, Papior N, Brandbyge M and Frederiksen T 2022 hubbard: v0.2.0. (Zenodo) (available at: https://github.com/dipc-cc/hubbard)

[54] Son Y W, Cohen M L and Louie S G 2006 Energy gaps in graphene nanoribbons *Phys. Rev. Lett.* **97** 216803

[55] Cusinato L, Evangelisti S, Leininger T and Monari A 2018 The electronic structure of graphene nanoislands: a CAS-SCF and NEVPT2 study *Adv. Condens. Matter Phys.* **2018** 9097045

[56] Sandoval-Salinas M E, Carreras A and Casanova D 2019 Triangular graphene nanofragments: open-shell character and doping *Phys. Chem. Chem. Phys.* **21** 9069–76

[57] Plasser F, Pašalić H, Gerzabek M H, Libisch F, Reiter R, Burgdörfer J, Müller T, Shepard R and Lischka H 2013 The multiradical character of one- and two-dimensional graphene nanoribbons *Angew. Chem., Int. Ed.* **52** 2581–4

[58] Hachmann J, Dorando J J, Avilés M and Chan G K L 2007 The radical character of the acenes: a density matrix renormalization group study *J. Chem. Phys.* **127** 134309

[59] Chan G K L and Sharma S 2011 The density matrix renormalization group in quantum chemistry *Annu. Rev. Phys. Chem.* **62** 465–81

[60] Mizukami W, Kurashige Y and Yanai T 2013 More $\pi$ electrons make a difference: emergence of many radicals on graphene nanoribbons studied by ab initio DMRG theory *J. Chem. Theory Comput.* **9** 401–7

[61] Sánchez-Grande A *et al* 2021 Unravelling the open-shell character of peripentacene on Au(111) *J. Phys. Chem. Lett.* **12** 330–6

[62] Brabec J, Brandejs J, Kowalski K, Xantheas S, Legeza O and Veis L 2021 Massively parallel quantum chemical density matrix renormalization group method *J. Comput. Chem.* **42** 534–44

[63] Joost J P, Jauho A P and Bonitz M 2019 Correlated topological states in graphene nanoribbon heterostructures *Nano Lett.* **19** 9045–50

[64] Korytár R and Lorente N 2011 Multi-orbital non-crossing approximation from maximally localized Wannier functions: the Kondo signature of copper phthalocyanine on Ag(100) *J. Phys.: Condens. Matter* **23** 355009

[65] Jacob D, Ortiz R and Fernández-Rossier J 2021 Renormalization of spin excitations and Kondo effect in open-shell nanographenes *Phys. Rev.* B **104** 075404

[66] Cao T, Zhao F and Louie S G 2017 Topological phases in graphene nanoribbons: junction states, spin centers and quantum spin chains *Phys. Rev. Lett.* **119** 076401

[67] Lin K S and Chou M Y 2018 Topological properties of gapped graphene nanoribbons with spatial symmetries *Nano Lett.* **18** 7254–60

[68] Rizzo D J, Veber G, Cao T, Bronner C, Chen T, Zhao F, Rodriguez H, Louie S G, Crommie M F and Fischer F R 2018 Topological band engineering of graphene nanoribbons *Nature* **560** 204–8

[69] Cirera B *et al* 2020 Tailoring topological order and $\pi$-conjugation to engineer quasi-metallic polymers *Nat. Nanotechnol.* **13** 437–43

[70] Friedrich N *et al* 2020 Magnetism of topological boundary states induced by boron substitution in graphene nanoribbons *Phys. Rev. Lett.* **125** 146801

[71] Zhao F, Cao T and Louie S G 2021 Topological phases in graphene nanoribbons tuned by electric fields *Phys. Rev. Lett.* **127** 166401

[72] Zak J 1989 Berry's phase for energy bands in solids *Phys. Rev. Lett.* **62** 2747–50

[73] Resta R 2000 Manifestations of Berry's phase in molecules and condensed matter *J. Phys.: Condens. Matter* **12** R107

[74] Yazyev O V 2013 A guide to the design of electronic properties of graphene nanoribbons *Acc. Chem. Res.* **46** 2319–28

[75] Lieb E H 1989 Two theorems on the Hubbard model *Phys. Rev. Lett.* **62** 1201–4

[76] Ovchinnikov A A 1978 Multiplicity of the ground state of large alternant organic molecules with conjugated bonds *Theor. Chim. Acta* **47** 297–304

[77] Palacios J J, Fernández-Rossier J and Brey L 2008 Vacancy-induced magnetism in graphene and graphene ribbons *Phys. Rev.* B **77** 195428

[78] González-Herrero H, Gómez-Rodríguez J M, Mallet P, Moaied M, Palacios J J, Salgado C, Ugeda M M, Veuillen J Y, Yndurain F and Brihuega I 2016 Atomic-scale control of graphene magnetism by using hydrogen atoms *Science* **352** 437

[79] Carvalho A R, Warnes J H and Lewenkopf C H 2014 Edge magnetization and local density of states in chiral graphene nanoribbons *Phys. Rev.* B **89** 245444

[80] Longuet-Higgins H C 1950 Some studies in molecular orbital theory I. Resonance structures and molecular orbitals in unsaturated hydrocarbons *J. Chem. Phys.* **18** 265–74

[81] Pisani L, Chan J A, Montanari B and Harrison N M 2007 Electronic structure and magnetic properties of graphitic ribbons *Phys. Rev.* B **75** 064418

[82] Weik N, Schindler J, Bera S, Solomon G C and Evers F 2016 Graphene with vacancies: supernumerary zero modes *Phys. Rev.* B **94** 064204

[83] Rano M, Ghosh S K and Ghosh D 2019 In the quest for a stable triplet state in small polyaromatic hydrocarbons: an *in silico* tool for rational design and prediction *Chem. Sci.* **10** 9270–6

[84] Solà M 2013 Forty years of Clar's aromatic $\pi$-sextet rule *Front. Chem.* **1** 22

[85] Konishi A and Kubo T 2015 Organic chemistry of graphene framework *Chemical Science of $\pi$-Electron Systems* (Tokyo: Springer)

[86] Slayden S W and Liebman J F 2001 The energetics of aromatic hydrocarbons: an experimental thermochemical perspective *Chem. Rev.* **101** 1541–66

[87] Konishi A *et al* 2010 Synthesis and characterization of teranthene: a singlet biradical polycyclic aromatic hydrocarbon having Kekulé structures *J. Am. Chem. Soc.* **132** 11021–3

[88] Rabinovitch B S and Looney F S 1955 Nitric oxide catalyzed *Cis-Trans* isomerization of dideuteroethylene *J. Chem. Phys.* **23** 2439–40

[89] Sun Z *et al* 2013 Dibenzoheptazethrene isomers with different biradical characters: an exercise of Clar's aromatic sextet rule in singlet biradicaloids *J. Am. Chem. Soc.* **135** 18229–36

[90] Vasseur G *et al* 2016 Quasi one-dimensional band dispersion and surface metallization in long-range ordered polymeric wires *Nat. Commun.* **7** 10235

[91] Holec J *et al* 2021 A large starphene comprising pentacene branches *Angew. Chem., Int. Ed.* **60** 7752–8

[92] Rauschenbach S, Rinke G, Gutzler R, Abb S, Albarghash A, Le D, Rahman T S, Dürr M, Harnau L and Kern K 2017 Two-dimensional folding of polypeptides into molecular nanostructures at surfaces *ACS Nano* **11** 2420–7

[93] Hinaut A *et al* 2018 Electrospray deposition of structurally complex molecules revealed by atomic force microscopy *Nanoscale* **10** 1337–44

[94] Hla S W, Bartels L, Meyer G and Rieder K H 2000 Inducing all steps of a chemical reaction with the scanning

tunneling microscope tip: towards single molecule engineering *Phys. Rev. Lett.* **85** 2777–80
[95] Kaiser K, Scriven L M, Schulz F, Gawel P, Gross L and Anderson H L 2019 An *sp*-hybridized molecular carbon allotrope, cyclo[18]carbon *Science* **365** 1299–301
[96] Zhong Q, Ihle A, Ahles S, Wegner H A, Schirmeisen A and Ebeling D 2021 Constructing covalent organic nanoarchitectures molecule by molecule via scanning probe manipulation *Nat. Chem.* **13** 1133–9
[97] Palmino F, Loppacher C and Chérioux F 2019 Photochemistry highlights on on-surface synthesis *ChemPhysChem* **20** 2271–80
[98] Wiesendanger R 2009 Spin mapping at the nanoscale and atomic scale *Rev. Mod. Phys.* **81** 1495–550
[99] Balatsky A V, Nishijima M and Manassen Y 2012 Electron spin resonance-scanning tunneling microscopy *Adv. Phys.* **61** 117–52
[100] Li J, Sanz S, Castro-Esteban J, Vilas-Varela M, Friedrich N, Frederiksen T, Peña D and Pascual J I 2020 Uncovering the triplet ground state of triangular graphene nanoflakes engineered with atomic precision on a metal surface *Phys. Rev. Lett.* **124** 177201
[101] Zheng Y *et al* 2020 Engineering of magnetic coupling in nanographene *Phys. Rev. Lett.* **124** 147206
[102] Wang S, Talirz L, Pignedoli C A, Feng X, Müllen K, Fasel R and Ruffieux P 2016 Giant edge state splitting at atomically precise graphene zigzag edges *Nat. Commun.* **7** 11507
[103] Wang T *et al* 2022 Magnetic interactions between radical pairs in chiral graphene nanoribbons *Nano Lett.* **22** 164–71
[104] Lawrence J, Brandimarte P, Berdonces-Layunta A, Mohammed M S G, Grewal A, Leon C C, Sánchez-Portal D and de Oteyza D G 2020 Probing the magnetism of topological end states in 5-armchair graphene nanoribbons *ACS Nano* **14** 4499–508
[105] Kondo J 1968 Effect of ordinary scattering on exchange scattering from magnetic impurity in metals *Phys. Rev.* **169** 437–40
[106] Ternes M, Heinrich A J and Schneider W D 2009 Spectroscopic manifestations of the Kondo effect on single adatoms *J. Phys.: Condens. Matter* **21** 053001
[107] Kouwenhoven L and Glazman L 2001 Revival of the Kondo effect *Phys. World* **14** 33–38
[108] Mishra S, Beyer D, Berger R, Liu J, Gröning O, Urgel J I, Müllen K, Ruffieux P, Feng X and Fasel R 2020 Topological defect-induced magnetism in a nanographene *J. Am. Chem. Soc.* **142** 1147–52
[109] Fernandez-Torrente I, Franke K J and Pascual J I 2008 Vibrational Kondo effect in pure organic charge-transfer assemblies *Phys. Rev. Lett.* **101** 217203
[110] Goldhaber-Gordon D, Göres J, Kastner M A, Shtrikman H, Mahalu D and Meirav U 1998 From the Kondo regime to the mixed-valence regime in a single-electron transistor *Phys. Rev. Lett.* **81** 5225–8
[111] Scott G D and Hu T C 2017 Gate-controlled Kondo effect in a single-molecule transistor with elliptical ferromagnetic leads *Phys. Rev.* B **96** 144416
[112] Jiang Y, Lo P W, May D, Li G, Guo G Y, Anders F B, Taniguchi T, Watanabe K, Mao J and Andrei E Y 2018 Inducing Kondo screening of vacancy magnetic moments in graphene with gating and local curvature *Nat. Commun.* **9** 2349
[113] Koch M, Ample F, Joachim C and Grill L 2012 Voltage-dependent conductance of a single graphene nanoribbon *Nat. Nanotechnol.* **7** 713–7
[114] Chong M C, Afshar-Imani N, Scheurer F, Cardoso C, Ferretti A, Prezzi D and Schull G 2018 Bright electroluminescence from single graphene nanoribbon junctions *Nano Lett.* **18** 175–81
[115] Li J, Friedrich N, Merino N, de Oteyza D G, Peña D, Jacob D and Pascual J I 2019 Electrically addressing the spin of a magnetic porphyrin through covalently connected graphene electrodes *Nano Lett.* **19** 3288–94
[116] Mangnus M J J, Fischer F R, Crommie M F, Swart I and Jacobse P H 2022 Charge transport in topological graphene nanoribbons and nanoribbon heterostructures *Phys. Rev.* B **105** 115424
[117] Mishra S *et al* 2019 Synthesis and characterization of $\pi$-extended triangulene *J. Am. Chem. Soc.* **141** 10621–5
[118] Su J *et al* 2019 Atomically precise bottom-up synthesis of $\pi$-extended [5]triangulene *Sci. Adv.* **5** eaav7717
[119] Arikawa S, Shimizu A, Shiomi D, Sato K and Shintani R 2021 Synthesis and isolation of a kinetically stabilized crystalline triangulene *J. Am. Chem. Soc.* **143** 19599–605
[120] Valenta L, Mayländer M, Kappeler P, Blacque O, Šolomek T, Richert S and Juríček M 2022 Trimesityltriangulene: a persistent derivative of Clar's hydrocarbon *Chem. Commun.* **58** 3019–22
[121] Su J *et al* 2021 On-surface synthesis and characterization of [7]triangulene quantum ring *Nano Lett.* **21** 861–7
[122] Mishra S, Xu K, Eimre K, Komber H, Ma J, Pignedoli C A, Fasel R, Feng X and Ruffieux P 2021 Synthesis and characterization of [7]triangulene *Nanoscale* **13** 1624–8
[123] Su X, Li C, Du Q, Tao K, Wang S and Yu P 2020 Atomically precise synthesis and characterization of heptauthrene with triplet ground state *Nano Lett.* **20** 6859–64
[124] Zheng Y *et al* 2020 Designer spin order in diradical nanographenes *Nat. Commun.* **11** 6076
[125] Lehtinen P O, Foster A S, Ayuela A, Krasheninnikov A, Nordlund K and Nieminen R M 2003 Magnetic properties and diffusion of adatoms on a graphene sheet *Phys. Rev. Lett.* **91** 017202
[126] Yazyev O V and Helm L 2007 Defect-induced magnetism in graphene *Phys. Rev.* B **75** 125408
[127] Boukhvalov D W, Katsnelson M I and Lichtenstein A I 2008 Hydrogen on graphene: electronic structure, total energy, structural distortions and magnetism from first-principles calculations *Phys. Rev.* B **77** 035427
[128] Leconte N, Soriano D, Roche S, Ordejon P, Charlier J C and Palacios J J 2011 Magnetism-dependent transport phenomena in hydrogenated graphene: from spin-splitting to localization effects *ACS Nano* **5** 3987–92
[129] Soriano D, Leconte N, Ordejón P, Charlier J C, Palacios J J and Roche S 2011 Magnetoresistance and magnetic ordering fingerprints in hydrogenated graphene *Phys. Rev. Lett.* **107** 016602
[130] Santos E J G, Ayuela A and Sánchez-Portal D 2012 Universal magnetic properties of $sp^3$-type defects in covalently functionalized graphene *New J. Phys.* **14** 043022
[131] Cyvin S J, Brunvoll J and Cyvin B N 1990 The hunt for concealed non-Kekuléan polyhexes *J. Math. Chem.* **4** 47–54
[132] Li J, Sanz S, Merino-Díez N, Vilas-Varela M, Garcia-Lekue A, Corso M, de Oteyza D G, Frederiksen T, Peña D and Pascual J I 2021 Topological phase transition in chiral graphene nanoribbons: from edge bands to end states *Nat. Commun.* **12** 5538
[133] Mishra S *et al* 2021 Large magnetic exchange coupling in rhombus-shaped nanographenes with zigzag periphery *Nat. Chem.* **13** 581–6
[134] Casado J 2017 *Para*-quinodimethanes: a unified review of the quinoidal-versus-aromatic competition and its implications *Top. Curr. Chem.* **375** 73
[135] Wang S *et al* 2019 On-surface synthesis and characterization of individual polyacetylene chains *Nat. Chem.* **11** 924–30
[136] Trinquier G and Malrieu J P 2018 Predicting the open-shell character of polycyclic hydrocarbons in terms of Clar sextets *J. Phys. Chem.* A **122** 1088–103

[137] Yeh C N and Chai J D 2016 Role of Kekulé and non-Kekulé structures in the radical character of alternant polycyclic aromatic hydrocarbons: a TAO-DFT study *Sci. Rep.* **6** 30562

[138] Yang Y, Davidson E R and Yang W 2016 Nature of ground and electronic excited states of higher acenes *Proc. Natl Acad. Sci. USA* **113** E5098

[139] Son Y W, Cohen M L and Louie S G 2006 Half-metallic graphene nanoribbons *Nature* **444** 347–9

[140] Magda G Z, Jin X, Hagymasi I, Vancso P, Osvath Z, Nemes-Incze P, Hwang C, Biro L P and Tapaszto L 2014 Room-temperature magnetic order on zigzag edges of narrow graphene nanoribbons *Nature* **514** 608–11

[141] Korytár R, Xenioti D, Schmitteckert P, Alouani M and Evers F 2014 Signature of the Dirac cone in the properties of linear oligoacenes *Nat. Commun.* **5** 5000

[142] Eisenhut F *et al* 2020 Dodecacene generated on surface: reopening of the energy gap *ACS Nano* **14** 1011–7

[143] Gutzler R and Perepichka D F 2013 $\pi$-electron conjugation in two dimensions *J. Am. Chem. Soc.* **135** 16585–94

[144] de Oteyza D G *et al* 2016 Substrate-independent growth of atomically precise chiral graphene nanoribbons *ACS Nano* **10** 9000–8

[145] Merino-Díez N, Mohammed M S G, Castro-Esteban J, Colazzo L, Berdonces-Layunta A, Lawrence J, Pascual J I, de Oteyza D G and Peña D 2020 Transferring axial molecular chirality through a sequence of on-surface reactions *Chem. Sci.* **11** 5441–6

[146] Suda S and Oshiyama A 2015 Energetics, electron states and magnetization in nearly zigzag-edged graphene nano-ribbons *J. Phys. Soc. Japan* **84** 024704

[147] Merino-Díez N *et al* 2018 Unraveling the electronic structure of narrow atomically precise chiral graphene nanoribbons *J. Phys. Chem. Lett.* **9** 25–30

[148] Yazyev O V, Capaz R B and Louie S G 2011 Theory of magnetic edge states in chiral graphene nanoribbons *Phys. Rev.* B **84** 115406

[149] Jiang Z and Song Y 2015 Band gap oscillation and novel transport property in ultrathin chiral graphene nanoribbons *Physica* B **464** 61–67

[150] Biswas K *et al* 2022 Synthesis and characterization of peri-heptacene on a metallic surface *Angew. Chem., Int. Ed.* **61** e202114983

[151] Mishra S, Lohr T G, Pignedoli C A, Liu J, Berger R, Urgel J I, Müllen K, Feng X, Ruffieux P and Fasel R 2018 Tailoring bond topologies in open-shell graphene nanostructures *ACS Nano* **12** 11917–27

[152] Tönshoff C and Bettinger H F 2021 Pushing the limits of acene chemistry: the recent surge of large acenes *Chem. Eur. J.* **27** 3193–212

[153] Konishi A and Kubo T 2017 Benzenoid quinodimethanes *Top. Curr. Chem.* **375** 83

[154] Bendikov M, Duong H M, Starkey K, Houk K N, Carter E A and Wudl F 2004 Oligoacenes: theoretical prediction of open-shell singlet diradical ground states *J. Am. Chem. Soc.* **126** 7416–7

[155] Zade S S and Bendikov M 2012 Reactivity of acenes: mechanisms and dependence on acene length *J. Phys. Org. Chem.* **25** 452–61

[156] Shen B, Tatchen J, Sanchez-Garcia E and Bettinger H F 2018 Evolution of the optical gap in the acene series: undecacene *Angew. Chem., Int. Ed.* **57** 10506–9

[157] Chen W, Li H, Widawsky J R, Appayee C, Venkataraman L and Breslow R 2014 Aromaticity decreases single-molecule junction conductance *J. Am. Chem. Soc.* **136** 918–20

[158] Grover G, Peters G M, Tovar J D and Kertesz M 2020 Quinonoid vs. aromatic structures of heteroconjugated polymers from oligomer calculations *Phys. Chem. Chem. Phys.* **22** 11431–9

[159] Su W P, Schrieffer J R and Heeger A J 1979 Solitons in polyacetylene *Phys. Rev. Lett.* **42** 1698–701

[160] Sun Q *et al* 2020 Massive Dirac fermion behavior in a low bandgap graphene nanoribbon near a topological phase boundary *Adv. Mater.* **32** 1906054

[161] Yuan B *et al* 2020 Resolving quinoid structure in poly(para-phenylene) chains *J. Am. Chem. Soc.* **142** 10034–41

[162] Mikie T and Osaka I 2020 Small-bandgap quinoid-based $\pi$-conjugated polymers *J. Mater. Chem.*C **8** 14262–88

[163] Bérubé N, Gaudreau J and Côté M 2013 Low band gap polymers design approach based on a mix of aromatic and quinoid structures *Macromolecules* **46** 6873–80

[164] Corso M and de Oteyza D G 2020 Topological engineering for metallic polymers *Nat. Nanotechnol.* **15** 421–3

[165] González-Herrero H, Mendieta-Moreno J I, Edalatmanesh S, Santos J, Martín N, Écija D, Torre B and Jelinek P 2021 Atomic scale control and visualization of topological quantum phase transition in $\pi$-conjugated polymers driven by their length *Adv. Mater.* **33** 2104495

[166] Bersuker I B 2013 Pseudo-Jahn–Teller effect—a two-state paradigm in formation, deformation and transformation of molecular systems and solids *Chem. Rev.* **113** 1351–90

[167] Carbonell-Sanromà E *et al* 2017 Doping of graphene nanoribbons via functional group edge modification *ACS Nano* **11** 7355

[168] Li J *et al* 2020 Band depopulation of graphene nanoribbons induced by chemical gating with amino groups *ACS Nano* **14** 1895–901

[169] Zhao F, Cao T and Louie S G 2021 Topological phases in graphene nanoribbons tuned by electric fields *Phys. Rev. Lett.* **127** 166401

[170] Sánchez-Sánchez C *et al* 2019 On-surface synthesis and characterization of acene-based nanoribbons incorporating four-membered rings *Chem. Eur. J.* **25** 12074–82

[171] Cui P, Zhang Q, Zhu H, Li X, Wang W, Li Q, Zeng C and Zhang Z 2016 Carbon tetragons as definitive spin switches in narrow zigzag graphene nanoribbons *Phys. Rev. Lett.* **116** 026802

[172] Plasser F 2021 Exploitation of Baird aromaticity and Clar's rule for tuning the triplet energies of polycyclic aromatic hydrocarbons *Chemistry* **3** 532–49

[173] Zeng Z *et al* 2022 Chemisorption-induced formation of biphenylene dimer on Ag(111) *J. Am. Chem. Soc.* **144** 723–32

[174] Kawai S *et al* 2017 Competing annulene and radialene structures in a single anti-aromatic molecule studied by high-resolution atomic force microscopy *ACS Nano* **11** 8122–30

[175] Lawrence J, Mohammed M S G, Rey D, Aguilar-Galindo F, Berdonces-Layunta A, Peña D and de Oteyza D G 2021 Reassessing alkyne coupling reactions while studying the electronic properties of diverse pyrene linkages at surfaces *ACS Nano* **15** 4937–46

[176] Di Giovannantonio M, Chen Q, Urgel J I, Ruffieux P, Pignedoli C A, Müllen K, Narita A and Fasel R 2020 On-surface synthesis of oligo(indenoindene) *J. Am. Chem. Soc.* **142** 12925–9

[177] Di Giovannantonio M *et al* 2019 On-surface synthesis of antiaromatic and open-shell indeno[2,1-b]fluorene polymers and their lateral fusion into porous ribbons *J. Am. Chem. Soc.* **141** 12346–54

[178] Di Giovannantonio M and Fasel R 2022 On-surface synthesis and atomic scale characterization of unprotected indenofluorene polymers *J. Polym. Sci.* **60** 1814–26

[179] Li C *et al* 2022 Topological defects induced high-spin quartet state in truxene-based molecular graphenoids (arXiv:2202.03853)

[180] Mishra S, Fatayer S, Fernández S, Kaiser K, Peña D and Gross L 2022 Nonbenzenoid high-spin polycyclic hydrocarbons generated by atom manipulation *ACS Nano* **16** 3264–71

[181] Berdonces-Layunta A, Lawrence J, Edalatmanesh S, Castro-Esteban J, Wang T, Mohammed M S G, Colazzo L, Peña D, Jelínek P and de Oteyza D G 2021 Chemical stability of (3, 1)-chiral graphene nanoribbons *ACS Nano* **15** 5610–7

[182] Wang T, Berdonces-Layunta A, Friedrich N, Vilas-Varela M, Calupitan J P, Pascual J I, Peña D, Casanova D, Corso M and de Oteyza D G 2022 Aza-triangulene: on-surface synthesis and electronic and magnetic properties *J. Am. Chem. Soc.* **144** 4522–9

[183] Lawrence J, Berdonces-Layunta A, Edalatmanesh S, Castro-Esteban J, Wang T, Mohammed M S G, Vilas-Varela M, Jelinek P, Peña D and de Oteyza D G 2021 Circumventing the stability problems of graphene nanoribbon zigzag edges (arXiv:2107.12754)

[184] Błoński P, Tuček J, Sofer Z, Mazánek V, Petr M, Pumera M, Otyepka M and Zbořil R 2017 Doping with graphitic nitrogen triggers ferromagnetism in graphene *J. Am. Chem. Soc.* **139** 3171–80

[185] Babar R and Kabir M 2019 Ferromagnetism in nitrogen-doped graphene *Phys. Rev.* B **99** 115442

[186] Wang X, Sun G, Routh P, Kim D H, Huang W and Chen P 2014 Heteroatom-doped graphene materials: syntheses, properties and applications *Chem. Soc. Rev.* **43** 7067–98

[187] Zhang P, Li X, Dong J, Zhu M, Zheng F and Zhang J 2022 $\pi$-magnetism and spin-dependent transport in boron pair doped armchair graphene nanoribbons *Appl. Phys. Lett.* **120** 132406

[188] Blackwell R E, Zhao F, Brooks E, Zhu J, Piskun I, Wang S, Delgado A, Lee Y L, Louie S G and Fischer F R 2021 Spin splitting of dopant edge state in magnetic zigzag graphene nanoribbons *Nature* **600** 647–52

[189] Garcia-Lekue A and Sánchez-Portal D 2021 Clever substitutions reveal magnetism in zigzag graphene nanoribbons *Nature* **600** 613–4

[190] Anderson P W 1961 Localized magnetic states in metals *Phys. Rev.* **124** 41

[191] Hollerer M, Lüftner D, Hurdax P, Ules T, Soubatch S, Tautz F S, Koller G, Puschnig P, Sterrer M and Ramsey M G 2017 Charge transfer and orbital level alignment at inorganic/organic interfaces: the role of dielectric interlayers *ACS Nano* **11** 6252–60

[192] Borghetti P, El-Sayed A, Goiri E, Rogero C, Lobo-Checa J, Floreano L, Ortega J E and de Oteyza D G 2014 Spectroscopic fingerprints of work-function-controlled phthalocyanine charging on metal surfaces *ACS Nano* **8** 12786–95

[193] Goiri E, Borghetti P, El-Sayed A, Ortega J E and de Oteyza D G 2016 Multi-component organic layers on metal substrates *Adv. Mater.* **28** 1340–68

[194] Goiri E, Matena M, El-Sayed A, Lobo-Checa J, Borghetti P, Rogero C, Detlefs B, Duvernay J, Ortega J E and de Oteyza D G 2014 Self-assembly of bicomponent molecular monolayers: adsorption height changes and their consequences *Phys. Rev. Lett.* **112** 117602

[195] Stadtmüller B *et al* 2014 Unexpected interplay of bonding height and energy level alignment at heteromolecular hybrid interfaces *Nat. Commun.* **5** 3685

[196] Franke K J, Schulze G, Henningsen N, Fernandez-Torrente I, Pascual J I, Zarwell S, Ruck-Braun K, Cobian M and Lorente N 2008 Reducing the molecule-substrate coupling in $C_{60}$-based nanostructures by molecular interactions *Phys. Rev. Lett.* **100** 036807

[197] Fernández-Torrente I, Kreikemeyer-Lorenzo D, Stróżecka A, Franke K J and Pascual J I 2012 Gating the charge state of single molecules by local electric fields *Phys. Rev. Lett.* **108** 036801

[198] Mohammed M S G, Colazzo L, Robles R, Dorel R, Echavarren A M, Lorente N and de Oteyza D G 2020 Electronic decoupling of polyacenes from the underlying metal substrate by $sp^3$ carbon atoms *Commun. Phys.* **3** 159

[199] Colazzo L, Mohammed M S G, Dorel R, Nita P, García Fernández C, Abufager P, Lorente N, Echavarren A M and de Oteyza D G 2018 On-surface synthesis of heptacene on Ag(001) from brominated and non-brominated tetrahydroheptacene precursors *Chem. Commun.* **54** 10260–3

[200] Zuzak R, Dorel R, Krawiec M, Such B, Kolmer M, Szymonski M, Echavarren A M and Godlewski S 2017 Nonacene generated by on-surface dehydrogenation *ACS Nano* **11** 9321–9

[201] Corso M, Menchón R E, Piquero-Zulaica I, Vilas-Varela M, Ortega J E, Peña D, Garcia-Lekue A and de Oteyza D G 2021 Band structure and energy level alignment of chiral graphene nanoribbons on silver surfaces *Nanomaterials* **11** 3303

[202] Garnica M, Stradi D, Barja S, Calleja F, Diaz C, Alcami M, Martin N, Vazquez de Parga A L, Martin F and Miranda R 2013 Long-range magnetic order in a purely organic 2D layer adsorbed on epitaxial graphene *Nat. Phys.* **9** 368–74

[203] Sun Q, Mateo L M, Robles R, Ruffieux P, Lorente N, Bottari G, Torres T and Fasel R 2020 Inducing open-shell character in porphyrins through surface-assisted phenalenyl $\pi$-extension *J. Am. Chem. Soc.* **142** 18109–17

[204] Zhao Y *et al* 2020 Precise control of $\pi$-electron magnetism in metal-free porphyrins *J. Am. Chem. Soc.* **142** 18532–40

[205] Dutta S and Wakabayashi K 2012 Tuning charge and spin excitations in zigzag edge nanographene ribbons *Sci. Rep.* **2** 519

[206] Pizzochero M and Kaxiras E 2021 Imprinting tunable $\pi$-magnetism in graphene nanoribbons via edge extensions *J. Phys. Chem. Lett.* **12** 1214–9

[207] Merino-Díez N, Garcia-Lekue A, Carbonell-Sanromà E, Li J, Corso M, Colazzo L, Sedona F, Sánchez-Portal D, Pascual J I and de Oteyza D G 2017 Width-dependent band gap in armchair graphene nanoribbons reveals fermi level pinning on Au(111) *ACS Nano* **11** 11661–8

[208] Chen Y C, de Oteyza D G, Pedramrazi Z, Chen C, Fischer F R and Crommie M F 2013 Tuning the band gap of graphene nanoribbons synthesized from molecular precursors *ACS Nano* **7** 6123–8

[209] Zeng W, Sun Z, Herng T S, Gonçalves T P, Gopalakrishna T Y, Huang K W, Ding J and Wu J 2016 Super-heptazethrene *Angew. Chem., Int. Ed.* **55** 8615–9

[210] Mishra S, Melidonie J, Eimre K, Obermann S, Gröning O, Pignedoli C A, Ruffieux P, Feng X and Fasel R 2020 On-surface synthesis of super-heptazethrene *Chem. Commun.* **56** 7467–70

[211] Turco E, Mishra S, Melidonie J, Eimre K, Obermann S, Pignedoli C A, Fasel R, Feng X and Ruffieux P 2021 On-surface synthesis and characterization of super-nonazethrene *J. Phys. Chem. Lett.* **12** 8314–9

[212] Sawada K, Ishii F, Saito M, Okada S and Kawai T 2009 Phase control of graphene nanoribbon by carrier doping: appearance of noncollinear magnetism *Nano Lett.* **9** 269–72

[213] Jung J and MacDonald A H 2009 Carrier density and magnetism in graphene zigzag nanoribbons *Phys. Rev.* B **79** 235433

[214] Hieulle J *et al* 2021 On-surface synthesis and collective spin excitations of a triangulene-based nanostar *Angew. Chem., Int. Ed.* **60** 25224–9

[215] Sánchez-Grande A *et al* 2020 Diradical organic one-dimensional polymers synthesized on a metallic surface *Angew. Chem., Int. Ed.* **59** 17594–9

[216] Wang W L, Yazyev O V, Meng S and Kaxiras E 2009 Topological frustration in graphene nanoflakes: magnetic order and spin logic devices *Phys. Rev. Lett.* **102** 157201

[217] Ge Y, Ji J, Shen Z, Zhang Q, Jian A, Duan Q, Wang C, Jiang J, Zhang W and Sang S 2018 First principles study of magnetism induced by topological frustration of bowtie-shaped graphene nanoflake *Carbon* **127** 432–6

[218] Heinrich A J, Gupta J A, Lutz C P and Eigler D M 2004 Single-atom spin-flip spectroscopy *Science* **306** 466–9

[219] Lorente N and Gauyacq J P 2009 Efficient spin transitions in inelastic electron tunneling spectroscopy *Phys. Rev. Lett.* **103** 176601

[220] Fernández-Rossier J 2009 Theory of single-spin inelastic tunneling spectroscopy *Phys. Rev. Lett.* **102** 256802

[221] Fransson J 2009 Spin inelastic electron tunneling spectroscopy on local spin adsorbed on surface *Nano Lett.* **9** 2414–7

[222] Ternes M 2015 Spin excitations and correlations in scanning tunneling spectroscopy *New J. Phys.* **17** 063016

[223] Choi D J, Lorente N, Wiebe J, von Bergmann K, Otte A F and Heinrich A J 2019 Colloquium: Atomic spin chains on surfaces *Rev. Mod. Phys.* **91** 041001

[224] Korytár R, Lorente N and Gauyacq J P 2012 Many-body effects in magnetic inelastic electron tunneling spectroscopy *Phys. Rev.* B **85** 125434

[225] Roch N, Florens S, Costi T A, Wernsdorfer W and Balestro F 2009 Observation of the underscreened Kondo effect in a molecular transistor *Phys. Rev. Lett.* **103** 197202

[226] Haldane F D M 1983 Nonlinear field theory of large-spin heisenberg antiferromagnets: semiclassically quantized solitons of the one-dimensional easy-axis Néel state *Phys. Rev. Lett.* **50** 1153–6

[227] Affleck I 1989 Quantum spin chains and the Haldane gap *J. Phys.: Condens. Matter* **1** 3047–72

[228] Affleck I, Kennedy T, Lieb E H and Tasaki H 1987 Rigorous results on valence-bond ground states in antiferromagnets *Phys. Rev. Lett.* **59** 799–802

[229] Wang S *et al* 2021 Realization of quantum nanomagnets in metal-free porphyrins *Research Square Preprint* (https://doi.org/10.21203/rs.3.rs-579482/v1)

[230] Sun Q, Yao X, Gröning O, Eimre K, Pignedoli C A, Müllen K, Narita A, Fasel R and Ruffieux P 2020 Coupled spin states in armchair graphene nanoribbons with asymmetric zigzag edge extensions *Nano Lett.* **20** 6429–36

[231] Sun Q, Yan Y, Yao X, Müllen K, Narita A, Fasel R and Ruffieux P 2021 Evolution of the topological energy band in graphene nanoribbons *J. Phys. Chem. Lett.* **12** 8679–84

[232] Jiang J and Louie S G 2021 Topology classification using chiral symmetry and spin correlations in graphene nanoribbons *Nano Lett.* **21** 197–202

[233] Carbonell-Sanromà E *et al* 2018 Electronic properties of substitutionally boron-doped graphene nanoribbons on a Au(111) surface *J. Phys. Chem.* C **122** 16092–9

[234] Bellunato A, Arjmandi Tash H, Cesa Y and Schneider G F 2016 Chemistry at the edge of graphene *ChemPhysChem* **17** 785–801

[235] Jiang D E, Sumpter B G and Dai S 2007 Unique chemical reactivity of a graphene nanoribbon's zigzag edge *J. Chem. Phys.* **126** 134701

[236] Urgel J I *et al* 2019 On-surface light-induced generation of higher acenes and elucidation of their open-shell character *Nat. Commun.* **10** 861

[237] Sun Q, Mateo L M, Robles R, Lorente N, Ruffieux P, Bottari G, Torres T and Fasel R 2021 Bottom-up fabrication and atomic-scale characterization of triply linked, laterally $\pi$-extended porphyrin nanotapes *Angew. Chem., Int. Ed.* **60** 16208–14

[238] Zade S S, Zamoshchik N, Reddy A R, Fridman-Marueli G, Sheberla D and Bendikov M 2011 Products and mechanism of acene dimerization. a computational study *J. Am. Chem. Soc.* **133** 10803–16

[239] Bennett P B, Pedramrazi Z, Madani A, Chen Y C, de Oteyza D G, Chen C, Fischer F R, Crommie M F and Bokor J 2013 Bottom-up graphene nanoribbon field-effect transistors *Appl. Phys. Lett.* **103** 253114

[240] Llinas J P *et al* 2017 Short-channel field-effect transistors with 9-atom and 13-atom wide graphene nanoribbons *Nat. Commun.* **8** 633

[241] Moreno C *et al* 2018 Bottom-up synthesis of multifunctional nanoporous graphene *Science* **360** 199

[242] Fairbrother A, Sanchez-Valencia J R, Lauber B, Shorubalko I, Ruffieux P, Hintermann T and Fasel R 2017 High vacuum synthesis and ambient stability of bottom-up graphene nanoribbons *Nanoscale* **9** 2785–92

[243] Mutlu Z, Llinas J P, Jacobse P H, Piskun I, Blackwell R, Crommie M F, Fischer F R and Bokor J 2021 Transfer-free synthesis of atomically precise graphene nanoribbons on insulating substrates *ACS Nano* **15** 2635–42

[244] Ma C, Xiao Z, Puretzky A A, Baddorf A P, Lu W, Hong K, Bernholc J and Li A P 2018 Oxidization stability of atomically precise graphene nanoribbons *Phys. Rev. Mater.* **2** 014006

[245] Barcelon J E *et al* 2021 Morphological characterization and electronic properties of pristine and oxygen-exposed graphene nanoribbons on Ag(110) *Phys. Chem. Chem. Phys.* **23** 7926–37

[246] Shen Q, Gao H Y and Fuchs H 2017 Frontiers of on-surface synthesis: from principles to applications *Nano Today* **13** 77–96

[247] Houtsma R S K, de la Rie J and Stöhr M 2021 Atomically precise graphene nanoribbons: interplay of structural and electronic properties *Chem. Soc. Rev.* **50** 6541–68

[248] Kolmer M, Steiner A K, Izydorczyk I, Ko W, Engelund M, Szymonski M, Li A P and Amsharov K 2020 Rational synthesis of atomically precise graphene nanoribbons directly on metal oxide surfaces *Science* **369** 571

[249] Pizzochero M, Barin G B, Čerņevičs K, Wang S, Ruffieux P, Fasel R and Yazyev O V 2021 Edge disorder in bottom-up zigzag graphene nanoribbons: implications for magnetism and quantum electronic transport *J. Phys. Chem. Lett.* **12** 4692–6

[250] Ortiz R, García-Martínez N A, Lado J L and Fernández-Rossier J 2018 Electrical spin manipulation in graphene nanostructures *Phys. Rev.* B **97** 195425

[251] Abdurahman A, Hele T J H, Gu Q, Zhang J, Peng Q, Zhang M, Friend R H, Li F and Evans E W 2020 Understanding the luminescent nature of organic radicals for efficient doublet emitters and pure-red light-emitting diodes *Nat. Mater.* **19** 1224–9

[252] Ai X, Evans E W, Dong S, Gillett A J, Guo H, Chen Y, Hele T J H, Friend R H and Li F 2018 Efficient radical-based light-emitting diodes with doublet emission *Nature* **563** 536–40

[253] Peng Q, Obolda A, Zhang M and Li F 2015 Organic light-emitting diodes using a neutral $\pi$ radical as emitter: the emission from a doublet *Angew. Chem., Int. Ed.* **54** 7091–5

[254] Rycerz A, Tworzydlo J and Beenakker C W J 2007 Valley filter and valley valve in graphene *Nat. Phys.* **3** 172–5

[255] Wimmer M, Adagideli I, Berber S, Tománek D and Richter K 2008 Spin currents in rough graphene

nanoribbons: universal fluctuations and spin injection *Phys. Rev. Lett.* **100** 177207
[256] Ni Y, Hua H, Li J and Hu N 2022 Perfect spin Seebeck effect, spin-valve, spin-filter and spin-rectification based on the heterojunction of sawtooth graphene and graphyne nanoribbons *Nanoscale* **14** 3818–25
[257] Bullard Z, Girão E C, Owens J R, Shelton W A and Meunier V 2015 Improved all-carbon spintronic device design *Sci. Rep.* **5** 7634
[258] Pedersen T G, Flindt C, Pedersen J, Mortensen N A, Jauho A P and Pedersen K 2008 Graphene antidot lattices: designed defects and spin qubits *Phys. Rev. Lett.* **100** 136804
[259] Botello-Méndez A R, Cruz-Silva E, Romo-Herrera J M, López-Urías F, Terrones M, Sumpter B G, Terrones H, Charlier J C and Meunier V 2011 Quantum transport in graphene nanonetworks *Nano Lett.* **11** 3058–64
[260] Lima L R F, Hernández A R, Pinheiro F A and Lewenkopf C 2016 A 50/50 electronic beam splitter in graphene nanoribbons as a building block for electron optics *J. Phys.: Condens. Matter* **28** 505303
[261] Brandimarte P, Engelund M, Papior N, Garcia-Lekue A, Frederiksen T and Sánchez-Portal D 2017 A tunable electronic beam splitter realized with crossed graphene nanoribbons *J. Chem. Phys.* **146** 092318
[262] Sanz S, Brandimarte P, Giedke G, Sánchez-Portal D and Frederiksen T 2020 Crossed graphene nanoribbons as beam splitters and mirrors for electron quantum optics *Phys. Rev.* B **102** 035436
[263] Sanz S, Papior N, Giedke G, Sánchez-Portal D, Brandbyge M and Frederiksen T 2022 Spin-polarizing electron beam splitter from crossed graphene nanoribbons *Phys. Rev. Lett.* **129** 037701
[264] Heinrich A J, Oliver W D, Vandersypen L M K, Ardavan A, Sessoli R, Loss D, Jayich A B, Fernandez-Rossier J, Laucht A and Morello A 2021 Quantum-coherent nanoscience *Nat. Nanotechnol.* **16** 1318–29
[265] Rondin L, Tetienne J P, Hingant T, Roch J F, Maletinsky P and Jacques V 2014 Magnetometry with nitrogen-vacancy defects in diamond *Rep. Prog. Phys.* **77** 056503